^{1}H MAS NMR Study of Water on Pd-MCM-41

by

Joshua Crone

A thesis
presented to the University of Waterloo
in fulfillment of the
thesis requirement for the degree of
Master of Science
in
Physics

Waterloo, Ontario, Canada, 2015

Author's Declaration

I hereby declare that I am the sole author of this thesis. This is a true copy of the thesis, including any required final revisions, as accepted by my examiners.

I understand that my thesis may be made electronically available to the public.

Abstract

Hydrogen spillover represents one of the most promising avenues to achieve hydrogen storage at the density required for transportation applications. The spillover phenomenon, however, is a topic of much debate, with many conflicting results existing in the literature. The goal of this work is to thoroughly study and understand a system where spillover has been reported, palladium loaded MCM-41 (Pd-MCM-41), thus laying a groundwork favorable to accurate, conclusive work on the spillover phenomenon in the future. Specifically, the nature of the material and how water (an important factor in certain spillover systems) interacts with it are investigated. This information would not only benefit the study of spillover, but also any other application of Pd-MCM-41 where water is involved.

^{1}H MAS NMR measurements were carried out on three mesoporous silica samples at a range of water hydration levels. The materials were unmodified (pristine) MCM-41, Pd-MCM-41 and reduced (ie. treated with H_2 gas) Pd-MCM-41. The spectra from these samples were fit using a previously published model for water on pristine MCM-41, which was extended to account for differences in the current samples.

The model was applied first to the pristine MCM-41 spectra. In the hydration range from 0.0 to 0.2 monolayers (ML) of water adsorbed on the pore surface, the results were similar enough to those from Walia's publication that they were used to aid and assess the fitting results of the Pd loaded samples. Additional features observed in the results for pristine MCM-41 were the appearance of a new peak at 0.5 ML, attributed to water condensing and filling sections of the pore volume, and the development of water-water interactions, which are typically absent at lower hydration levels.

Two additional peaks, designated Pd Water Groups 1 and 2, are observed in the spectra of the palladized samples. Once these were added to the fitting model, the spectra were determined to be

adequately fit by the model; features of the remaining peaks matched those in the pristine sample. Two models, labeled A and B, are presented to explain the differences between the results from pristine MCM-41 and Pd-MCM-41. In Model A, water dissociatively and preferentially adsorbs onto the Pd, causing water to condense around the metal clusters. This multilayer water phase exchanges with water on the pore surface, resulting in Pd Water Group 1. Pd Water Group 2 is attributed to the first layers of water molecules strongly bound to Pd. Model B, which relies on Pd causing nearby water to have a large chemical shift, is shown to be unlikely. The main reason is that the chemical shift of this Pd shifted water is required to increase with increasing water hydration level in order to reproduce the observed chemical shift of Pd Water Group 1. For this and other reasons, Model A is concluded to be the most probable description for the behavior of water on Pd-MCM-41, based on the results presented.

Acknowledgments

They say that many hands make light work, and this project was no exception. Many came before me and I definitely stand on their shoulders. There are a few people in particular that deserve special recognition for their efforts and assistance; without them, there would be nothing.

Dr. Hartwig Peemoeller has been not just a supervisor, but a mentor. He has been equal measures of motivation and seemingly infinite patience. I have learned immeasurably during our time together, sampling his expertise on topics of physics and beyond. Despite all of this, he is one of the humblest men I know. Thank you for everything, it has been a genuine pleasure.

Claude Lemaire was involved with basically every experimental aspect of this and every other project I worked on. His counsel on research matters was always appreciated, and definitely needed, as were all the discussions not about research. Thanks, Claude.

Many other students have worked and learned in the NMR group over the course of my degree. Jaspreet Walia and I shared many conversations and a lot of coffee. He is a creative thinker and avid researcher. I want to wish him continued success in what I expect will be a long and fruitful career. I could not have asked for a better person to share an office space with than Ghada Khouqeer. Her kindness and generosity, especially with baked goods from back home, will never be forgotten. There were several undergraduates who spent time in our group, and all of them contributed to our efforts, especially Ian Lam. I learned something from each of them and hope I returned the favor.

I would also like to thank Dr. Eric Reardon and Dr. Colin Guthrie who provided the samples that were used in this project. Without their contributions, we could not have even started. Thank you both.

Table of Contents

List of Figures

List of Tables

1. Introduction

For about 50 years, there has existed in the literature surrounding heterogeneous catalysis a phenomenon called “spillover” [1 – 17]. In its typical presentation, spillover is characterized by a diatomic gaseous species dissociatively adsorbing onto a catalytically active metal particle and then transferring to the otherwise inert support or substrate of the metal. The most interest is in the spillover of hydrogen because of the incredible potential such a mechanism would have not just to improve innumerable industrial chemical applications, but to change the energy industry as well. The ability to stably and densely store large amounts of hydrogen is a primary goal of hydrogen fuel research [18]. If hydrogen spillover is mastered in systems with high specific surface areas, the technique could achieve the energy density requirements for a fossil fuel alternative [18].

Any lofty goal of spillover research is, however, plagued with difficulties. Despite nearly five decades of research and several international conferences dedicated to the subject, the mechanism is still poorly understood, largely due to many conflicting results. The field suffers from frequent misidentification of spillover in systems where the results can be explained by other processes [6]. Research interest in the topic is waning and is in need of a novel approach.

^{1}H MAS NMR is an ideal method to study hydrogen spillover, being uniquely suited to study the systems it is reported to exist in. ^{1}H NMR is specifically sensitive to hydrogen nuclei, and MAS is a standard method used to greatly improve the spectrum's resolution when a solid-like system is being studied, such as H atoms bound to a surface. Despite the many advantages this technique would have when investigating spillover, ^{1}H MAS NMR has not been extensively used in its study.

Water has been shown to be intimately tied to the spillover phenomenon. It can act as an important intermediary in the transfer of hydrogen, or an equally important contaminant [5]. Either way, a thorough understanding of water in a spillover system could be vital to a full understanding of

the process. ^{1}H MAS NMR has been used to great success in the study of water in many systems, including small amounts of adsorbed water in high surface area systems, like MCM-41.

MCM-41 is a mesoporous silica material with a high specific surface area (~ 1000 m^2/g) [19, 20]. It has long garnered attention for its use in any number of applications that benefit from this characteristic [21 – 37]. The pore surface is often modified with additional compounds, such as catalytically active metals, to tailor the material's function [25, 26, 38 – 44]. Palladium loaded MCM-41 (Pd-MCM-41) has been used to great effect in several applications [25, 26, 40 – 44], it is also a system where hydrogen spillover has been reported [22 – 24]. This is an ideal system for the study of spillover, since there is a wealth of research already on the behavior of water in unmodified MCM-41 [21, 27 – 30].

The goal of the present study is to understand the behavior of water in Pd-MCM-41. This will provide insight into any aqueous system that Pd-MCM-41 is involved in, as well as spillover reactions, which can be activated by, or produce, water. To this end, three samples are studied using ^{1}H MAS NMR: unmodified MCM-41, Pd-MCM-41 and reduced Pd-MCM-41, which has undergone a pretreatment with hydrogen gas. An existing model of water in unmodified MCM-41 [21] is used to interpret the spectral results, first confirming its usefulness by fitting the unmodified MCM-41 results with it. The model is then extended in order to apply it to the Pd loaded samples. The remainder of this document is directed at detailing the pursuit of this goal.

Chapter 2 outlines the various topics of NMR theory required for the analysis of the experiments performed in this study. The 3rd chapter reviews the details of the spillover phenomenon and reviews the state of the present body of knowledge on the subject. The synthesis, characterization and brief review of the present research on MCM-41 is covered in chapter 4. Chapter 5 contains the details of the experimental methods and procedures used in the present study. The results of those

experiments are presented in chapter 6, and the discussion of those results in chapter 7. Finally, the conclusions of this study, as well as recommendations for future work, are found in chapter 8.

2. Nuclear Magnetic Resonance

Nuclear magnetic resonance (NMR) is a radio frequency spectroscopy technique. By exciting atomic nuclei into higher Zeeman energy levels and subsequently monitoring the evolution of the system, the technique is capable of elucidating atomic-level details of the system. Standard NMR measurements can reveal information about a sample's chemical composition, physical state and the relative location and dynamics of different components of a heterogeneous system.

In this section, the essential ideas of NMR relevant to the current work will be covered, drawing on the texts of Slichter [45] and Abragam [46], unless otherwise noted. The reader is referred to these texts, and other works referenced here, when more detail is needed.

2.1. Nuclear Paramagnetism

When a system possesses both a magnetic moment, $\vec{\mu}$, and an angular momentum, $\vec{L}$, magnetic resonance can be observed. If a magnetic field is present, there will be an interaction energy between $\vec{\mu}$ and the field, $\vec{H}_0$, represented by the Hamiltonian,

$$\boldsymbol{H}_{Zeeman} = -\vec{\mu} \cdot \vec{H}_0 \tag{1}$$

This defines the Zeeman Hamiltonian for the described system. In the quantum picture, the angular momentum will be quantized as integer or half-integer multiples of $\hbar$,

$$\vec{L} = \hbar \vec{I} \tag{2}$$

where I is the nuclear spin quantum number, or simply spin, and $\vec{I}$ is the nuclear spin operator. $\vec{\mu}$ and $\vec{I}$ are related according to,

$$\vec{\mu} = \hbar \gamma \vec{I} \tag{3}$$

where γ is the gyromagnetic ratio, which has units of MHz per Tesla or radians per second per Tesla. Combining these equations and arbitrarily assigning the magnetic field to be along the z-direction (a common convention that will be continued throughout this discussion) leaves equation (1) in the form,

$$\boldsymbol{H}_{Zeeman} = -\gamma \hbar H_0 I_z \tag{4}$$

The expectation values of this Hamiltonian, in the basis set defined by the eigenstates of the I_z operator, define the Zeeman energy levels for the system as

$$\begin{gathered} E_{Zeeman} = -\gamma \hbar H_0 m \\ m = -I, -I+1, \ldots, I-1, I \end{gathered} \tag{5}$$

The separation between adjacent energy levels is thus $\gamma\hbar H_0$. If we define an angular frequency as

$$\omega = \gamma H_0 \tag{6}$$

then the separation becomes $\hbar\omega$ and we have defined the frequency of a photon required to cause a transition to an adjacent energy level.

In a macroscopic sample, the Boltzmann law describes how the spins will distribute themselves among the energy levels of equation (5). Therefore, the relative population of each level can be written as

$$P_m \propto e^{\frac{\gamma \hbar m H_0}{k_B T}} \tag{7}$$

This proportionality points to the fact that there will be more spins in the lower energy states, as expected, which correspond with higher values of m. In states with positive m, the z-component of magnetic moment is parallel with the magnetic field, while those with negative m have it anti-parallel. Therefore, at equilibrium, a net magnetization will develop in the z-direction, collinear with the external magnetic field. The net magnetization is explicitly given by summing over all values of m,

$$\vec{M} = N\gamma\hbar \frac{\sum_{m=-I}^{I} m\, e^{\frac{\gamma\hbar H_0}{k_B T}}}{\sum_{m=-I}^{I} e^{\frac{\gamma\hbar H_0}{k_B T}}} \hat{z} \tag{8}$$

where N is the total number of spins in the system. The Zeeman energy in a system is small compared to the thermal energy, and so the above can be simplified to:

$$\vec{M} = \frac{N\gamma^2\hbar^2 I(I+1) H_0}{3 k_B T} \hat{z} \tag{9}$$

Having arrived at this net magnetization for the spin system, a classical discussion can be carried out to describe the interaction between the magnetic moments comprising the spin system and any applied magnetic fields.

2.2. Time Dependence of Spins

The above discussion describes how a net magnetization vector, $\vec{M}$ is generated in a system of spins. While the magnitude of $\vec{M}$ contains information on the number of spins present, provided the other details in equation (9) are known, the time dependence of $\vec{M}$ is much more informative, particularly following a perturbation to the spin system. The primary source of time-dependent behavior for a nuclear magnetic moment is interactions with magnetic fields.

When subject to a magnetic field, $\vec{H}$, a magnetic moment, $\vec{\mu}$ will experience a torque defined by,

$$\vec{\tau} = \vec{\mu} \times \vec{H} = \frac{d\vec{L}}{dt} \tag{10}$$

Applying equations (2) and (3), as well as defining an angular frequency as,

$$\vec{\omega} = \gamma \vec{H} \tag{11}$$

similar to equation above, then equation (10) simplifies to,

$$\frac{d\vec{\mu}}{dt} = \vec{\mu} \times \vec{\omega} \tag{12}$$

Therefore, when $\vec{\mu}$ has a component perpendicular to $\vec{H}$, $\vec{\mu}$ will precess about the axis defined by $\vec{H}$ at a frequency given by equation (11). This precessional motion applies both to the individual nuclear magnetic moments of a sample in a static field, as well as the net magnetization vector, $\vec{M}$, described in equations (8) and (9). It is important to note that the frequency of motion is equal to the frequency defined by the separation of adjacent energy levels in this system.

Since, at thermal equilibrium, $\vec{M}$ is collinear with the main field, $\vec{H}_0$, it remains stationary. If however an additional magnetic field, $\vec{H}_1$, is applied, at an angle to the main field, then $\vec{M}$ will begin to precess about the sum of these two fields,

$$\vec{H}_{tot} = \vec{H}_0 + \vec{H}_1 \tag{13}$$

In conventional NMR, $\gamma \vec{H}_0 \approx 1 - 1000$ MHz and $\gamma \vec{H}_1 \approx 1 - 100$ kHz. Therefore, the subsequent motion of $\vec{M}$ due to $\vec{H}_{tot}$ will be dominated by a rapid precession about $\vec{H}_0$ in the stationary or laboratory frame of reference. Consequently, it is common practice to carry out any further discussion in a rotating reference frame. It can be shown that the equation of motion for $\vec{\mu}$ in this rotating frame is the same as equation (12), as long as the actual field $\vec{H}_{tot}$ is replaced by an effective field,

$$\vec{H}_{eff} = \vec{H}_0 + \vec{H}_1 + \frac{\vec{\Omega}}{\gamma} \tag{14}$$

where $\vec{\Omega}$ is the angular velocity of the rotating frame with respect to the static, laboratory frame. This

suggests that shifting into the rotating frame has the same effect as applying an additional field in the same direction as $\vec{\Omega}$. It follows that $\vec{\Omega}$ can be chosen to cancel $\vec{H}_0$, leaving $\vec{H}_{eff}=\vec{H}_1$, so that in the rotating frame, the discussion of the time dependence of $\vec{M}$ is greatly simplified.

Now operating in the rotating reference frame, we can more easily interpret the return of a system to equilibrium following a perturbation by an applied magnetic field. A logical choice is to apply $\vec{H}_1$ as a field rotating with the same angular velocity as the rotating frame, since this will simplify its representation in the rotating frame, and therefore the subsequent motion it brings about, as well as being the required frequency to cause resonant energy level transitions. The application of such a field will cause $\vec{M}$ to precess about $\vec{H}_1$ at a angular frequency γH_1. By varying the time, t, the field is applied for, the angle that the magnetization is tipped away from its equilibrium direction can be controlled. This tip angle is given by,

$$\theta=\gamma H_1 t \tag{15}$$

Following such a pulse, the system will be left in a non-equilibrium state. Continuing the convention of placing the main field in the z-direction, we will specify two relaxation times, T_1 and T_2, for the parallel and perpendicular components respectively, to return to equilibrium. The distinction between the two comes from the fact that changes in $\vec{M}$ along the direction of quantization, M_z or the longitudinal magnetization, correspond to a change in energy, while changes in M_x or M_y, the transverse magnetization, do not. The mechanistic origins of these relaxation times will be discussed later. For now, we will view them simply as characteristic decay times, as a number of useful results follow, regardless of their origin. At thermal equilibrium, the magnetization is given by equation (9), which can be simplified to,

$$\vec{M}=M_0\hat{z} \tag{16}$$

This implies that following perturbation, M_x and M_y will decay to zero and M_z will approach M_0. Combining these decay concepts with the motion defined by equation (12), expressed slightly differently, we arrive at a set of equations that effectively model the time dependence of the magnetization, the Bloch equations,

$$\frac{dM_x}{dt} = \gamma(\vec{M} \times \vec{H})_x - \frac{M_x}{T_2} \tag{17a}$$

$$\frac{dM_y}{dt} = \gamma(\vec{M} \times \vec{H})_y - \frac{M_x}{T_2} \tag{17b}$$

$$\frac{dM_z}{dt} = \gamma(\vec{M} \times \vec{H})_z + \frac{M_0 - M_z}{T_1} \tag{17c}$$

It should be emphasized that these equations are a model of how magnetization evolves in an NMR experiment. In this model, both the longitudinal and transverse magnetization have been chosen to decay exponentially. While this choice can be justified for the longitudinal decay from the atomic theory of absorption, the same is not true for the transverse decay; it is mainly a very useful postulate. In fact, the transverse decay in some cases can be better modeled with a Gaussian decay or Gaussian-damped sinc function.

Choosing the applied field, $\vec{H}_1$, to be stationary along the x-direction of the rotating reference frame and ignoring any transients in the signal, then the following solutions to the above equations can be found:

$$M_x = \kappa \gamma H_1 (\omega_0 - \omega) T_2^2 M_0 \tag{18a}$$

$$M_y = \kappa \gamma H_1 T_2 M_0 \tag{18b}$$

$$M_z = \kappa \left(1 + (\omega_0 - \omega)^2 T_2^2\right) M_0 \tag{18c}$$

$$\text{where, } \kappa^{-1} = 1 + (\omega_0 - \omega)^2 T_2^2 + \gamma^2 H_1^2 T_1 T_2 \tag{18d}$$

In the above equations, ω_0 is the precessional frequency of the spins in the main field and ω is that of the rotating frame with respect to the lab frame, and so also the frequency of the applied

radiofrequency pulse. If saturation is avoided (ie. $\gamma^2 H_1^2 T_1 T_2 \ll 1$) then M_x and M_y have the form of the dispersion and absorption, respectively, of a Lorentzian line.

Typically the axis 90° out of phase with the applied pulse is detected, because following a pulse with a tip angle of 90°, the entirety of $\vec{M}$ lies on this axis. In the above case, this is M_y. Finding the full width at half maximum of equation (18b) gives,

$$\Delta \omega_{\frac{1}{2}} = \frac{2}{T_2} \sqrt{1 + \gamma^2 H_1^2 T_1 T_2} \tag{19}$$

This result shows that the width of a signal in the frequency domain is independent of the main field, $\vec{H}_0$. If we again avoid saturation, we arrive at a simple equation for T_2,

$$T_2 = \frac{2}{\Delta \omega_{\frac{1}{2}}} \tag{20}$$

We can obtain a similar result by setting ω to ω_0, which simplifies equations (17a-c), leaving the time dependence of M_x and M_y as exponential decays, with a phase difference between them based on initial conditions of the solutions. The Fourier transform of M_y will therefore be a Lorentzian distribution, again whose width is related to T_2.

Equation (20) is an interesting result. It suggests a spread in frequencies as a possible source or cause of the spin-spin relaxation time, T_2. Recalling equation (11), we know that the frequency of a spin's precession is related to the magnitude of the field it is experiencing. Besides the main and applied fields, there are a number of sources of magnetic fields that in fact originate from within the sample itself. Two major contributors are the currents set up by the circulating electrons, leading to the so-called chemical shift, and the dipole interaction between a spin and the distribution of magnetic dipole moments within the sample. These effects will be discussed in the following sections.

2.3. Chemical Shift

The presence of the electrons, which have been ignored up until this point, can have a significant impact on the local field experienced by a nucleus and therefore on its Zeeman energy levels. Their influence on the nucleus can be carried out by both the electric field generated by the electron being a charge carrier, and the magnetic fields brought about by the particle's orbital motion and its intrinsic magnetic moment. Nuclei with $I > ½$ possess an electric quadrupole moment, which can be acted on by the electron's electric field, generating a torque. This effect is referred to as the quadrupolar interaction. The electronic magnetic moment, μ_e, is mainly relevant in metals and paramagnetic materials. The μ_e of the unpaired electrons in these situations are polarized by H_0, and are coupled to nuclei via the hyperfine interaction. The resulting shift in the nuclear resonant frequency is known as the Knight shift in metals and the paramagnetic shift in paramagnetic materials. There is also indirect nuclear coupling that is brokered by electrons, though this causes subtle, hyperfine structure in the energy levels, mainly visible in high resolution NMR of liquids. When observing resonance of a proton, a spin ½, non-metal nucleus, the most significant change in energy levels is caused by the field generated by the orbital motion of the electron, an effect known as the chemical shift.

The principle behind the chemical shift is quite simple: electrons orbiting the nucleus establish a magnetic field, ΔH, which contributes to the field seen by the nucleus, thus changing the resonant frequency given in equation (11) to,

$$\omega = \gamma(H_0 + \Delta H) \tag{21}$$

The size of the shift will depend on the details of the electron motion, which is determined in part by the orbital the electron is occupying and the environment in close proximity. The latter influence is related to the etymology of the term chemical shift, since different molecules will present different

electronic environments to resonant nuclei. For example, the electrons surrounding a proton of a water molecule will produce a different electronic environment than the electrons surrounding a methyl group's proton because of its different number, distribution and type of atoms.

Approached classically, the magnetic field generated at the origin by a charged particle at $\vec{r}$ with a velocity $\vec{v}$ and a charge q is given by,

$$\vec{H} = \frac{q}{c}\frac{\vec{r}\times\vec{v}}{r^3} = \frac{q}{mc}\frac{\vec{L}}{r^3} \tag{22}$$

Calculating this value for electrons with non-zero angular momentum (ie. all those other than the s-states) results in magnetic fields on the order of tens to hundreds of Teslas, which is obviously erroneous for the systems under question. It can be shown that the problem with this approach is that it does not take into account that the angular momentum becomes "quenched". More specifically, the expectation values of all components of the angular momentum operator are zero when the crystalline electric field leaves electron orbitals with the same azimuthal quantum number non-degenerate. Therefore, a more careful, quantum-mechanical treatment is needed.

The Hamiltonian for a charged particle in a magnetic field is given by,

$$\boldsymbol{H} = \frac{1}{2m}\left(\vec{p} - \frac{q}{c}\vec{A}\right)^2 + V \tag{23}$$

where $\vec{A}$ is the magnetic vector potential of the magnetic field, $\vec{p}$ is the operator $(\hbar/i)\vec{\nabla}$, and V is the sum of all the scalar potentials, including those from crystalline electric fields. When considering an atom's electron, the total vector potential will be the sum of the potentials due to the main field, $\vec{A_0}$, and the nucleus, $\vec{A_n}$. We can choose the latter to be,

$$\vec{A}_n = \frac{\vec{\mu} \times \vec{r}}{r^3} \tag{24}$$

since this potential will generate the appropriate dipole field. Defining a new Hermitian operator

$$\vec{\pi} = \vec{p} - \frac{q}{c}\vec{A}_0 \tag{25}$$

and expanding the Hamiltonian, ignoring higher order terms of $\vec{A}_n$ since $\mu_n \ll \mu_e$, leaves,

$$\boldsymbol{H} = \frac{1}{2m}\pi^2 + V - \frac{q}{2mc}\left(\vec{\pi}\cdot\vec{A}_n + \vec{A}_n\cdot\vec{\pi}\right) \tag{26}$$

The first two terms are equivalent to the Hamiltonian of an isolated electron in a magnetic field, while the other is the nuclear coupling term. Identifying the interaction between the nucleus and the electron as a perturbation to the electron's states, the energy of the coupling can be calculated using first order perturbation theory,

$$E_{pert} = \frac{-1}{c}\int \vec{A}_n \cdot \vec{j}_0 \, d\tau \tag{27}$$

The resulting quantity $\vec{j}_0$ is the current density, which is defined by,

$$\vec{j}_0(\vec{r}) = \frac{q}{2m}\frac{\hbar}{i}(\psi^* \nabla \psi - \psi \nabla \psi^*) - \frac{q^2}{mc}\vec{A}_0 \psi^* \psi \tag{28}$$

This can be recognized as being just the charge times the quantum mechanical probability density. Substituting equation (24) into (27) leaves the equation for the magnetic field due to the electron current density as,

$$\Delta \vec{H} = \frac{1}{c}\int \frac{\vec{r} \times \vec{j}_0(\vec{r})}{r^3} d\tau \tag{29}$$

Equation (29) describes the field generated by an electron at the location of the nucleus, given

knowledge of j_0. Therefore, the problem of analytically determining chemical shifts is essentially a problem of calculating the above integral, after determining j_0 from equation (28), which in turn is a problem of finding the appropriate wavefunctions. Simple, model examples can be solved to reasonable satisfaction by making several approximations, such as a p-state electron in a simplified crystalline field acted on by a static field. These zeroth order approximations can provide some insight into the general problem of chemical shielding calculations, such as showing the generation of both paramagnetic and diamagnetic currents. Inconsistencies arise, however, such as j_0 having non-zero divergence, thereby disobeying continuity, due to a less than rigorous approach.

The above discussion is only for a single electron. The complexity of the problem becomes compounded with additional electrons. Therefore, this is a longstanding and continuing area of research. Lamb [47] was the first to discuss the internal magnetic fields generated at the nucleus by electrons acted on by an external field. Ramsay [48, 49] extended the discussion to molecules. Since then, with more complex scenarios being considered, determination of electron wavefunctions by numerical methods has become the norm [50].

The shift in field is found experimentally to be directly proportional to the main field, and so a constant of proportionality can defined by,

$$\Delta \vec{H} = -\sigma \vec{H}_0 \tag{30}$$

where the parameter σ is referred to as the shielding parameter. This dependence on H_0 makes it awkward to report a standard value of shift for a given substance since the field would also have to be stated. There is also no clear zero for the frequency domain. Therefore, the chemical shift, δ, is defined as the relative difference between the resonance frequency of a reference material, ω_{ref}, and that of a particular nucleus in a particular scenario, as shown in equation (31).

$$\delta = \frac{\omega - \omega_{ref}}{\omega_{ref}} \tag{31}$$

This field-independent quantity is how the NMR resonance of different materials in different environments is reported. Common shift references used are salts with well defined resonance peaks, like tetramethylsilane (TMS) and 4,4-dimethyl-4-silapentane-1-sulfonic acid (DSS), dissolved in deuterium or other proton-free liquids [51]. Relative chemical shift positions are designated as downfield for increasing chemical shift and upfield for decreasing chemical shift. This nomenclature originates in the correlation between the resonant frequency of a nucleus and the strength of the shielding field generated by the nucleus' electrons (ie. a stronger shielding field – upfield – leads to a lower resonant frequency, and thus a lower δ).

2.4. Dipolar Interaction

The coupling between magnetic dipoles is often the dominant interaction in a spin system, particularly for spin ½ systems, which lack an electric quadrupole moment. Investigating this interaction can therefore lead to a thorough understanding of nuclear relaxation.

The simplest approach and first approximation of the dipolar interaction and the resulting T_2, or spin-spin relaxation time, is to view the dipolar fields of each nuclear spin as simply adding to the local field experienced by all neighboring spins. Estimating the field due to a dipole as,

$$H_{local} = \frac{\mu}{r^3} \tag{32}$$

and taking order of magnitude approximations of μ and r to be 0.001 of the Bohr magneton and 2 Å, respectively, yields a local field on the order of ~ 0.1 mT. This means that the resonance condition is spread over a range of $\gamma H_{local} \approx 10$ kHz. If one considers the energy levels of such a system, the effect of this distribution of local fields will be to broaden the line defining the Zeeman energy level, as

illustrated in Figure 1.

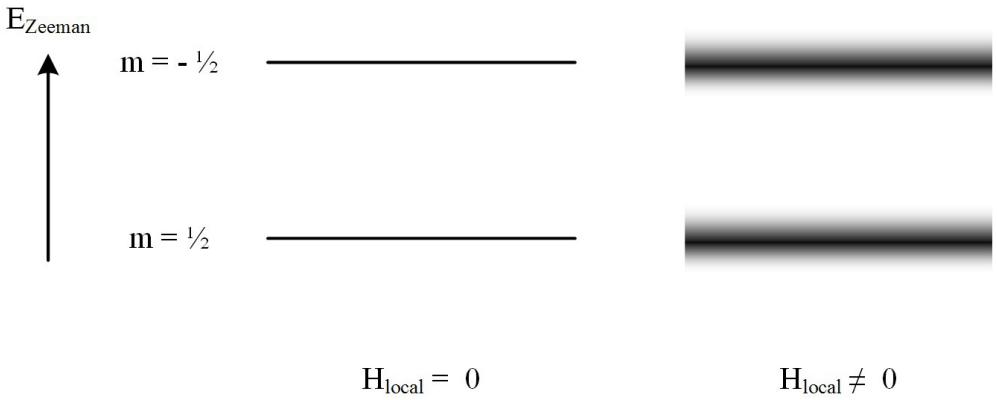

Figure 1: Illustration of the effect of the local dipolar field on the Zeeman energy levels in a spin ½ system.

The resonance line in the frequency domain will be similarly broadened, making this an approximation of T_2.

A more rigorous discussion requires looking at the energy of interaction between two magnetic dipoles,

$$E_D = \frac{\vec{\mu}_1 \cdot \vec{\mu}_2}{r^3} - \frac{3(\vec{\mu}_1 \cdot \vec{r})(\vec{\mu}_2 \cdot \vec{r})}{r^5} \tag{33}$$

This will provide the Hamiltonian of interaction. Applying equation (3), expanding the scalar products and expressing the position vector pointing from one dipole to the other in polar coordinates, with the direction of the main field defining the z-axis, yields,

$$\begin{aligned} \boldsymbol{H}_D &= \frac{\gamma^2 \hbar^2}{r^3}(\boldsymbol{A}+\boldsymbol{B}+\boldsymbol{C}+\boldsymbol{D}+\boldsymbol{E}+\boldsymbol{F}) \\ \boldsymbol{A} &= \boldsymbol{I}_{1z}\boldsymbol{I}_{2z}(1-3\cos^2\theta) \\ \boldsymbol{B} &= \frac{1}{2}(1-3\cos^2\theta)(\boldsymbol{I}_{1z}\boldsymbol{I}_{2z}-\vec{\boldsymbol{I}}_1\cdot\vec{\boldsymbol{I}}_2) = -\frac{1}{4}(1-3\cos^2\theta)(\boldsymbol{I}_{1+}\boldsymbol{I}_{2-}+\boldsymbol{I}_{1-}\boldsymbol{I}_{2+}) \\ \boldsymbol{C} &= \boldsymbol{D}^* = -\frac{3}{2}\theta\cos\theta e^{-i\phi}(\boldsymbol{I}_{1z}\boldsymbol{I}_{2+}+\boldsymbol{I}_{2z}\boldsymbol{I}_{1+}) \\ \boldsymbol{E} &= \boldsymbol{F}^* = -\frac{3}{4}\sin^2\theta e^{-2i\phi} \end{aligned} \tag{34}$$

The effect of each of the terms in equation (34) can be explained best using the Slichter diagram shown in Figure 2. The composite states used to describe the two-spin system are denoted by + and – for spin up ($m_i = +½$) and spin down ($m_i = –½$), respectively. So, for example, + – and – + are for the two degenerate states with one spin in each state.

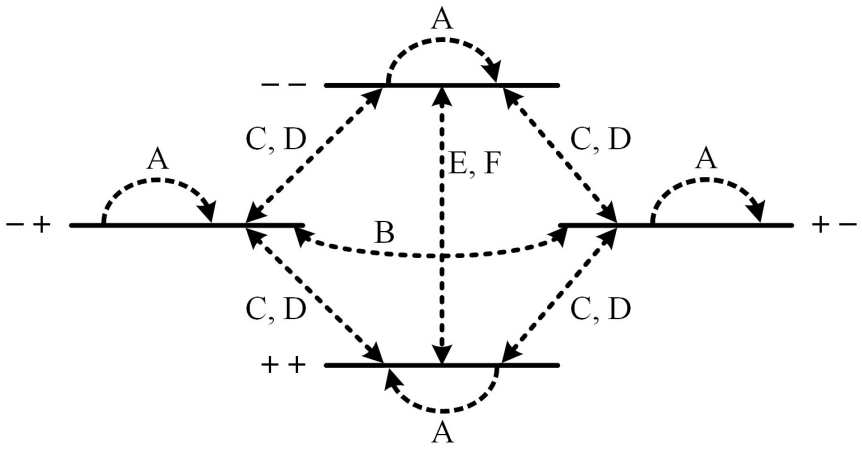

Figure 2: Slichter diagram of energy level transitions due to the dipolar interaction. Each transition, identified with a dashed line, is labeled with the term from the dipolar Hamiltonian (equation (34)) that causes it. Reproduced from reference [45].

The terms of equation (34) are separated based on the types of operators, and therefore the types of possible transitions. The ***A*** term is a completely diagonal operator and connects the Zeeman energy levels to themselves, that is $|m_1, m_2\rangle$ to $\langle m_1, m_2|$. Term ***B***, has off-diagonal elements connecting the two degenerate energy levels, permitting transitions from $|m_1, m_2\rangle$ to $\langle m_1+1, m_2-1|$ and $\langle m_1-1, m_2+1|$. Both ***A*** and ***B*** describe energy conserving transitions. Terms ***C*** and ***D*** connect $|m_1, m_2\rangle$ to $\langle m_1 \pm 1, m_2|$ or $\langle m_1, m_2 \pm 1|$ involving single-quantum transitions. Finally, the ***E*** and ***F*** terms connect $|m_1, m_2\rangle$ to $\langle m_1+1, m_2+1|$ or $\langle m_1-1, m_2-1|$ involving double-quantum transitions. Only ***C***-***F*** cause transitions between states of different energy, meaning that, although the ***B*** term is off-diagonal in the

$|m_1, m_2\rangle$ representation, it would be diagonal in the proper zero-order basis. Therefore, treating terms ***C*-*F*** as a perturbation, the admixture of other states into a given zero-order state is permitted, not just single spin flips, but also double spin flips, via terms ***E*** and ***F***. The admixture of unperturbed states into the exact state for a given perturbation, $\boldsymbol{H}_{pert}$ is, according to second order perturbation theory,

$$|n\rangle = |n_0\rangle + \sum_{n'} \frac{\langle n'|\boldsymbol{H}_{pert}|n\rangle}{E_n - E_{n'}} \tag{35}$$

The numerator of the summation term can be approximated as the coefficient of equation (34), since terms ***A*-*F*** are on the order of one,

$$\langle n'|\boldsymbol{H}_{pert}|n\rangle = \langle n'|\boldsymbol{H}_{D}|n\rangle \approx \frac{\gamma^2 \hbar^2}{r^3} \tag{36}$$

recalling equation (32),

$$\langle n'|\boldsymbol{H}_{D}|n\rangle \approx \gamma \hbar H_{local} \tag{37}$$

The denominator in the summation term of equation (35) is simply the difference in Zeeman energy levels,

$$E_n - E_{n'} = \hbar \gamma H_0 \tag{38}$$

which leaves an approximation of how much of the states are admixed,

$$\frac{\langle n'|\boldsymbol{H}'|n\rangle}{E_n - E_{n'}} \approx \frac{H_{local}}{H_0} \approx \frac{0.1\,mT}{1\,T} = 10^{-4} \tag{39}$$

This small effect leads to a small amount of absorbance at the normally forbidden frequencies of $\omega = 0$ and $\omega = 2\omega_0$. These small corrections to the unperturbed states, and their causes, can be ignored for our purposes. Therefore the ***C*-*F*** terms will be dropped, leaving the truncated dipolar Hamiltonian,

$$\boldsymbol{H}_{\boldsymbol{D}}^{\boldsymbol{0}}=\frac{\gamma^2\hbar^2}{r^3}(\boldsymbol{A}+\boldsymbol{B}) \tag{40}$$

Since $\boldsymbol{H}_z$ and $\boldsymbol{H}_{\boldsymbol{D}}^{\boldsymbol{0}}$ commute, there exist simultaneous eigenvectors of both. The states to use are the composite states, $|I\,m\rangle$, where $I\in[0,1]$ and $m\in[-1,0,1]$ for two protons. The total Hamiltonian is then,

$$\begin{gathered}\boldsymbol{H}=\boldsymbol{H}_z+\boldsymbol{H}_{\boldsymbol{D}}\\ \text{with } \boldsymbol{H}_z=-\gamma\hbar(\boldsymbol{I}_{1z}+\boldsymbol{I}_{2z})\\ \text{and } \boldsymbol{H}_{\boldsymbol{D}}^{\boldsymbol{0}}=\frac{\gamma^2\hbar^2}{r^3}(\boldsymbol{A}+\boldsymbol{B})=\frac{1}{2}\frac{\gamma^2\hbar^2}{r^3}(1-3\cos^2\theta)(3\,\boldsymbol{I}_{1z}\boldsymbol{I}_{2z}-\vec{\boldsymbol{I}}_1\cdot\vec{\boldsymbol{I}}_2)\end{gathered} \tag{41}$$

Expanding the square of the total spin angular momentum operator,

$$\boldsymbol{I}^2=(\vec{\boldsymbol{I}}_1+\vec{\boldsymbol{I}}_2)^2=\boldsymbol{I}_1^2+\boldsymbol{I}_2^2+2\,\vec{\boldsymbol{I}}_1\cdot\vec{\boldsymbol{I}}_2 \tag{42}$$

leads to the energy levels of the coupled system:

$$\begin{aligned}\langle I\,m|\boldsymbol{H}_z|I\,m\rangle&=-\gamma\hbar H_0(m_1+m_2)=-\gamma\hbar H_0 m\\ \langle I\,m|\boldsymbol{H}_{\boldsymbol{D}}|I\,m\rangle&=\frac{1}{2}\frac{\gamma^2\hbar^2}{r^3}(1-3\cos^2\theta)\left[3\,m_1m_2-\frac{1}{4}\right]\end{aligned} \tag{43}$$

The resulting energy level diagram is shown in Figure 3.

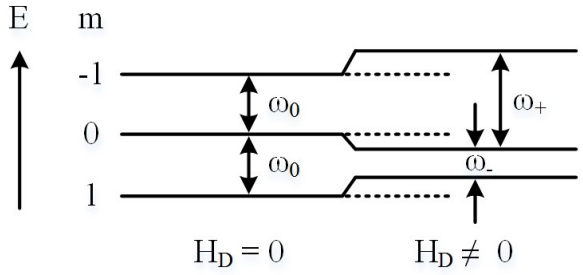

Figure 3: Zeeman energy level diagram for two protons without (left) and with (right) coupling through the dipolar interaction.

where,

$$\omega_{+/-} = \frac{1}{\hbar}\left[\gamma \hbar H_0 \pm \frac{3}{4}\frac{\gamma^2 \hbar}{r^3}(1 - 3\cos^2\theta)\right] \tag{44}$$

The resulting spectrum for this two spin system would appear as in Figure 4A. For a system of many spins, there will be a distribution of r and θ, which means there will be a broad distribution of ω, resulting in the spectrum shown in Figure 4B, demonstrating, qualitatively, how the dipolar interaction leads to a broadness of a resonance line. To quantitatively extract the T_2 from this distribution, Van Vleck's method of moments must be applied [45].

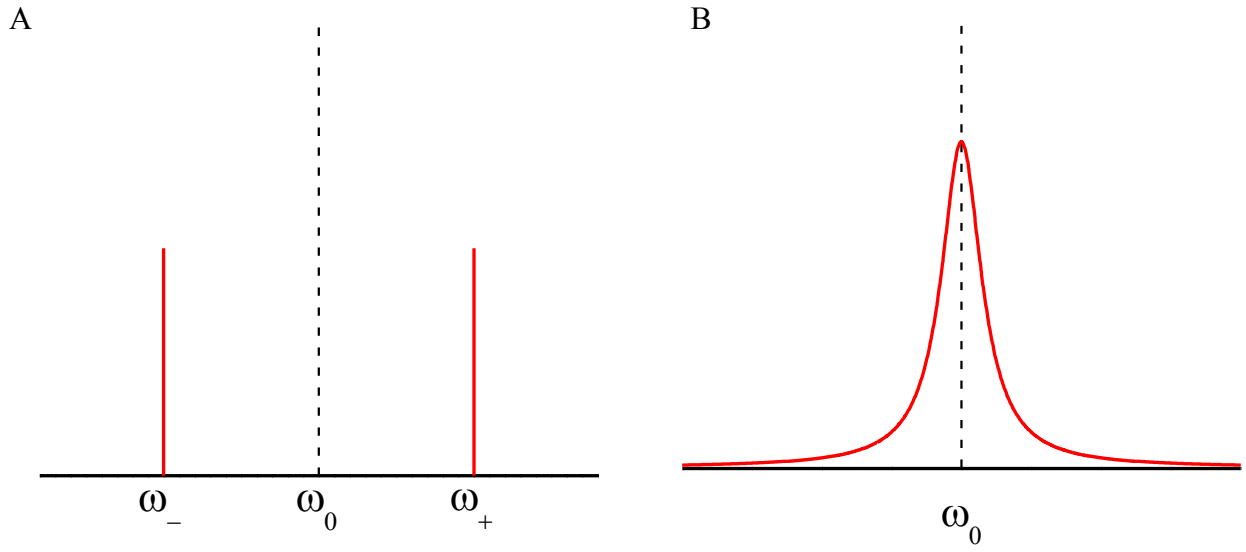

Figure 4: (A) Spectrum for a system of two protons coupled by the dipolar interaction. (B) The equivalent spectrum for many protons.

2.5. Magic Angle Spinning (MAS) NMR

The discussion in the previous section demonstrates how the dipolar interaction leads to the broadening of a resonance line in a NMR experiment. The truncated dipolar Hamiltonian, $\boldsymbol{H}_{\boldsymbol{D}}^{\boldsymbol{0}}$, in equation (40), contains the terms from the total $\boldsymbol{H}_{\boldsymbol{D}}$ responsible for this broadening, $\boldsymbol{A}$ and $\boldsymbol{B}$. Both of these terms contain a factor of $(1 - 3\cos^2\theta)$, where θ is the polar angle of the interaction vector between

two magnetic dipoles, with respect to the main field, H_0. For $\theta = 54.74°$, these terms go to zero, suggesting a way to effectively remove the dipolar interaction in a sample.

By rapidly rotating the sample about an axis tilted with respect to the main field, the interaction vector between spins becomes averaged, effectively allowing θ to be controlled. By setting the angle of sample rotation to the "magic angle", $\theta_M = 54.74°$, as illustrated in Figure 5, the dipolar interaction can be reduced to zero, provided the spinning is faster than the frequency defined by the dipolar field. Figure 6 shows the effect of MAS by comparing the spectra of a hydrated MCM-41 sample, with and without spinning.

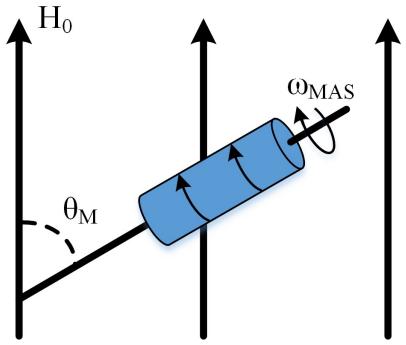

Figure 5: Diagram of magic angle spinning.

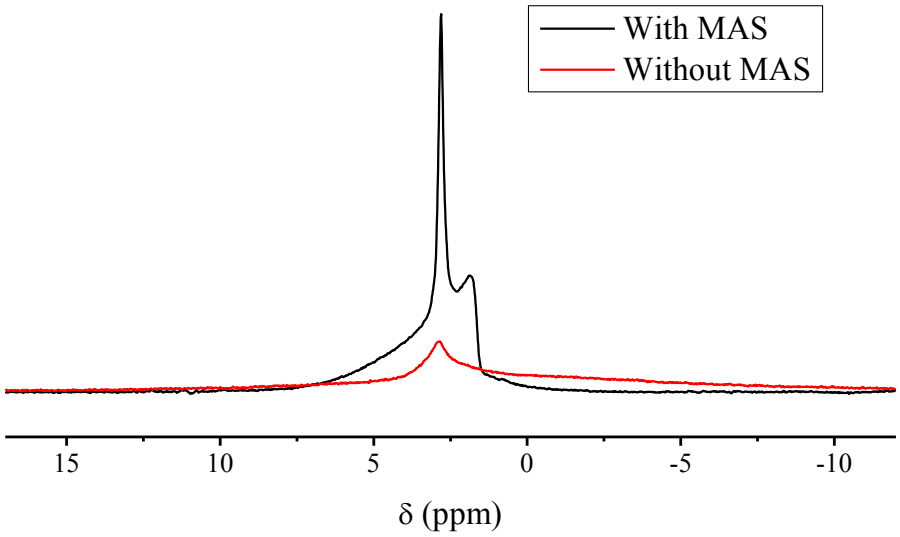

Figure 6: NMR spectra of a hydrated, pristine MCM-41 sample, both with (black) and without (red) MAS.

2.6. Basic Relaxation Theory

At equilibrium, the spin populations of a system, the relative population of each energy state, for a given temperature and main field strength, is described by equation (7). When the equilibrium changes, by a change in field for example, then the equilibrium population has changed. Specifically, for an increase in main field strength, fewer spins can populate the higher energy states. This means that to achieve equilibrium again following this change, some spins must move to a lower energy state.

A nuclear spin in a high energy state can relax to a lower energy state only by releasing energy, either by spontaneous or stimulated emission. At radio frequencies, the probability of the spontaneous emission of a photon is negligible [52]. For stimulated emission to take place, the spin must interact with a magnetic field fluctuating at its Larmor frequency. The energy is lost to the "lattice", which represents all non-spin degrees of freedom, such as thermal energy. The rate of energy loss is exponential with a time constant T_1, the spin-lattice relaxation time.

Any mechanism that generates a fluctuating magnetic field in the vicinity of a spin can cause it to relax, provided it is at the correct frequency. As mentioned previously, the dominant interaction mechanism for spin ½ systems is the magnetic dipole-dipole interaction between a nucleus and the magnetic dipoles of the surrounding atoms. It is a typical example used to develop and illustrate the connection between random molecular motion and nuclear relaxation.

The Hamiltonian describing the interaction between two magnetic dipoles is given in equation (34). The atoms that these spins are associated with will be undergoing motion due to the thermal energy they possess. The motion of the spins, and thus the values of r, θ and ϕ which describe the relative position of one spin with respect to another, will not be purely random. Instead there will be some probability that, if the relative position, and thus $\boldsymbol{H}_{\boldsymbol{D}}$, is found to have a given value at some time, t, it may have a value a time τ later that is still correlated with the value at t. A correlation function, $G(\tau)$, can be defined to describe this correlation (probability) as,

$$\begin{aligned} G(\tau) &= \overline{\langle \boldsymbol{H}_{\boldsymbol{D}}(t)\boldsymbol{H}^{*}_{\boldsymbol{D}}(t+\tau)\rangle} \\ G(\tau) &= \overline{\langle \boldsymbol{H}_{\boldsymbol{D}}(t)\boldsymbol{H}^{*}_{\boldsymbol{D}}(t)\rangle} F(\tau) \end{aligned} \tag{45}$$

where $F(\tau)$ is simply the normalized correlation function and the over bar indicates an ensemble average over the entire system. $F(\tau)$ will typically be a decaying function of time that will contain the correlation time, τ_c, which is the characteristic time between jumps or changes from one state to another.

The Fourier transform of $G(\tau)$ yields the power spectrum, or spectral density, $J(\omega)$,

$$J(\omega) = \int G(\tau) e^{(-i\omega\tau)} d\tau \tag{46}$$

This describes the relative presence of each frequency in the perturbation. In the case of dipole-dipole interactions, $J(\omega)$ describes the amplitudes of the frequency components of the fluctuating dipolar

fields, though this treatment can be generalized to any perturbing Hamiltonian. The amplitude of $J(\omega)$ at the Larmor frequency, ω_0, is given by the proportion of motion that is occurring at that frequency. The greater this amplitude, the more effective of a relaxation mechanism this perturbation is [52].

In equation (34), the position is described by second order spherical harmonics. Carrying out the integral of equation (46) on these harmonics yields terms of the form,

$$\frac{\tau_c}{1+\omega^2\tau_c^2} \tag{47}$$

Typical spectral density functions are shown in Figure 7. An important feature of $J(\omega)$ is that its integral over all frequencies does not depend on τ_c. This is easily shown by setting τ to zero in equation (46),

$$J(\omega)_{\tau=0} = \int \overline{\langle \boldsymbol{H}_{\boldsymbol{D}}(t)\boldsymbol{H}^{*}{}_{\boldsymbol{D}}(t)\rangle}\, F(0)\, d\tau \tag{48}$$

Since τ_c is contained in the $F(\tau)$ term, which reduces to one when τ is zero, the area of the $J(\omega)$ curve is constant with respect to τ_c.

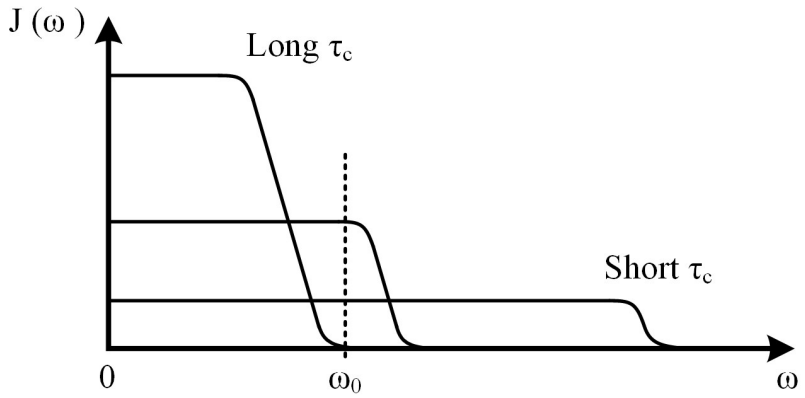

Figure 7: Typical spectral density functions. Each curve represents the spectral density at a different correlation time. Reproduced from reference [45].

The spectral density function will contain frequency components up to the order of τ_c^{-1}, as shown in Figure 7. As temperature increases, the motion becomes faster and the correlation time

decreases, since the molecules remain in their state for shorter times. This means that larger frequency components will be included in the spectral density, but, due to the fact that $J(\omega)$ is normalized by definition, the amplitude at each frequency must decrease in order for the area to remain constant. This means that the amplitude of $J(\omega)$ at the Larmor frequency will change, first being very small, sampling only the function's rapid falloff. As τ_c decreases, the amplitude at ω_0 will reach a maximum as it passes the shoulder of $J(\omega)$ and takes on the constant value for frequencies less than τ_c^{-1}. As τ_c decreases further, the frequency component at ω_0 will decrease again as $J(\omega)$ is spread over more frequencies.

The changes in the spectral density function with temperature explains the behavior of T_1 as described by Bloembergen, Purcell and Pound [53]. The calculation they outlined, referred to as the BPP theory, describes the relaxation effect of isotropic motion on identical spins on a liquid molecule. Their approach assumes that this motion is a Markoffian process, which means the normalized correlation function has the following form [45],

$$F(\tau)=e^{-\tau/\tau_c} \tag{49}$$

Their derivation uses time-dependent perturbation theory to derive a relationship between T_1 and $J(\omega)$ [46],

$$\frac{1}{T_1}=\frac{3}{2}\gamma^4\hbar^2\left\{J_1(\omega_0)+J_2(\omega_0)\right\} \tag{50}$$

For two like spins on the same liquid molecule, rotating randomly, the $J(\omega)$ from $\boldsymbol{H_D}$ is given by [46],

$$J_0(\omega)=6J_1(\omega)=\frac{3}{2}J_2(\omega)=\frac{24}{15r^6}\left(\frac{\tau_c}{1+\omega^2\tau_c^2}\right) \tag{51}$$

where the subscript 0 corresponds to terms $\boldsymbol{A}$ and $\boldsymbol{B}$ from $\boldsymbol{H}_D$; 1 to $\boldsymbol{C}$ and $\boldsymbol{D}$; and 2 to $\boldsymbol{E}$ and $\boldsymbol{F}$.

Combining the last two equations yields the standard equation for T_1^{-1} whose behavior as a function of τ_c is plotted in Figure 8. The correlation time can be replaced as the independent variable by T^{-1}, the inverse temperature, by assuming an Arrhenius behavior for τ_c as,

$$\tau_c = \tau_0 e^{\frac{E_a}{RT}} \tag{52}$$

where τ_0 is a constant amplitude factor, R is the ideal gas constant and E_a is the activation energy for the motion.

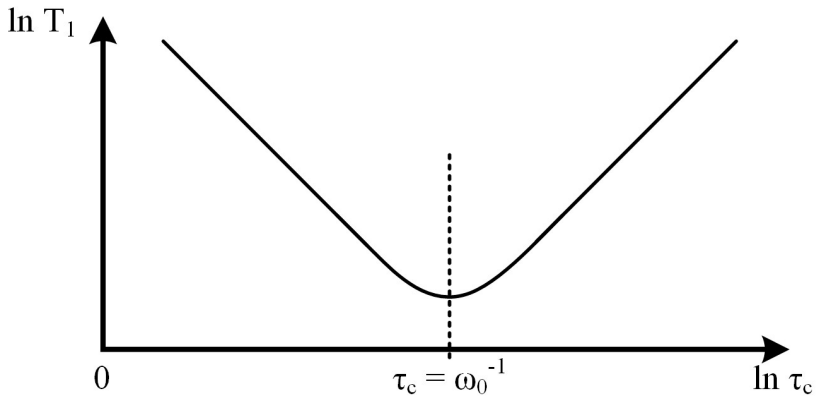

Figure 8: Plot of the T_1 relaxation time as a function of correlation time. Note that the minimum occurs at the correlation time corresponding to the inverse of the Larmor frequency. Reproduced from reference [45].

The minimum in the graph of Figure 8 occurs at the correlation time that is equal to the inverse of ω_0. This can be deduced from equation (50), since this is the frequency at which $\Sigma_i J_i(\omega)$ is at its maximum, so the system relaxes fastest when the component of the dipolar fields at the Larmor frequency is at its maximum amplitude. From an experimental perspective, this suggests that relaxation experiments will be most sensitive to changes in species that have correlation times roughly equal to ω_0^{-1}. By changing ω_0, the experiment will be sensitive to different τ_c, and thus different time-scales of motion which could possibly distinguish different spin environments.

2.7. Magnetization Exchange in Heterogeneous Systems

When a system consists of a single type of spin group, that is, all of the spins are in equivalent environments, the magnetization of the group will decay as a whole towards thermal equilibrium with a single exponential decay time. An example of this would be the protons in a pure water sample; each hydrogen atom experiences the intramolecular environment due to the oxygen and the other hydrogen on the same water molecule as well as the environment due to the oxygen and hydrogen atoms on other water molecules undergoing rapid molecular motion.

More than one spin group exists when there are atomic nuclei located in multiple, distinct chemical or physical environments. A two site system could be comprised of water and a solid material such as tissue. The protons on these two groups would have distinct T_1 and T_2 values because of: a) the different types of motion they undergo, and b) their different molecular structures, with concomitant differences in their molecules' arrangements of internuclear vectors; the water molecules undergoing rapid motion compared to the more rigid macromolecules that make up an extracellular matrix, for example. The water group in this scenario would likely be further separated into two groups since the water closest to the tissue components will interact strongly with it and have its motion restricted compared to the remaining bulk water. Following excitation, these three groups of spins will not only lose magnetization to the lattice, but will also transfer or exchange it among themselves.

There are three categories of magnetization exchange mechanisms: physical, chemical and magnetic. Each of these mechanisms has the same result, the transfer of spin energy from the constituents of one group to another. Physical exchange is the diffusion of a spin-bearing molecule from one environment to another. In the above example of the tissue-water system, this type of exchange would occur between the two water groups. The surface interactions are not strong enough

to bind the water molecule for a time that is long on the scale of an NMR experiment (~ milliseconds); a surface-associated water can diffuse away from the tissue component and enter the bulk water group, carrying magnetization with it, and its place at the surface being filled by a water molecule from the bulk.

Chemical exchange involves the breaking of chemical bonds to exchange the spin-bearing atom between molecules of different spin groups. This could occur between the hydroxyl protons of tissue macromolecules and water protons. Intermediate hydrogen bonding lowers the activation energy for this reaction, making it an efficient exchange mechanism under the right conditions (concentration, temperature, etc.).

The **B** term of the dipolar Hamiltonian in equation (34) describes the so-called spin "flip-flop". That is, this term generates transitions for a two-spin system to states where one spin is in a lower state and the other is in a higher state, that is, transitions from $|m_1, m_2\rangle$ to $|m_1-1, m_2+1\rangle$. This can be seen as an exchange of Zeeman magnetization from spin 1 to spin 2. This is magnetic exchange and can occur between any pair of spins provided they are in close proximity.

The process of exchange between two spin groups, labeled A and B, is mathematically described by a form of the Bloch equations (17), modified for exchange,

$$\begin{aligned} \frac{dM_A}{dt} &= -R_A M_A + k(M_B - M_A) \\ \frac{dM_B}{dt} &= -R_B M_B + k(M_A - M_B) \end{aligned} \tag{53}$$

where M_i and R_i are the magnetization and relaxation rate (= $1/T_1$) of group i. The constant k is the exchange rate. The formulation of this equation is basically a bookkeeping exercise, simply equating the change in magnetization with a tally of the sources of magnetization losses and gains. In this two-

site example, group A loses magnetization via relaxation to the lattice ($-R_A M_A$) and to group B via exchange ($-kM_A$). The only source of gain in magnetization is from exchange with group B ($+kM_B$).

To consider the effect of exchange in the frequency domain, the transverse relaxation behavior must be included in the analysis,

$$M_A = M_{A0} e^{i\omega_A t} e^{t/T_2} \tag{54}$$

Ernst thoroughly covers the solutions to the Bloch equations in both one and two dimensions in his book [54]. The effect of exchange on a NMR spectra is summarized in Figure 9. Two columns of spectra are shown, each representing a different system of two spin reservoirs. The spectra on the right are for a system with an even (1:1) distribution between the two spin groups, while on the left are for a system with a 3:1 ratio of spin groups. Each row contains spectra for each system modeled with a different exchange rate, starting with an exchange rate of zero. The effect seen, with increasing exchange rate, is the resonance peaks broaden, coalesce into a single peak, then sharpen again, at a frequency equal to the weighted average of the original frequencies of the two spin groups.

$$\delta = \delta_a p_a + \delta_b p_b \tag{55}$$

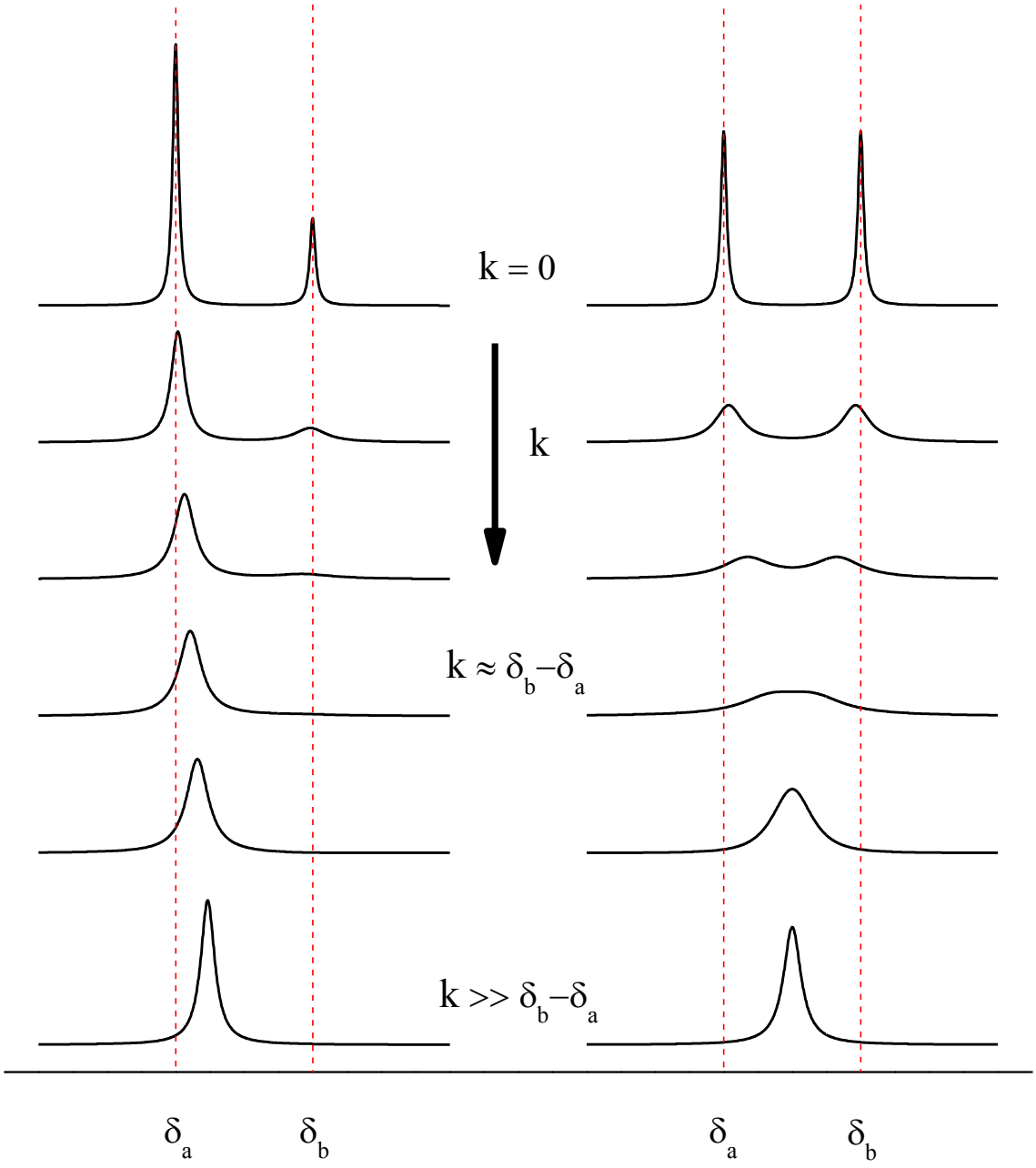

Figure 9: Effect of exchange on the NMR spectrum of a system with two spin environments. On the right are spectra for a system where the relative size of the two groups is equal (ie. 1:1 spin population ratio). On the left are spectra for an uneven spin distribution (3:1 ratio). The spectra in the top row are the intrinsic spectra (ie. no exchange) and the exchange rate increases with each subsequent row of spectra.

3. Spillover

The reduction of yellow WO_3 to blue W_4O_{11} by H_2 gas normally proceeds at temperatures above 400° C. In 1964, Khoobiar [1] reported the color change occurring at room temperature when an alumina-supported Pt catalyst was mechanically mixed with the WO_3. H_2 gas was already known to dissociatively chemisorb on Pt group metals, so the effect was attributed to the transfer of hydrogen, either in atomic or ionic form, from Pt to WO_3 via the alumina support. Boudart [2] later introduced the term "spillover" to describe this transfer of hydrogen. Since these early reports, further work has shown that the spillover mechanism is not limited to this one system, but is in fact a more general phenomenon. There are four main reviews on the topic of spillover [3 – 6] that cover all aspects of spillover, with an emphasis on hydrogen spillover. This section will summarize some of the key points on the topic found in these reviews and elsewhere.

Spillover is broadly defined as "the transport of active species sorbed or formed on one phase to another phase which does not sorb or generate these species under the given conditions" [5]. This simple definition outlines the three main players in a spillover mechanism: i) the spillover species, which is the active species being transported; ii) the spillover initiator, which is the first phase, or initial site of formation for the spillover species; and finally, iii) the destination for the spillover species, referred to as the spillover acceptor. Outside of these three elements of spillover, there are several other factors that have been reported to affect the process. Co-adsorption of different species has been shown to be important. CO and O can inhibit spillover, while water has been shown to be a spillover promoter in many systems, increasing the rate of spillover or lowering the activation energy [5, 55]. For example, spillover on perfectly dry WO_3 proceeds at 100° C, while co-adsorption of water lowers this so the reaction takes place at room temperature.

It has been shown that the three primary parts of the spillover process, mentioned in the above

paragraph, are in fact much broader categories than what was first discovered by Khoobiar, though there is significant disagreement about just how broad. It is generally well agreed upon that species other than H can be the spillover species. O, N, CO and NCO have all be shown to be capable of participating in spillover. Not just Pt group metals but any hydrogenation catalyst can act as a spillover initiator. Perhaps the most supported aspect of spillover is that the first step of the process is dissociative adsorption of the spillover species onto the initiator, usually starting as a diatomic molecule and ending as a covalently bound atom. But here, all consensus ends.

The latter parts of the spillover process are surrounded in the greatest debate. The exact mechanism of how the spillover species travels from the initiator to the acceptor, what form it takes at the location of the acceptor, and especially what substances can act as acceptors, are argued points. Based on the contents of the most recent review by Prins [6], spillover research has suffered greatly by premature claims of spillover as an explanation for an observed effect. This has resulted in contradicting conclusions becoming common, making it difficult to make concrete progress on the problem of spillover. This suggests that the area may be advanced the most by dispelling false claims of spillover. This is how Prins proceeds in his review article, not only summarizing a number of results, but drawing attention to a number of inconsistencies and highlighting research that supports definitive, logical resolutions.

Two major conclusions or statements that Prins makes in his review article are: certain experiments, such as protium-deuterium (H-D) exchange, are not indicators of spillover, and spillover to nonreducible acceptors is highly improbable, if not impossible. His article focuses specifically on hydrogen spillover, but many of his points are applicable to the universal problems of spillover. The former point is mostly relevant for the sake of the latter.

Many studies have used the exchange of H from a surface hydroxyl group with D from D_2 gas

as evidence for spillover to have occurred in nonreducible supports such as alumina, silica and magnesia. Prins argues that there are other mechanisms that can account for these results. The observation is typically made via infrared spectroscopy, where absorption bands corresponding to OH bonds disappear in proportion to the appearance of OD bands. Instead of this being spillover, Prins draws on a mechanism first proposed by Dalla Betta et. al. [56]. It suggest that the effect could simply be due to chemical exchange, where a D bonded to an initiator, which we will assume is a metal for the sake of example, exchanges with a H on a water molecule, forming HDO. This molecule could then travel to the site of a surface hydroxyl group through either the adsorbed phase or the vapor phase, and finally exchange its D for the H of the hydroxyl group. This process is illustrated in Figure 10. While H-D exchange has occurred, this is not a spillover process, since there is no net transport of the spillover species.

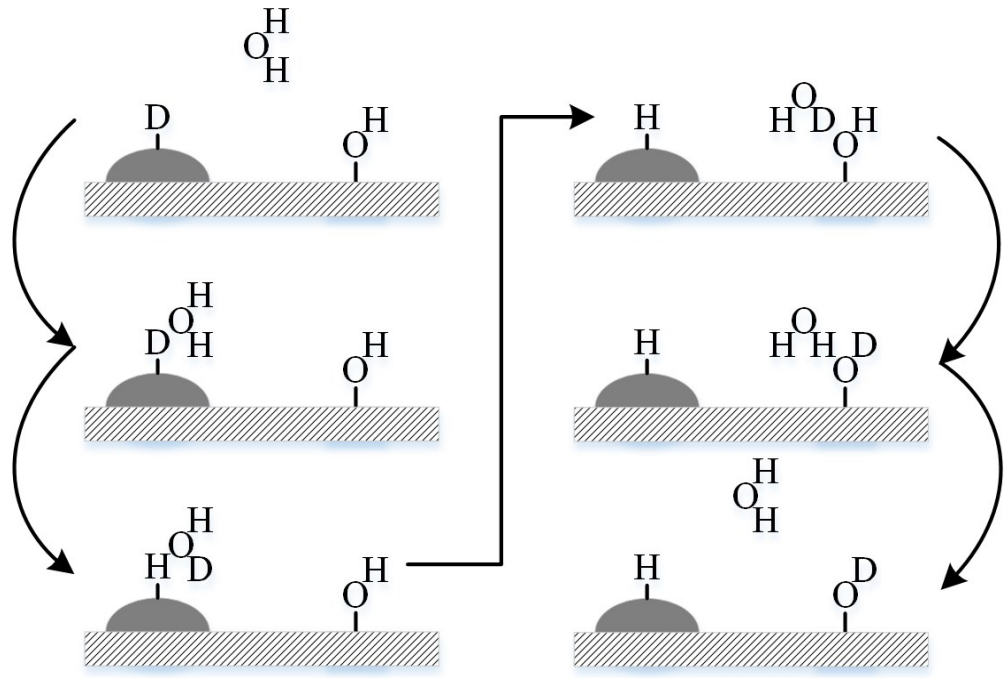

Figure 10: Details of the H-D exchange mechanism as proposed by Dalla Betta. See text for explanation.

Other claims of spillover can be just as easily explained with other effects. The simplest cases

are when spillover is reported in a system where the final spillover acceptor is in contact with the spillover initiator as well as an intermediate acceptor. In one example like this [57], researchers immersed an alumina supported Pd catalyst in a solution of phenyl t-butyl nitrone (PBN), a molecule that traps H atoms. The radical formed following this reduction is unequivocally detected using electron paramagnetic resonance. The radical is only observed when both H_2 and the catalyst are present, which the research took as evidence of spillover from the Pd to alumina and finally to the PBN. But in this case, the PBN in solution is in contact both with the Pd metal, which would undoubtedly be coated with H atoms following exposure to H_2 gas, as well as the surface of the alumina which was supposedly acting as an intermediate transport surface for the H atoms. This is an example of an observation being incorrectly attributed to spillover.

In some cases, claims of spillover in nonreducible supports, which cannot be otherwise explained, have been made. One material that is being actively studied is Pt supported on high surface area carbon compounds, such as activated carbon and carbon nanotubes. The formation of C-H bonds following exposure to H_2 gas have been confirmed in this material with several methods, including inelastic neutron scattering [7]. This is justified by the rehybridization of sp2 orbitals in carbon back to sp3 [8].

The main argument against spillover in nonreducible supports is a fairly simple one based on bond energies. Continuing to use the scenario of hydrogen spillover from a metal initiator, it is a fair (and supported) assumption that the energy of the metal-hydrogen (M-H) bond is greater than half the dissociation energy of molecular H, otherwise, H_2 would not dissociatively adsorb onto the metal. In order for the H atom to move to the support, a new bond must be formed of equal or greater strength, and it must be formed in the same process as that which breaks the M-H bond. If these conditions are not met, transport of the H atom is highly improbable.

The scenario of a nonreducible support would have an energy diagram similar to what is shown in Figure 11A. This illustrates how the atomically adsorbed state, where the atomic H is associated with the surface, is a much higher energy state than when it is associated with the metal. The high activation energy results because, according to valence bond theory, hydrogen does not want to form a chemical bond with atoms whose bonds are saturated, as is the case with the ions of nonreducible supports. Figure 11B shows a similar diagram for the H-D exchange described above. When a D atom simply exchanges with a H atom, with no net transport of either species, there is no difference in energy for the different states involved, making the process probable, though not favorable. This comparison further demonstrates how the latter explanation is much more likely.

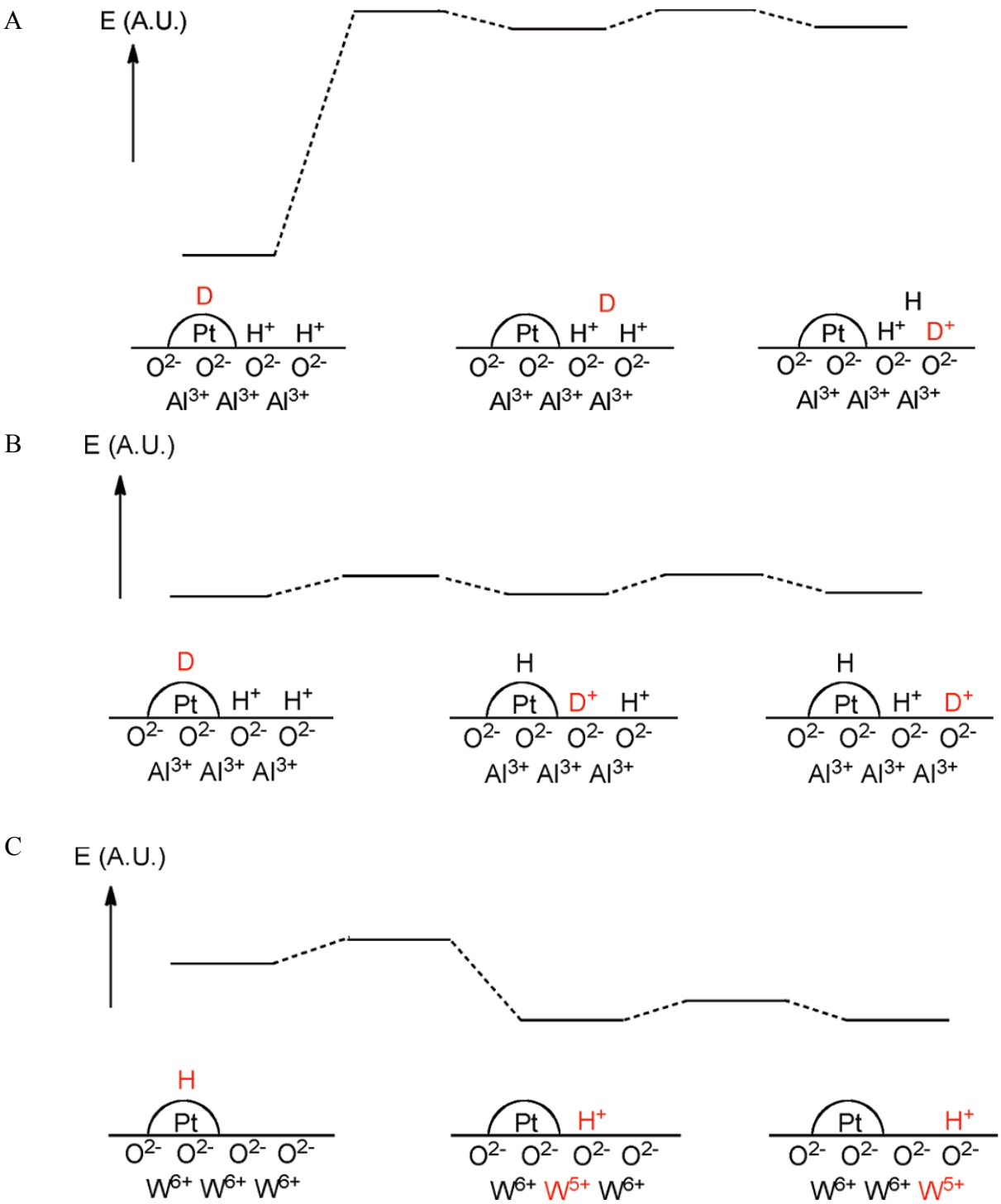

Figure 11: Illustrations and associated energy level diagrams for different atomic transfer mechanisms on surfaces. (A) Spillover of D atom from metal particle to non-reducible support, followed by H-D exchange on the support. (B) H-D exchange between metal and support, followed by the same on the support. (C) Hydrogen spillover onto a reducible support. Taken from reference [6].

The most energetically favorable scenario is shown in Figure 11C: spillover on a reducible support. Following dissociative adsorption onto the metal catalyst, atomic hydrogen will protonate an oxygen anion and donate an electron to the conduction band of the supporting metal. The most realistic form that the protonation will take is a hydrated proton, H_3O^+, following reaction with a water molecule. Support sites distant from the acceptor can be easily reached by diffusion of the H_3O^+ ion on the support surface in tandem with the conduction of the extra electron through the support. This mechanism [58, 59], is supported by the observation, mentioned above, that water acts as a spillover promoter in most cases, increasing the rate of reaction. Therefore, confirmation and further investigation of this proposed mechanism requires an understanding of water in the spillover system. NMR is an ideal tool to study water, being sensitive to the quantity, environment and dynamics of proton-containing molecules.

3.1. NMR in Spillover Research

Studies on spillover employ a multitude of methods, sometime several within the same article, including temperature programmed desorption, H-D exchange, infrared spectroscopy and NMR spectroscopy. NMR has a number advantages in the study of spillover. It is highly specific in its signal detection, capable of observing only a particular nuclei of interest, while also being able to differentiate between nuclei in different electronic or magnetic environments, either due to structure, molecular dynamics or chemical reactions. These are determined by differences in T_1, T_2 and chemical shift. The technique is especially attractive in the study of hydrogen spillover, since ^{1}H nuclei have the highest gyromagnetic ratios of NMR active nuclei, resulting in a high signal-to-noise ratio in a NMR experiment.

Indeed, a review of the literature finds many studies utilizing NMR to identify cases of spillover. Only a small sampling will be mentioned here. Multiple phases of adsorbed H on Ru and

Rh supported catalysts are frequently reported [9 – 12], usually two assigned to H bound to the metal, either reversibly or irreversibly, and a third to a highly mobile, weakly bound H species. One group [13] refers to this mobile species as a hydrogen "fog" because of how delocalized it is, maintaining however that it is still chemisorbed. Pd or Pt on silica or alumina is another well reported case of spillover, with a wide range of conditions required [14 – 16]. One case claimed that as much as 87% of the hydrogen taken up by a Pt-silica catalyst is present on the silica surface as spillover H. Again, Prins discounts a number of the above studies in his review, attributing some of the reported spillover to the reactivity of defects in the structure of the support, particularly when the identification of spillover involves detection of a hydrogenated hydrocarbon.

NMR as a technique for detecting and characterizing spillover has its drawbacks. For one, spillover is a surface effect, while NMR is a volume technique. This makes the method best suited for high surface area materials like porous silica. Also, all of these systems are solid. Even the spillover species, though possibly mobile, are bound to the surface. This will result in long correlation times and broad resonance lines. The NMR techniques used in existing studies have often been simple, single pulse experiments, occasionally using selective excitation or spin-labeling experiments. These experiments do not reduce the dipole-dipole interaction at all and will therefore yield broad NMR lines, on the order of 50-200 ppm. While the studies are able to accomplish and measure a great deal, they suffer from sensitivity and resolution limitations. For example, given the large linewidths there would be no simple way to clearly discern the surface water in multiple environments, separate from surface hydroxyl groups.

MAS NMR is well suited for the study of spillover. By reducing the effect of the dipole-dipole interaction, resonance lines are narrowed and details can be extracted from previously broad lines. Despite this, a paper by Chao et. al. [17] is the only report of a MAS NMR study of spillover that exists

in the literature. In this paper, because of the high resolution granted by the MAS technique narrowing the resonance lines, the group reports being able to individually detect seven individual spin groups: two types of surface water, two types of hydroxyl groups, spillover hydrogen, H bound by an oxygen vacancy (ie. Si-H bond) and H bound to Rh in various phases. The resonance lines of the first five of these species occur over the range of ~ 5 ppm, confirming the power of MAS NMR to increase resolution in this type of sample.

There are, however, a few questions and concerns surrounding this article, unfortunately detracting from its credibility. This article contains many references to other reported studies of hydrogen spillover using ^{1}H MAS NMR, however, the article by Chao is the only reported study to apply the MAS technique to the study of spillover species and spillover promoters. Many reports, not elaborated on here, use various NMR techniques, including MAS NMR, to characterize the support.

Points of contention of a more scientific basis exist in the paper by Chao as well. There are a number of pretreatments applied to the sample, including heating in a gas flow of O_2 or H_2 at 973 K. Spectra taken following this treatment show a number of species, depending on the type of gas used. Both treatments, however, show the presence of what is assigned as water strongly adsorbed to bridged hydroxyls. Not only is all water removed from silica surfaces at temperatures above 450 K [60, 61], but there should also be a decrease in the hydroxyl signal, as the threshold for hydrogen bonded hydroxyl dehydration from silica surfaces is reported to be in the range of 673 K [28, 62] to 773 K [61, 63]. It is possible that the water observed in the NMR results is a contaminant that has entered the experimental system after this heat treatment.

It is expected that improved peak assignment is possible through proper selection of catalyst support. Chao uses 60 – 80 mesh silica granules when synthesizing the catalyst, citing a surface area of 406 m^2/g. By using a highly ordered, well characterized porous silica, such as MCM-41, there

would be less uncertainty in peak assignments. Measured spectra could be more directly compared with results reported in the literature, since there is a wealth of knowledge on the behavior of water on such materials. If MCM-41 were used, there would also be more signal, due its larger specific surface area (> 1000 m^2/g).

Despite these minor details, the fact remains that ^1H NMR in this sample has had considerable success in general, and Chao's contribution demonstrates the increased resolution achieved in spillover conditions using ^1H MAS NMR. Based on the overall mixed success mentioned in the previous section, spillover research has always been marred by inconclusive and contradicting results. Even after almost 50 years of research and five international conferences dedicated to the topic, a number of fundamental questions pertaining to spillover still remain. There is a great need for the careful application of a novel technique to this field of research. ^1H MAS NMR has the potential to be this technique.

3.2. Spillover Applications

A full explanation of the spillover phenomenon remains mostly an open question, which is an enticing goal or motivation in and of itself. There are also, however, several applications that make researching this topic appealing to both the industrial and scientific communities. The first wave of spillover research was mainly motivated by the phenomenon's catalytic properties. The goal was to harness it as a novel hydrogenation technique in areas such as petroleum processing. Research attention shifted away from spillover due to conflicting results and lack of application development. More recently, interest has been piqued by new results and a new application in the field of hydrogen storage.

Environmental and supply concerns are necessitating a move away from fossil fuels as a source of energy in a variety of areas, particularly transportation. One possible avenue is to use hydrogen as a

fuel source, the energy being extracted locally by a non-combustion method in proton exchange membrane fuel cells, as these are much more efficient than conventional combustion methods. But to make this a viable alternative, a number of limitations must be overcome.

The first and foremost limitation of hydrogen fuel is storage. If hydrogen is to become a primary fuel source for transportation purposes, a storage technique must be found that matches or exceeds the energy density of fossil fuels. Conventional, high-density storage of hydrogen is achieved in the molecular gas state at high pressures, requiring incredibly strong tanks, the state of the art tanks being composed of carbon fiber. There are justified doubts as to the safety of this method in transportation applications. Physisorption methods also depend on high pressures, as well as low temperatures, making them impractical as well. Alternatively, chemisorption, in most cases, can proceed under ambient conditions, making it a desirable alternative.

The spillover mechanism, if understood, could be utilized to store hydrogen atoms on high surface area materials, easily hitting the United States' Department of Energy energy density criteria for a fossil fuel alternative [18]. This represents one of only a handful of technologies that has the potential to make hydrogen fueled transportation a viable alternative to the existing fossil fuel standard.

Based on several of the comments in the above sections, a thorough understanding of how water, a common spillover promoter, behaves on the surface of the support, particularly in the vicinity of a spillover initiator, is an important first step to a careful investigation of the spillover mechanism.

4. MCM-41

Silica (SiO_2) has been used for centuries in a wide range of applications in research and industry. A thorough, historical perspective on this can be found elsewhere [64], but a short, sample list of the areas utilizing silica includes catalysis, ceramics, textiles, food treatments and medicine. A number of its applications, such as catalysis and fundamental studies of adsorption mechanics [65], benefit from increased surface area, and so porous silica materials are an area of great interest.

In its report on porous solids [66], the International Union of Pure and Applied Chemistry (IUPAC) makes the distinction of the types of pores based on the pore width or pore diameter, d: micropores ($d < 2$ nm), mesopores (2 nm $< d <$ 50 nm) and macropores ($d > 50$ nm). The report goes on to outline four categories of porous solids based on how the pores are formed: 1) the crystal structure of the material is such that pores are naturally formed, as is the case in zeolites and some clays; 2) certain ceramics and inorganic gels are formed by the aggregation of small particles; 3) the natural processes leading to the porosity of animal and plant tissue (eg. cell division); and 4) the selective removal of parts of a material to create pores. A number of materials fall into the latter category, such as activated carbons and porous metal oxides (eg. SiO_2, TiO_2, ZnO_2, etc.). This method often results in materials with irregularly spaced, occasionally interconnected pores of varying diameter [20]. Example silica-based materials are SBA-15 [30] and controlled pore glass [31].

The first presentation of mesoporous silica materials with regular, well-defined pores was in 1992 when Beck et. al. presented what they called a "new family of materials" designated M41S [19, 20]. While a number of members of this group of materials have been reported on, MCM-41 has received the most attention, with a wealth of research on its fundamental nature and interaction with various compounds and environments existing in the literature (references [20, 21, 27 – 30, 40, 67 – 71] to name a few). These works have lead to proposed and realized applications in such diverse areas

as catalysis reactions [22 – 26], fundamental research of water-surface interactions [21, 27 – 35], non-freezable (ie. super cooled) water [36] and drug delivery [37].

MCM-41, as well as all members of the M41S family for that matter, are formed by self-assembly in solution via a liquid crystal templating mechanism. Covered in more detail in references [19, 20], the schematic of the mechanism, presented by Kresge, is shown in Figure 12. Basically, cationic surfactant molecules form cylindrical micelles which arrange themselves into hexagonal arrays. Silica then fills the space between and around the micellar template. A calcination step removes any remaining template, leaving uniform channels of amorphous silica. The diameter of the pores can be controlled by varying the length of the surfactant molecules used as a template. Pore diameters from 1.5 to 50 nm have been characterized [20].

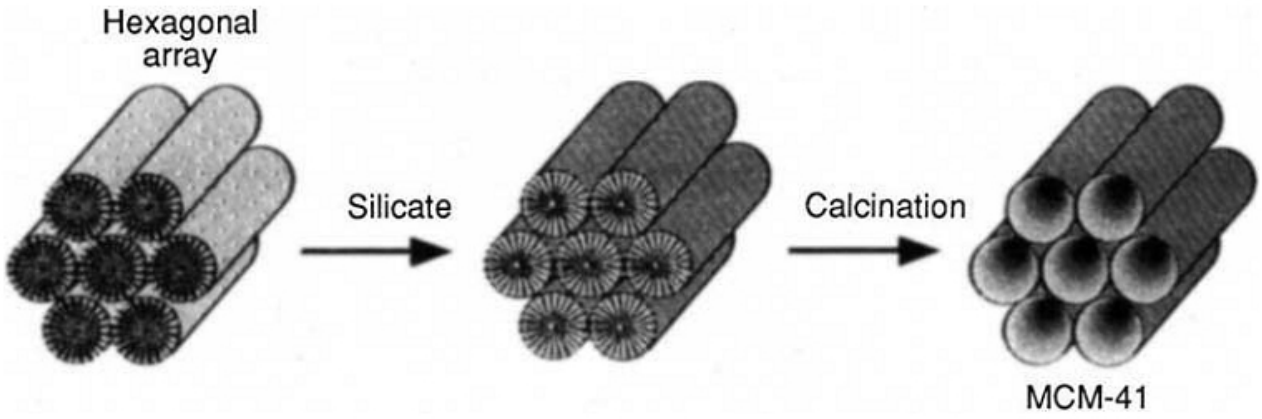

Figure 12: Schematic of the liquid crystal templating mechanism used in the synthesis of MCM-41. Taken from reference [20].

4.1. Structural Characterization

There are a number of techniques to characterize porous solids, as outlined in the IUPAC report on porous solids [66]. The applicability and usefulness of these techniques depend on the specifics of the material. For a mesoporous material in a powder state, such as MCM-41, characterization is most

commonly carried out by x-ray diffraction (XRD) and gas adsorption. Electron microscopy is also useful, though not essential.

4.1.1. X-Ray Diffraction

X-ray diffractometry has been used in crystallographic studies since the advent of the technique. It is one of the primary research methods for determining the structure of solids, particularly in polycrystalline materials. This method is a field unto itself, and its finer points are covered in great detail in reference [72]. A brief summary is provided here, as it pertains to the characterization of MCM-41.

In a powdered, polycrystalline sample, that is, a sample made up of small, crystalline grains, the orientation of the individual crystallites is assumed to be randomly distributed. This means that when a monochromatic x-ray source of wavelength λ is directed at the material, all the diffracted beams are present simultaneously. By sweeping the angle of a detector relative to the incident beam, pivoting about the sample, a number of diffracted beams can be measured, as shown in Figure 13A. These beams are detected at angles defined by Bragg's law,

$$n\lambda = 2d\sin\theta \tag{56}$$

where n is the order of the diffraction, λ is the wavelength of the source, d is the spacing between reflecting planes and θ is the angle of incidence and reflection (therefore, 2θ is the angle between the incident and diffracted beams). Equation (56) is simply derived from the condition of constructive interference between incident and reflected beams, which occurs when the additional distance traveled by one of the two interfering, reflected x-rays is equal to an integer number, n, of wavelengths. This point is illustrated in Figure 13B.

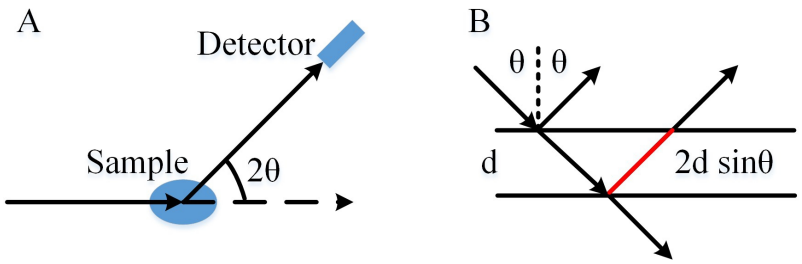

Figure 13: X-ray diffraction. (A) Experimental setup. (B) Theory. Red line indicates the extra distance traveled by the second reflecting x-ray.

In most cases, the periodic, reflecting surface is an atomic-level crystal plane. In the case of MCM-41, the periodic features are the pores themselves [68], which are arranged in a hexagonal close packing (HCP) arrangement, as shown in Figure 12. This can be determined from the diffractogram generated by an MCM-41 sample, an example of which is shown in Figure 14. The lattice type, and thus the Miller indices of the crystal planes the x-rays are reflecting from to cause each peak in the diffractogram, is determined by analyzing a data set such as this. First, the interplanar distance, *d*, for each peak is computed, using the value of 2θ it is centered on and equation (56). The ratio of *d* for each peak relative to that of the first is unique to each type of crystal lattice type. By calculating the ratios of *d* spacings for a given diffractogram and comparing them to the calculated ratios for each lattice type, the structure of the given material is determined.

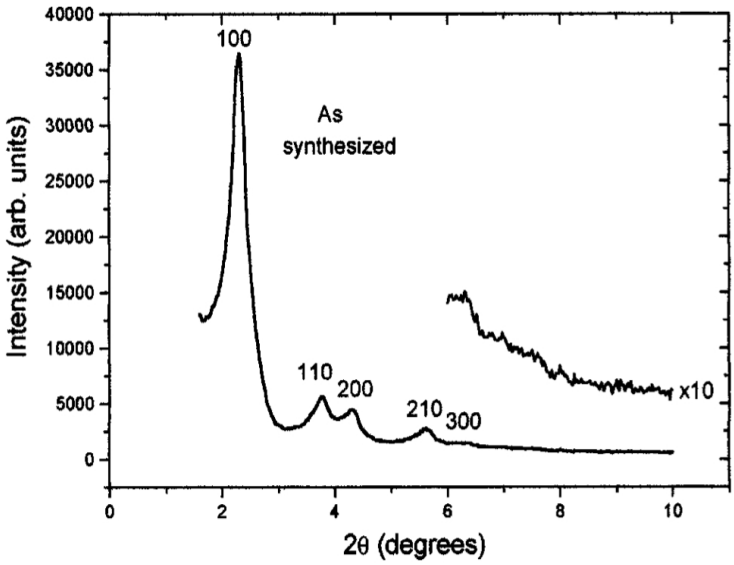

Figure 14: Representative XRD pattern for well-formed MCM-41. The peaks have been labeled with the Miller indices of the reflecting crystal plane. Taken from reference [73].

The spacing of the first peak in the diffractogram, which corresponds to the (100) plane, d_{100}, can be used to determine the pore diameter, d_{pore}. The lattice parameter, a, can be calculated from this spacing by

$$a = \frac{2}{\sqrt{3}} d_{100} \tag{57}$$

This represents the centre-to-centre distance between two pores, and so includes two pore radii (ie. one d_{pore}) and one pore wall thickness, d_{wall} [19]. d_{pore} can be calculated from [74],

$$d_{pore} = c d_{100} \sqrt{\frac{\rho V_p}{1+\rho V_p}} \tag{58}$$

where c is a shape factor related to the pore's cross-section, ρ is the pore wall density and V_p is the primary mesopore volume. d_{wall} is calculated by subtracting d_{pore} from a.

4.1.2. Gas Adsorption

A wealth of information about a porous material can be obtained from a gas adsorption

isotherm, a measurement of the volume, V, of gas (the adsorbate) adsorbed onto a material (the adsorbent) as a function of partial pressure (p/p_0), including surface area and pore size distribution. p_0 is the saturation pressure of the adsorbate gas. The IUPAC report on porous solids suggests that nitrogen, at its boiling point (77 K), is the best gas for determining surface area and mesopore size distribution [66]. The report suggests other gases and techniques for macropore and micropore size distributions.

Most experimental isotherms fall into one of six types, three of which are shown in Figure 15 [75]. These are differentiated by the characteristics of the curve, such as hysteresis, curvature and number of inflection points. The type of isotherm suggests a broad classification of the adsorbent. For example, broadly speaking, non-porous, microporous and mesoporous solids are indicated by isotherms of Type II, I and IV, respectively.

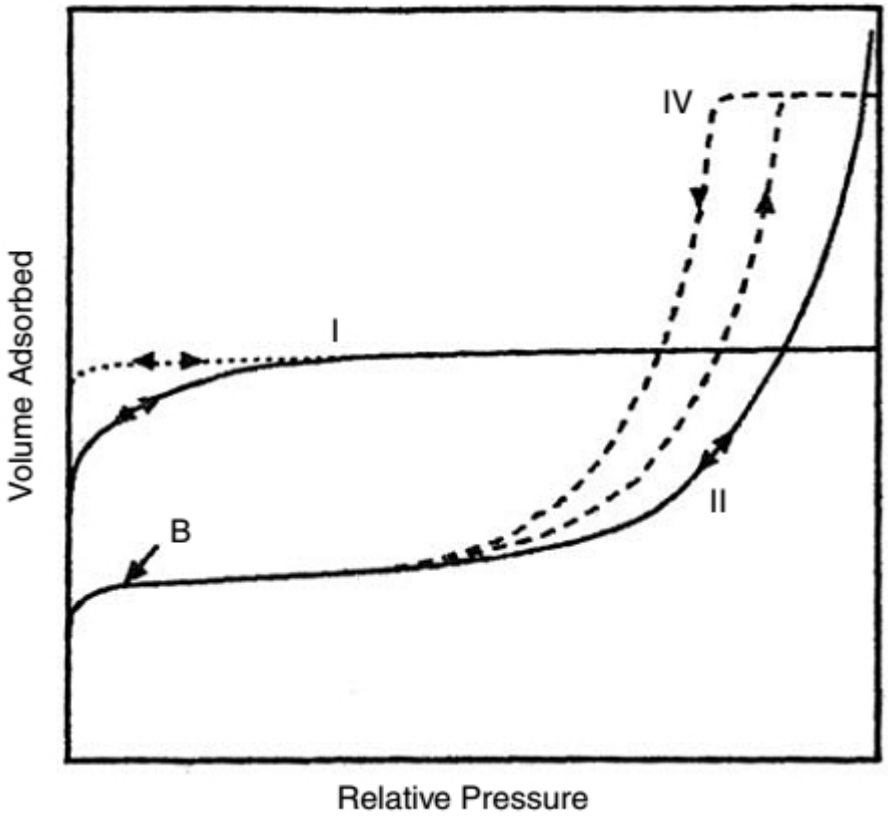

Figure 15: Three types of adsorption isotherms. Taken from reference [76].

A Type IV isotherm, such as is found for MCM-41, can be divided into three main regions. Starting from a relative pressure of zero, there is an initial sharp uptake of gas. Following this, the first main region is linear and is attributed to the formation of a monolayer of adsorbed gas. The sharp increase, which shows a hysteresis behavior, is caused by capillary condensation (a filling of the pore volume by multilayer adsorption from the vapor phase) of gas in the pores. The final region shows saturation of the material with gas.

The surface area of a porous sample can be determined from an adsorption isotherm by means of the Brunauer-Emmett-Teller (BET) theory [75, 77]. The surface area, A, contained in a porous sample can be stated as,

$$A = n_m a_m N_A \tag{59}$$

where n_m is the number of moles of adsorbate per gram of adsorbent in a monolayer, a_m is the average area occupied by a molecule of adsorbate in a completed monolayer and N_A is Avogadro's constant. Both a_m and N_A are known constants. n_m is determined from the isotherm by applying the BET equation in the form,

$$\frac{p/p_0}{n(1-p/p_0)} = \frac{1}{n_m c} + \frac{c-1}{n_m c}(p/p_0) \tag{60}$$

where c is a parameter defined by the net heat of adsorption. Fitting the initial, linear portion of the isotherm to this equation, both c and n_m can be calculated, allowing determination of the surface area.

A Type IV isotherm can also be used to determine the pore size distribution using the Kelvin equation [75]. This distribution amounts to a plot of dV/dR_p versus R_p, where R_p is the pore radius. The equation describing this plot is

$$\frac{dV}{dR_p} = 2.356 \frac{dV}{d\left(\frac{p}{p_0}\right)} \left[\ln^2\left(\frac{p}{p_0}\right) \right] \frac{p}{p_0} \tag{61}$$

The differential factor is determined by numerically differentiating the adsorption isotherm (V versus p/p_0) with respect to (p/p_0).

4.1.3. Electron Microscopy

In principle, some of the information obtained by the above methods could also be determined using scanning electron microscopy (SEM) and transmission electron microscopy (TEM). It is possible to image the sample using a resolution sufficient to observe the pore structure of MCM-41. An example of this is given in Figure 16. This could allow the estimation of the pore diameter and wall thickness, as well as irrefutable confirmation of the hexagonal pore arrangement.

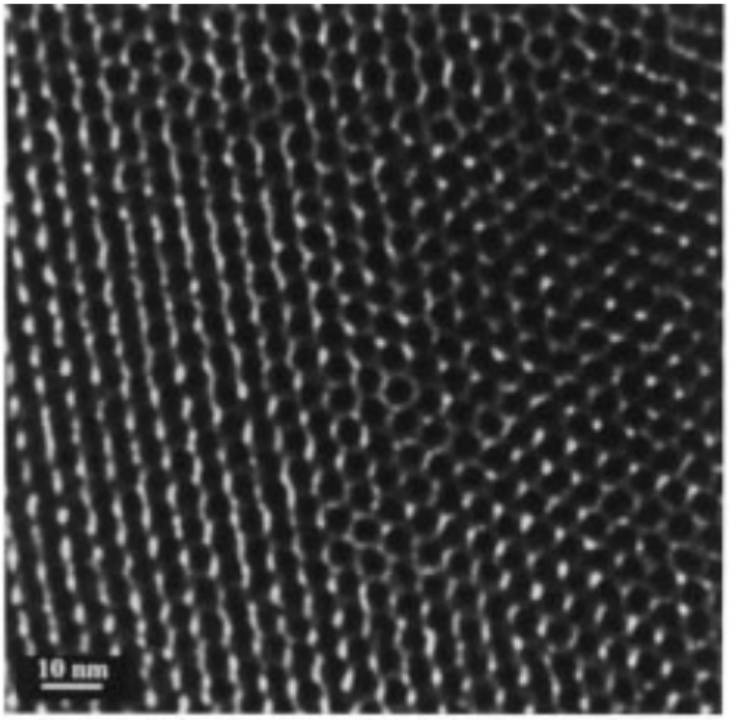

Figure 16: Example of a TEM image of MCM-41. Scale is inset. Taken from reference [74].

4.2. MCM-41 Pore Surface

A mesoporous, polycrystalline material such as MCM-41 has characteristics at several length scales. The previous section dealt with those at the roughly nanometer to micrometer scale, the size and arrangement of the pores. The current section will delve a little deeper, discussing the roughly angstrom scale that exists at the pore's surface, involving the structure and chemistry of the molecular groups that populate it.

4.2.1. Silica Chemistry in MCM-41

The term silica is used to encompass all of its forms: crystalline, amorphous, natural and synthetic. Regardless of the details, the basic structure is the same: a Si atom bonded tetrahedrally to four O atoms. At the surface of silica particles, there is the possibility that one or more of these O atoms will be bonded to a H atom rather than another Si atom. Such a Si–OH group is called a silanol group [78].

There are four possible types of silanol groups in silica, labeled Q^{4-n}, where *n* is this number of hydroxyl groups bonded to the silicon atom [78]. There are, however, only three of these present in MCM-41, as indicated by ^{29}Si-CPMAS NMR experiments [28, 67, 78]; there have been no reports of Q^1 groups being observed in MCM-41. In fact, the physical existence of the Q^1 group in silica materials is not generally accepted [78]. The Q^4 groups, which comprise about 15-25% of MCM-41, are necessarily found only in the pore walls, away from the surface. The majority, 50-70%, of the silicon atoms in MCM-41 are Q^3 groups; only small amounts of Q^2 are present, normally < 10%. Figure 17 shows an illustration of these various types of groups.

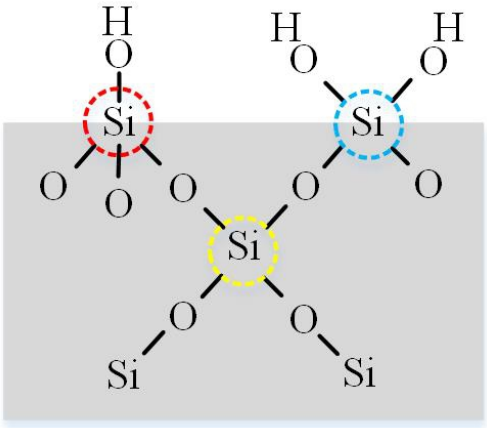

Figure 17: Types of Q^n groups found in silica. The different types highlighted with dashed circles are: Q^2 (blue), Q^3 (red) and Q^4 (yellow). The gray box designates the silica volume.

Though not distinguishable in ^{29}Si-CPMAS NMR, ^{1}H NMR and IR spectroscopy show that the Q^3 groups can be found in a variety of arrangements. These are best illustrated through a discussion of how these groups form on the pore surface of MCM-41.

The final step in the synthesis of MCM-41 is a calcination procedure to remove the surfactant template. This leaves the pore surface almost perfectly devoid of silanol groups. Adjacent Si atoms that are exposed at the silica surface are joined by a bridging O atom. These ≡Si–O–Si≡ structures are referred to as siloxane bridges [78] (the ≡ signifies the three remaining bonds of Si to other O atoms).

If a sufficiently energetic water molecule reacts with a siloxane bridge, it will dissociatively adsorb, or chemisorb. This opens the siloxane bridge, leaving two silanol groups. This hydroxylation process is illustrated in Figure 18. These single silanol (SOH) groups continue to form as more water reacts with the surface. At a sufficiently high hydroxylation level, a second type of Q^3 silanol begins to form where the geometry allows for it. When the H of one silanol is sufficiently close the O of a neighboring silanol, hydrogen bonding will occur, leading to a hydrogen bonded silanol (HBOH) group [69, 78].

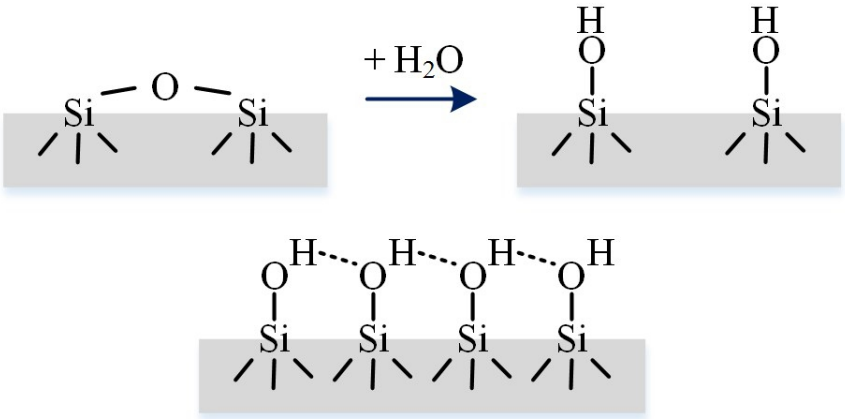

Figure 18: Progression of hydroxylation on MCM-41. (Top) The dissociative adsorption of water on a siloxane bridge leading to two SOH groups. (Bottom) HBOH groups, where the hydrogen bond is shown as a dashed line. The gray box designates the silica volume.

This hydroxylation process can be reversed with the addition of thermal energy. Heating MCM-41 to 673 K removes the HBOH groups from the pore surface, but leaves the SOH groups [28, 62]. If the sample temperature is raised above this level, then the SOH groups are removed as well [62]. At 1123 K, the pores collapse, resulting in what is essentially bulk silica [70].

The structure of the pore wall and surface of MCM-41 is generally thought to be amorphous [69]. A particularly successful approach to modeling the amorphous silica surface has been to use specific faces of the β-crystobalite crystal structure (see reference [79] and references therein). Mixing these faces in appropriate proportions can reproduce certain observations such as surface silanol

density and Q^n populations. But these methods fall short in MCM-41, being unable to reproduce the lower silanol density seen there as compared to truly amorphous silica surfaces, leaving the topic as an arena of active research [67]. One method to access more information about the surface is to study the behavior of water on these silica surfaces.

4.3. MCM-41 and Water

Central to nearly every application for MCM-41 mentioned above is that they occur in an aqueous environment. A silica surface interacts strongly with water, since it is covered in hydrophillic silanol groups. This makes knowledge of how water behaves in MCM-41 crucial to a thorough understanding of any aqueous application. This is especially true for applications like catalysis and spillover research, where water can play a pivotal role in a system's mechanics.

NMR naturally lends itself to the study of a proton-rich system like water in porous silica. The work of several researchers (references [21, 27 – 35] to cite but a few) have been able to identify many of the system's features over a range of hydration levels (the amount of water in the system). A selection of these include the identification of different water environments, the chemical shift of those species and various theories on how they may be interacting with each other and the silica surface. Each publication leads to another conclusion about MCM-41 and its interaction with water. A recent model published by Walia et. al. [21] aims at drawing together many of the ideas existing in the literature to generate a detailed model for small amounts of water on MCM-41 in order to explain the results of their ^{1}H MAS NMR experiments.

4.3.1. Walia Model for the behavior of Water in MCM-41

The Walia model builds on the work of Trebosc [29] and Grunberg [30], as well as several others (see reference [21] and references therein). There are two main points that set this particular model apart from the work that comes before it. The first is the level of detail, both in the acquisition

of data and the fitting process. Measurements were taken of a commercially synthesized MCM-41 sample as a function of temperature (200 – 325 K) and of hydration (0 – 7.8 % water by weight). This large data set was then fit to greater detail than had previously been attempted. Based on physical arguments identifying the different proton environments present in MCM-41, the spectra were fit with five peaks. A more conventional approach to analyzing MAS NMR spectra of MCM-41 is to fit only the main peaks (one or two), citing magnetization exchange as the cause for the various proton species appearing in small number of peaks.

The five peaks identified in the Walia model are SOH groups, HBOH groups, hydrated SOH groups (ie. a single silanol group that has a water molecule hydrogen bonded to it), water that is hydrogen bonded to SOH groups (SOH water) and water that is hydrogen bonded to HBOH groups (HBOH water). The presence of a peak for the hydrated SOH groups, meaning it is distinguishable from both the unhydrated SOH groups and the SOH water that are hydrating those groups, highlights the second unique feature of the Walia model: its lack of magnetization exchange.

Contrary to most other discussions of MAS NMR spectra of MCM-41, which leverage exchange in some aspect of their explanation, no such exchange is needed in the Walia model. This is necessary to explain the results of publications finding limited exchange at low hydration levels [27 – 29]. The chemical shift and area of each peak are explained by shifting occupation probabilities (or equivalently, populations) of different hydrogen bonding configurations. These are the result of large numbers of water molecules in constant motion on the surface of MCM-41, causing an average distribution across the configurations that changes based on the details of the system, such as temperature and hydration.

The full set of hydrogen bonding configurations used by Walia are presented in Figure 19. Each configuration, labeled *a* through *g*, involves two or more of the five different proton species

mentioned above. Configurations *a* through *e* show the different ways that hydrated SOH groups and SOH water can hydrogen bond, while configurations *f* and *g* show the same for HBOH groups and HBOH water.

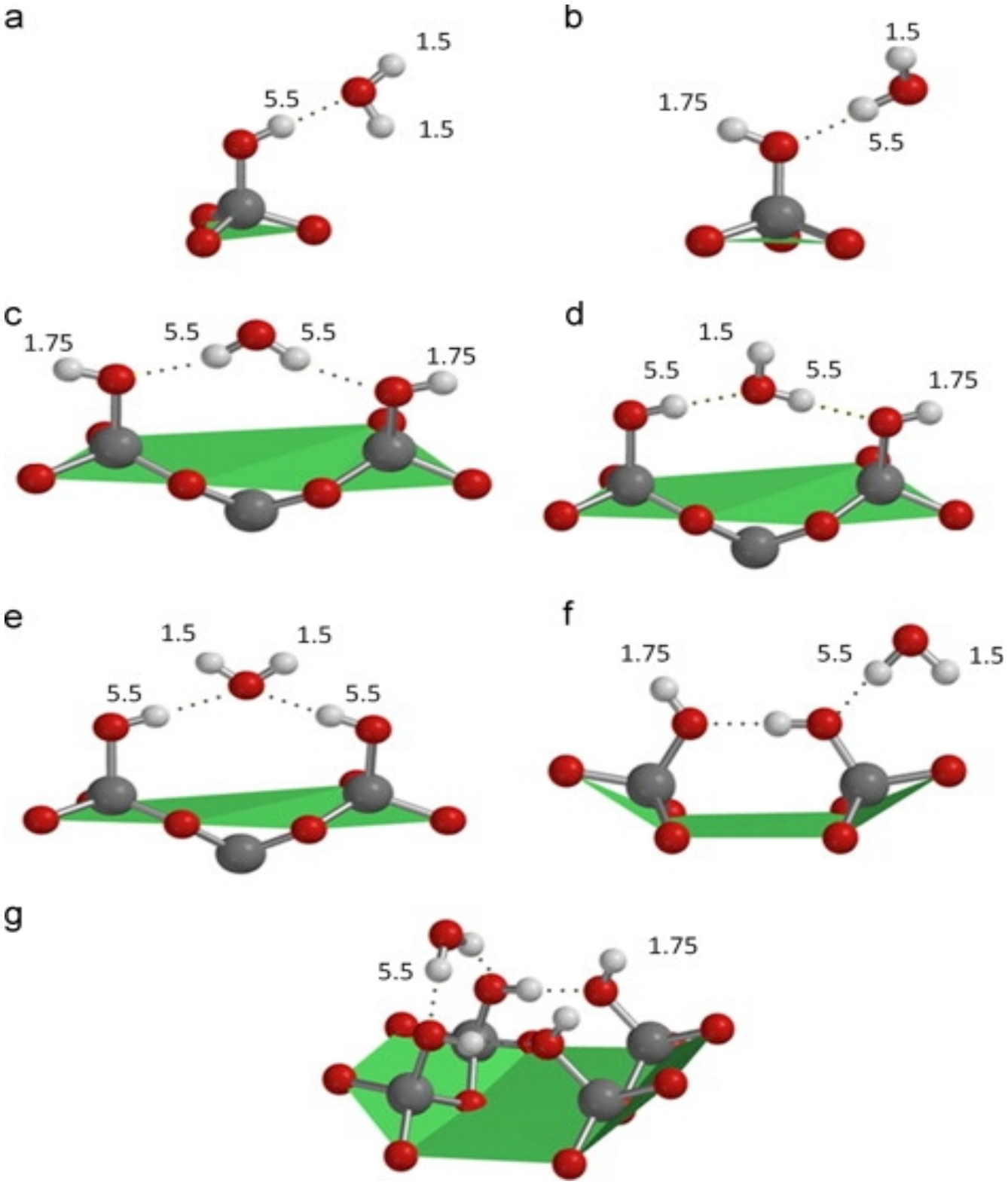

Figure 19: Hydrogen bonding configurations of water with the MCM-41 surface, as presented in the definition of the Walia model. Taken from reference [21].

The chemical shift of an individual proton in the Walia model is straightforward: the H on an unhydrated SOH group has a shift of 1.75 ppm; the shift of a H on a water molecule that is not hydrogen bonded to anything has a shift of 1.5 ppm; and a H that is involved in a hydrogen bond has a shift of 5.5 ppm. These three states of H atoms can be used to determine how each hydrogen bonding configurations in Figure 19 contributes to the overall shift for the groups involved. For example, the SOH water molecule in configuration *b* is involved in one hydrogen bond, so its two H atoms have shifts of 1.5 and 5.5 ppm. The contribution of water molecules to the chemical shift of their associated NMR peak is the average shift between its two H atoms [21], so the water in configuration *b* will contribute 3.5 ppm. Similarly, the water in configuration *g* will contribute 5.5 ppm, since it is involved in two hydrogen bonds, to the shift of the HBOH water peak. The summary of how each configuration contributes to the chemical shift of the species involved are found in the following equations, originally presented by Walia,

$$\delta_{SOH\ Water} = p_a(1.5) + p_b(3.5) + p_c(5.5) + p_d(3.5) + p_e(1.5) \tag{62}$$

$$\delta_{HBOH\ Water} = p_f(3.5) + p_g(5.5) \tag{63}$$

$$\delta_{Hydrated\ SOH} = p_a(5.5) + p_b(1.75) + p_c(1.75+1.75) + p_d(5.5+1.75) + p_e(5.5+5.5) \tag{64}$$

where p_i is the relative population of each configuration occurring in the sample. The number in brackets represents the chemical shift in ppm of the species each equation concerns, in each particular configuration.

The area of each peak in the NMR spectrum is explained using the different configurations in Figure 19, as well as other physical arguments. This model, with some modification, will form the basis for the analysis of results in the current study. Therefore, further aspects of the model are discussed in more detail, as needed, in the Discussion section.

4.4. Hydrogen Spillover on MCM-41

As is outlined in chapter 3, several sound arguments exists that should theoretically prevent hydrogen spillover from occurring on MCM-41. Despite this, numerous reports exist in the literature citing this phenomenon as the cause for a variety of observations [22 – 25, 80, 81]. The model put forward by Kanda et. al. [25] is shown in Figure 20, illustrating the transfer of atomic H over the MCM-41 surface, which according to Prins is highly unlikely. Still, some results are difficult to dispute. Wojcieszak et. al. [81] performed temperature programmed desorption measurements on their system, which they claim exhibits spillover behavior. The high temperatures required to desorb some of the hydrogen species are difficult to explain without the spillover phenomenon. Clearly more work is required on these systems in order to understand them well enough to be able to conclusively prove or disprove the possibility of spillover.

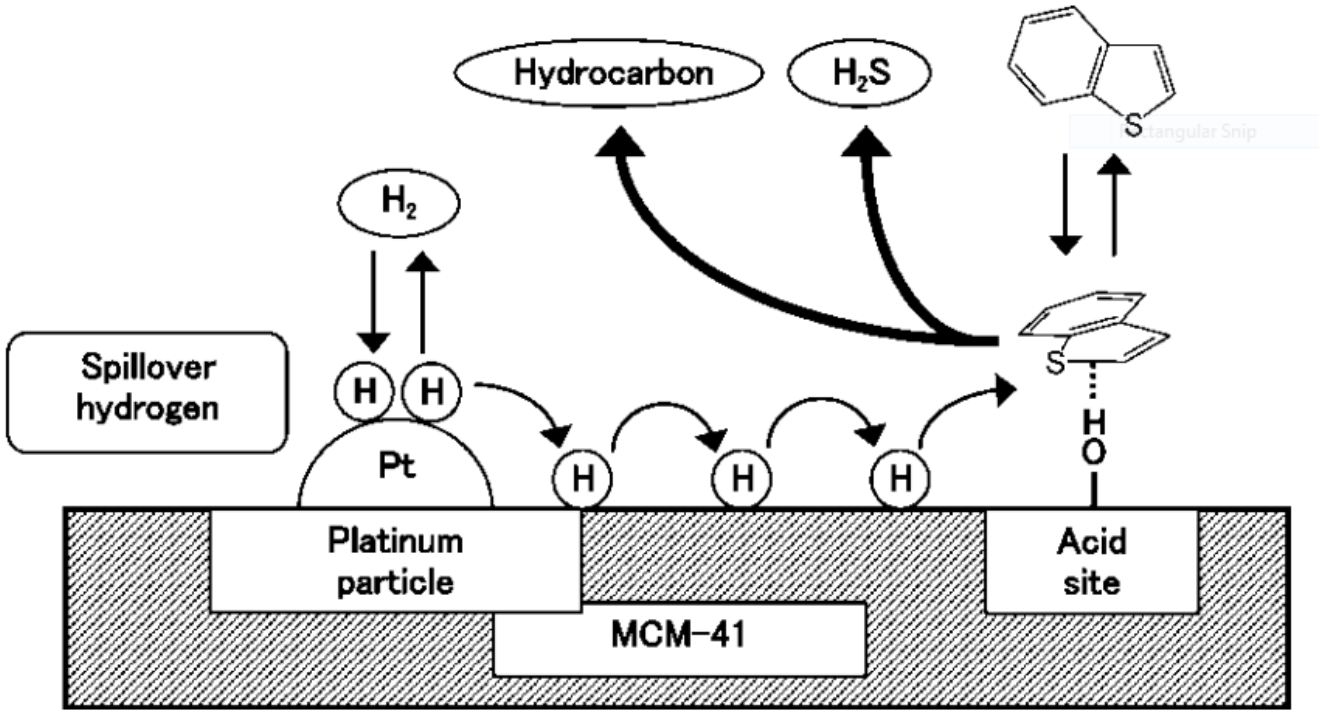

Figure 20: Model for hydrodesulfurization of benzothiophene over Pd-MCM-41 as presented by Kanda et. al. [25]. Pictured is the transfer of atomic hydrogen (ie. spillover) across the surface of MCM-41. Taken from reference [25].

4.5. Palladium in MCM-41

Palladium is a transition metal that has found eager adoption in a variety of uses in industry as well as electrical, dental and aesthetic applications [82]. It is exceptionally active as a catalyst, and has many secondary features that make it even more desirable in this role, such as: high selectivity in certain reactions, resiliency to many chemical agents, high catalytic activity under ambient conditions and easy recovery once spent [82]. Of particular note is its ability to allow H to diffuse through its lattice, finding application in the isolation of ultra pure H gas. The highly attractive catalytic features of Pd make its incorporation into a high surface area support like MCM-41 a natural progression, since this would allow the stable dispersion of a large number of small Pd particles over a large surface area in a small volume.

Pd can be added to MCM-41 in a variety of ways during or after the synthesis of the MCM-41 support. A Pd source can be added to the mixture of surfactant template and free silica, either as a slightly acidic salt solution (eg. $Pd[NH_3]_4Cl_2$or $PdCl_2$) [41, 42] or as preformed, ligand stabilized nanoparticles [26, 41]. Addition of the Pd after synthesis of the support is usually achieved by impregnating the MCM-41 with a solution, usually by the incipient wetness technique, but fully aqueous methods exist as well [24]. This solution can again be a slightly acidic, Pd salt solution [22, 23, 41, 43, 83] or a suspension of preformed nanoparticles, normally stabilized by ligands [41, 44]. Occasionally, this impregnation can be assisted by performing an ion exchange pretreatment [43], aimed at assisting reduction of the metal out of solution, depositing it on the pore surface. In all of the above cases, the desirable features of the support, namely its high surface area and mesoporous structure, are left intact or minimally affected.

Pd-MCM-41 materials have been used to great success in a number of catalytically assisted reactions. A small sample of these include fine chemical and pharmaceutical manufacture [22, 23],

oxidation of methane [24], petroleum processing [25] and liquid phase hydrogenation [26]. Its capacity for hydrogen storage has also been demonstrated [40]. As mentioned in the previous section, Pd-MCM-41 is implicated in a number of hydrogen spillover reactions [22 – 24].

Most of these systems involve water to some capacity. If gaseous H is involved, and any amount O is present during H exposure, then water will be formed [84 – 86] which will affect the behavior and performance of the system. Therefore, gaining an understanding of the behavior of water in this material is a step towards understanding the entirety of each of the aforementioned systems; water is a universal factor in the applications of Pd-MCM-41.

5. Materials and Methods

5.1. Sample Synthesis

There are three types of MCM-41 samples studied for the majority of this work: i) conventional, unmodified MCM-41, referred to as “pristine MCM-41”; ii) palladized or palladium-loaded MCM-41, referred to as “Pd-MCM-41”; and, iii) Pd-MCM-41 with some of it's palladium oxide groups reduced to palladium metal, referred to as “reduced Pd-MCM-41” or “Red-Pd-MCM-41”. An initial step of the synthesis process of Pd-MCM-41 is ammonium ion exchange of pristine MCM-41. A sample representing this intermediate step is obtained and briefly studied to understand the effects of this treatment. This sample is designated “NH_4-MCM-41”. Another sample studied briefly is Pd-MCM-41 that has been more thoroughly treated than the above Red-Pd-MCM-41 so that no oxides remain. This sample is identified as “oxide-cleaned Pd-MCM-41”. The details of the synthesis of each of these samples is covered in the following sections.

5.1.1. Pristine MCM-41

The unmodified MCM-41 material (as well as the Pd-MCM-41 covered in the next section) used in this report was synthesized by Dr. Colin Guthrie during his time as a PhD candidate at the University of Waterloo, supervised by Dr. Eric Reardon. His procedure, detailed in his thesis [87], is based on what is available in the literature [73, 88], which will be summarized here.

A solution of tetramethylammonium hydroxide (TMAOH) and cetyltrimethylammonium bromide (CTABr) is prepared at 303 K under light stirring using ultrapure water. Once these are properly dissolved, the silica source, fumed silica, is added. Stirring and heating are continued for 3 h, after which the mixture is in a gel state. At this point the vessel is covered and allowed to cure for 24 h at room temperature. The relative molar composition of the solution at this point is 1 SiO_2, 0.19

TMAOH, 0.27 CTABr, 40 H_2O. The size of the batches are based on 250 g of H_2O, which is chosen based on hardware capacity limitations.

After curing, the mixture is heated at 400 K for 68 h in a stainless steel autoclave, sealed with a Viton-Teflon o-ring. At the end of the heat treatment, the autoclave is cooled in running water. The resulting material is white in appearance and paste-like in texture. This material is washed 12 times, or until the supernatant rinsate has a conductance less than 10 μS/cm, by adding ultrapure water, mixing, centrifuging and decanting the supernatant. The final step is calcination at 923 K for 8 h to remove the last of the template molecules. The resulting powder is dehydroxylated MCM-41.

5.1.2. Pd-MCM-41 and NH_4-MCM-41

As mentioned above, the Pd-MCM-41 used in this report was synthesized by Dr. Colin Guthrie. His procedure, detailed in his thesis [87], is based on that of Koh [43], which will be summarized here.

The chosen method depositing Pd on MCM-41 begins with an ion exchange step. This will facilitate the reduction and adhesion of Pd onto the surface of the MCM-41. Calcined MCM-41, prepared as above, is added to 100 mL of 2 M NH_4Cl solution. This mixture is stirred for 15 minutes and then washed 12 times with the rinse, centrifuge, decant method described above. After a final centrifuging, the recovered solid is dried at 353 K overnight. A sample of this NH_4-MCM-41 is set aside for later testing.

The Pd source, $Pd(NH_3)_4Cl_2 \cdot H_2O$, is dissolved in deionized water. This solution is added dropwise to the NH_4-MCM-41 following the incipient wetness technique, whereby the solution is essentially drawn into the pores via capillary action and aided by the hydrophillic SiOH groups on the surface of the MCM-41. This material is then dried at 353 K overnight and then calcined at 593 K for 3 h, both under ambient laboratory atmosphere. Based on the amount of Pd metal source dissolved in solution and subsequently added to the sample, the resulting metal content is 2 % Pd by mass (ie. 2 g

out of every 100 g of Pd-MCM-41 is due to Pd metal).

5.1.3. Reduced Pd-MCM-41

The reduced Pd-MCM-41 sample is prepared from the same batch of Pd-MCM-41 detailed in the previous section. About 100 mg of Pd-MCM-41 is measured into a gas tight NMR tube acquired from the Wilmad-LabGlass company. This vessel is attached to a vacuum system and evacuated under vacuum ($< 10^{-6}$ bar) for 24 h in order to remove any water adsorbed on its surface, leaving the Pd clusters as bare as possible. The sample is then exposed to 1.7 bar of pure H_2 gas, with care being taken to ensure that all intermediate volumes involved are either evacuated and sealed, or flushed with flowing H_2 to ensure no O_2 contamination. Any O_2 that enters the system during this reduction procedure would react with H_2 to form H_2O, which would not result in any loss of O from the Pd cluster surface, thus limiting the effectiveness of the procedure. The tube is then sealed using its incorporated Teflon valve and left to soak for 24 h. The sample is reattached to the vacuum system, pumped on for another 24 h and the process is repeated once.

5.1.4. Oxide-Free Pd-MCM-41

A more thoroughly oxide cleaned sample is prepared by Dr. Guthrie in his lab. His process is identical to that used above for the reduced Pd-MCM-41, but employs a more robust apparatus. A stainless steel reaction chamber is used with high-pressure fittings and valves. This reaction chamber has a volume around 6 mL, which is 100-200 times smaller than the glass vacuum system used above.

5.2. MCM-41 Characterization

5.2.1. Gas Adsorption

Gas adsorption measurements are performed on a Micromeritics Gemini VII Surface Area Analyzer, located in the Chemical Engineering Analytical Services Laboratory at the University of

Waterloo. The measurement process begins with a pretreatment of heating about 160 mg of the sample at 573 K under a nitrogen atmosphere overnight (17 hours). After measuring the saturation pressure of the adsorbate gas (N_2), an adsorption isotherm is recorded by recording the volume of gas adsorbed at various relative pressures (compared to the saturation pressure). Two types of BET experiments are performed: i) a 25 point full isotherm ($0.05 < p/p_0 < 0.95$), used to characterize pore quality and obtain pore size distributions; and, ii) a 15 point selective isotherm ($0.05 < p/p_0 < 0.30$), used to accurately measure the BET surface area, which only depends on the initial linear region of the isotherm. These isotherms were then analyzed using equations (60) and (61) to obtain the surface area and pore size distribution. Selective isotherms are recorded for all three sample types in order to determine their surface area, while full isotherms are only measured for the pristine MCM-41 and Pd-MCM-41 samples, as the reduction process is assumed to not cause any significant structural changes.

5.2.2. XRD

The XRD measurements are made with a Bruker AXS D8 Advance X-ray diffractometer with a Cu Kα (1.5418 Å) x-ray source. The measurements were performed by Dr. Linda Nazar's group in the Department of Chemistry at the University of Waterloo. Each scan uses 50 mg of powdered sample and the detector position is swept from 0.7 to 8.0 degrees 2θ in 0.017 degree step sizes.

5.3. NMR Measurements

All NMR measurements are performed in a 11.7 Tesla superconducting magnet using a Bruker DMX500 spectrometer. The spectrometer is controlled from a Unix workstation running Bruker's XWIN-NMR software. A Bruker MAS probe is used for all measurements. The samples are packed into a zirconia MAS rotor with a 4 mm outer diameter. The rotor is acquired from the Wilmad-LabGlass company. It is sealed with a rubber o-ring-containing cap to prevent any loss or addition of water vapor or other contaminants during handling and measurement. The rotor driving gas is dry,

filtered air from central air lines in the lab. In MAS experiments, the rotor is driven at 10 kHz. All experiments are performed at room temperature.

The only NMR experiment used in this study is signal acquisition following a single 90° pulse. The length of the 90° pulse is 3.17 μs. This is calibrated by using half the length of a 180° pulse, which is the pulse length required for there to be no or minimal observed signal following a single pulse. 16 accumulations are collected to provide an adequate signal-to-noise ratio with a repetition time, T_R, of 60 s for dry samples and 3 s for all others. The conventional minimum T_R required for the system to fully recover to equilibrium is dictated by the longest T_1 in the system, given by the equation,

$$T_R = 5\,T_1 \tag{65}$$

Since the addition of any water to a MCM-41 sample provides additional relaxation pathways for the spin system to relax, longer T_1 values are found in dry MCM-41 compared to wet. Previous work [89] has found dry MCM-41 to have a T_1 of around 7 s, while for wet samples it is closer to 220 ms. Therefore, T_R = 3 s is more than adequate for the wet samples, as is 60 s for the dry. Despite the preexisting knowledge about the MCM-41 system and its related T_1 times, these repetition times are frequently checked to ensure that they are sufficient for the system to return to thermal equilibrium.

The same receiver gain is used for all experiments to allow accurate comparison of absolute signal magnitude across all sample materials and conditions. This is not to the detriment of signal resolution in any case, as all signals are still well inside the digitization range of the receiver.

The time-domain signal is then Fourier transformed to the frequency domain to provide the spectra used. The recorded spectra are 100 kHz wide. While the spectrum from the MCM-41 is less than 5 kHz wide under MAS conditions, there is a broad background signal originating from the rotor and coil that is roughly 50 – 70 kHz wide. The additional bandwidth establishes a true background and

aids in signal processing.

All chemical shifts are referenced to 4,4-dimethyl-4-silapentane-1-sulfonic acid (DSS), a standard NMR reference material [51]. A solution of DSS is prepared and added to the same type of rotor used for experiments, in order to keep conditions as similar as possible between the two.

5.4. Sample Preparation for Hydration Study

Before the hydration study can commence, the samples go through a hydroxylation procedure to ensure a fully hydroxylated surface in each test. Several times the required amount of the MCM-41 of interest (pristine, Pd or reduced Pd) is measured into a glass vial and covered with three to four times its volume of ultra pure water. A light vacuum is applied to draw the air out of the material's pores, and equivalently, water into them, to ensure all surfaces are in contact with water. This point is reached when bubbles are no longer visibly leaving the submerged powder. The sample is left to soak for 48 hours. It has been shown that this procedure is sufficient to ensure complete hydroxylation of the MCM-41 pore surface [90]. Excess water is then removed from the glass vial using a pipette and the sample is dried under vacuum ($< 10^{-6}$ bar). The vacuum chamber is heated to 353 K to prevent the excess water from freezing and to aid in drying.

The hydroxylation process is not carried out on the NH_4-MCM-41 and oxide-cleaned MCM-41 samples as the water bath would alter their desirable chemical features. Furthermore, the only hydration states investigated for these samples were dry NH_4-MCM-41 and ambiently wetted oxide-cleaned MCM-41; not a full hydration study.

To prepare the MAS rotor (with cap) that will be used in the NMR experiments, it is washed with ethanol and rinsed with distilled water three times. It is then dried under vacuum for 30 – 60 min and weighed. An NMR measurement of the empty rotor is taken to aid in processing of the NMR

signals later on.

The cleaned and dried rotor is packed with enough MCM-41 sample to fill it and still fit the cap on, after lightly tamping it down. The rotor and cap, without the cap sealing the rotor, are dried under vacuum for at least 24 h. The vacuum chamber containing the sample is then sealed, removed from the vacuum system and placed in a glove box. Under a dry nitrogen atmosphere, the vacuum chamber's seal is slowly opened, as rapidly admitting nitrogen would blow powder out of the rotor. The vacuum chamber is then opened and the rotor's cap can be affixed, still under nitrogen, to prevent atmospheric water vapor from hydrating the sample. This sample is then weighed and the empty rotor mass subtracted to determine the dry sample mass. This sample's NMR spectrum is measured as described above.

In order to obtain a hydrated sample, the dry sample is opened to the ambient, laboratory atmosphere. The water vapor naturally present in air will adsorb onto the dry pore surface. This hydration mechanism has two main benefits: i) it is slow, and therefore can be more finely controlled, by varying the amount of time the cap is removed for, than liquid water hydration; and ii) since the vapor phase is being used, the water reaches the entire surface much quicker than adding liquid water would allow. Once the appropriate time has passed, the cap is replaced and the sample weighed, to determine, within a few μg, how much water as been added to the sample. The sample's NMR spectrum is again measured. Once the sample is removed from the magnet, the mass is measured again to ensure that the sample's seal was not compromised at any point, changing the hydration of the sample during the measurement process.

This procedure is repeated, recording the NMR spectrum at each subsequent hydration level, until the sample is reasonably saturated with water. This saturation is chosen to be when the sample no longer gains significant water mass in a reasonable amount of time via exposure to ambient laboratory

air. The sample is then dried once more and this process is repeated to obtain measurements at more hydration levels. These levels are chosen so that, between the two separate runs, the sample's NMR spectrum is recorded at hydration levels that are evenly distributed across the full hydration range from dry to saturation.

5.5. Processing and Fitting NMR Spectra

After measurement, each spectrum is phased by hand and the baseline is subtracted using the same program as was used for data acquisition: Bruker's XWIN-NMR. Baseline subtraction is performed using an automated spline fitting based on 35 – 40 points chosen by the user.

Spectrum fitting is carried out in Origin Pro, which uses a Levenberg–Marquardt algorithm for least square fitting. Multiple Lorentzian waveforms are used, the number of which depends on the sample. The equation describing a point on one of these peaks is,

$$y(x)=\left(\frac{2A}{\pi}\right)\frac{w}{4(x-\delta)^2+w^2} \tag{66}$$

where A is the peak's area, the position of its center on the horizontal axis is δ (ie. the peaks chemical shift), and its full width at half maximum, w.

6. Results

6.1. Sample Characterization

The physical appearance of all samples studied is of a fine powder, though each sample is a different color The pristine MCM-41 and NH_4-MCM-41 are white; Pd-MCM-41 is a light brown or tan color; and the reduced Pd-MCM-41 and oxide-free Pd-MCM-41 are a dark gray. The 15 point BET nitrogen adsorption isotherms for pristine MCM-41, Pd-MCM-41 and reduced Pd-MCM-41 are shown in Figure 21 and the specific surface areas calculated from them, using equations (59) and (60), are shown in Table 1. Full, 25 point nitrogen adsorption isotherms for the pristine and palladized samples are given in Figure 22, revealing the expected Type IV isotherm behavior. Figure 23 shows the pore-size distributions corresponding to the full isotherms of Figure 22. XRD diffractograms are shown in Figure 24 for the same two samples. Table 2 shows the values of d_{pore} and d_{wall} calculated from the (100) reflection in each diffractogram in Figure 24, using equations (56) – (58). In these calculations, the pores of the material are assumed to have a circular cross-section so that the shape factor, c, used in equation (58) is 1.213 [74, 91]. Also, the pore walls are assumed to be amorphous silica, with a ρ of 2.2 g/cm^3 [91], and V_p is taken to be 0.91 cm^3/g [91]. The latter value is determined by the chain length of the surfactant used in the synthesis process. CTABr is used as the surfactant for all samples, which has a chain length of 16 [91]. Electron microscopy images, taken from Dr. Guthrie's thesis [87], are shown in Figures 25 – 27. These images were obtained from measurements on samples prepared under identical conditions to those used in the current study.

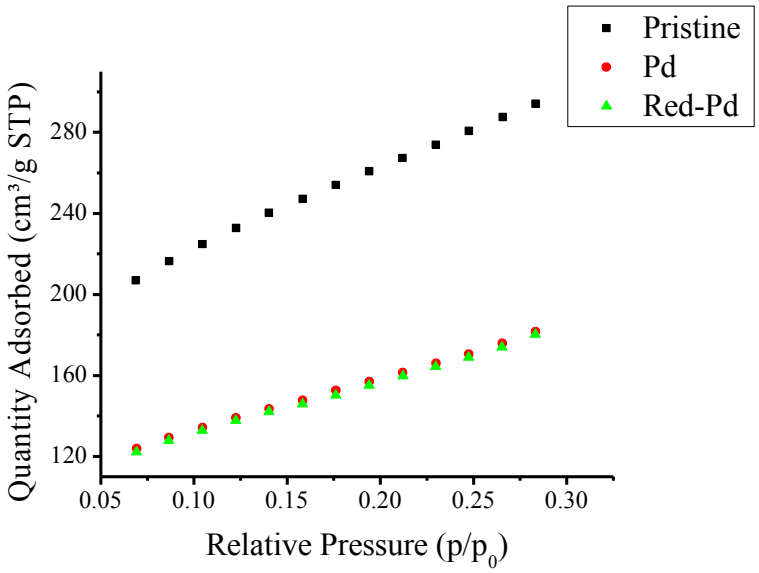

Figure 21: 15 point N_2 adsorption isotherms detailing the linear portion of the isotherms for pristine MCM-41, Pd-MCM-41 and reduced Pd-MCM-41.

Material	**Specific Surface Area (m^2/g)**
Pristine MCM-41	942 ± 3
Pd-MCM-41	582 ± 2
Reduced Pd-MCM-41	577 ± 3

Table 1: Specific surface areas of the various MCM-41 materials studied, calculated from the isotherms in Figure 21.

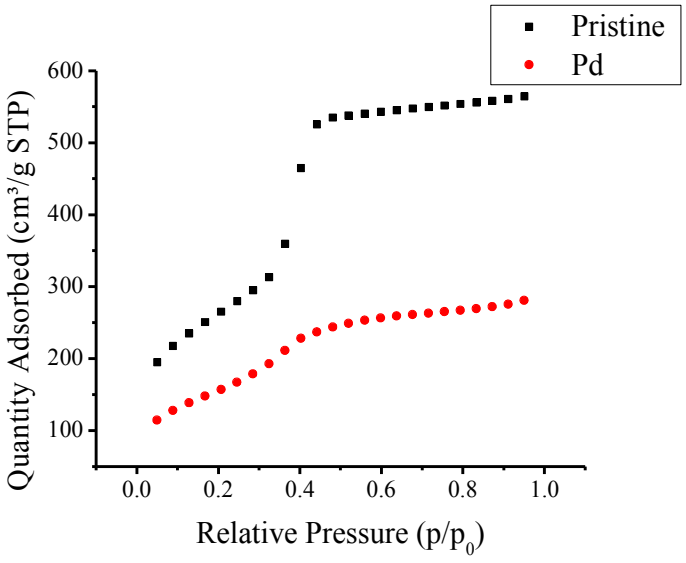

Figure 22: Full, 25 point N_2 adsorption isotherms for the pristine MCM-41 and Pd-MCM-41 samples.

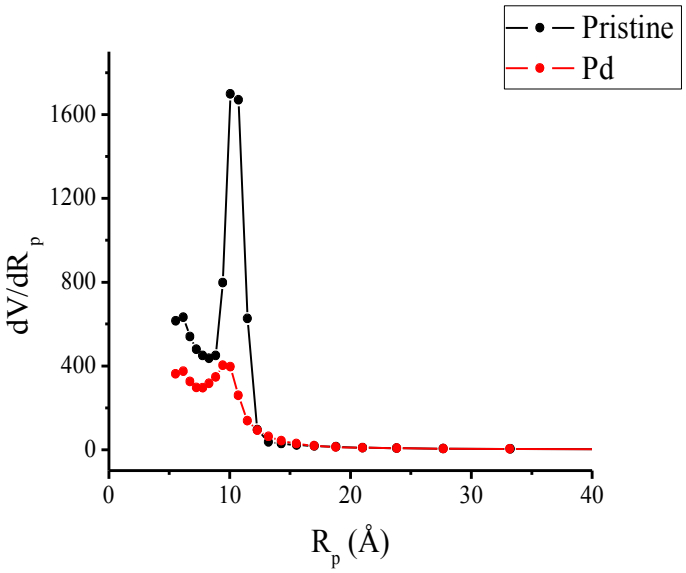

Figure 23: Pore size distributions for the pristine MCM-41 and Pd-MCM-41 samples, calculated from the isotherms in Figure 22.

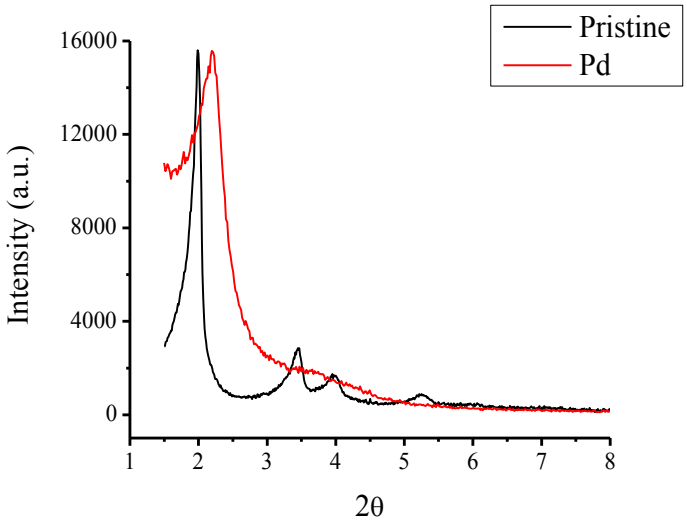

Figure 24: XRD diffractograms for the pristine MCM-41 and Pd-MCM-41 samples, normalized to match primary peak intensities.

Material	**2θ (100) (°)**	**d_{100} (nm)**	**a (nm)**	**d_{pore} (nm)**	**d_{wall} (nm)**
Pristine MCM-41	1.99	4.44	5.13	4.40	0.73
Pd-MCM-41	2.20	4.02	4.64	3.98	0.66

Table 2: Mesopore details of pristine MCM-41 and Pd-MCM-41 calculated from the position of the (100) reflection in their XRD diffractograms.

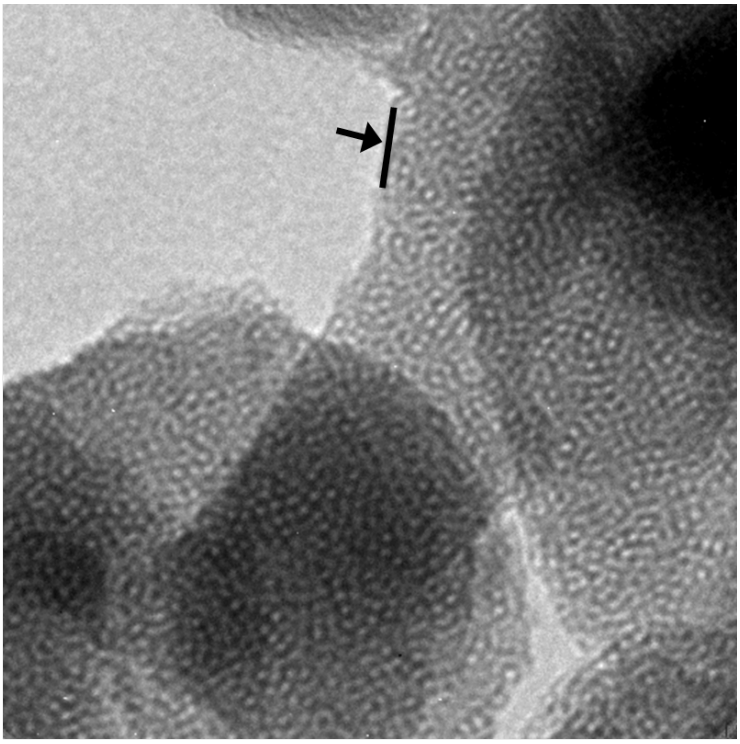

Figure 25: TEM image of pristine MCM-41. The material shown was prepared using the same synthesis procedures as those in the present study. The scale is such that the width of the entire image is 200 nm. The black line indicated by the arrow delineates the boundary of a MCM-41 particle. Taken from reference [87].

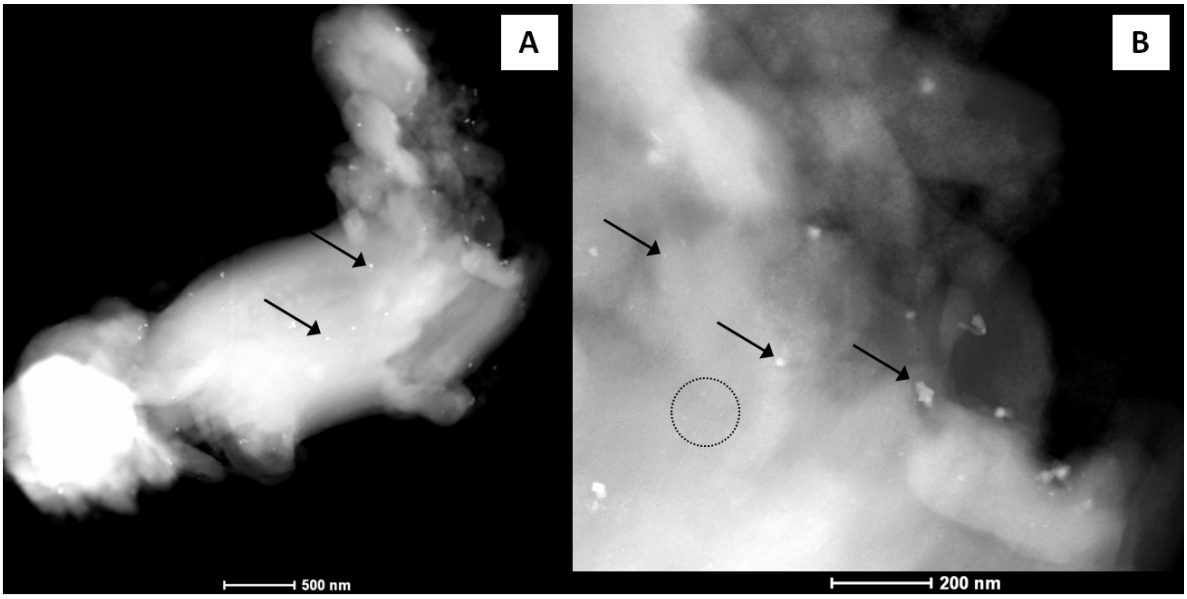

Figure 26: SEM image of Pd-MCM-41. The material shown was prepared using the same synthesis procedures as those in the present study. The loading of the material shown is 0.12 % Pd by weight. The two images, A and B, are of the same sample at two different magnifications. The arrows in the images are indicating Pd metal clusters. The dashed circle indicates a region where there may be smaller Pd particles, but the limited resolution of the image prevents conclusive identification. Taken from reference [87].

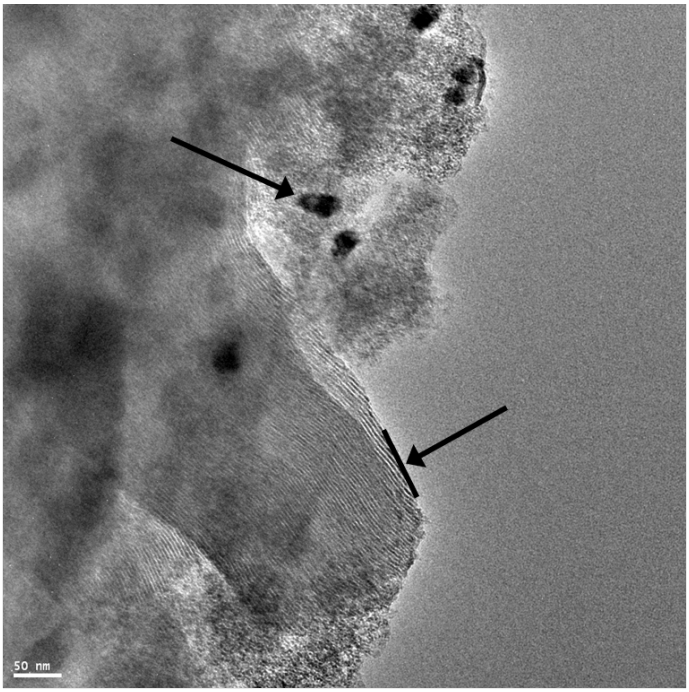

Figure 27: TEM image of Pd-MCM-41. The material shown was prepared using the same synthesis procedures as those in the present study. The loading of the material shown is 0.12 % Pd by weight. The black line indicated by the arrow delineates the boundary of the MCM-41 particle. The other arrow is indicating a Pd cluster. Taken from reference [87].

6.2. Dry Samples

A comparison of the spectra obtained from the dry samples is shown in Figure 28. In a perfectly dry state, all the observed signal is only from the protons on the surface silanol groups. The spectra clearly exhibits two unique spin groups, and so the total signal is decomposed into two Lorentzian lines, shown in Figure 29.

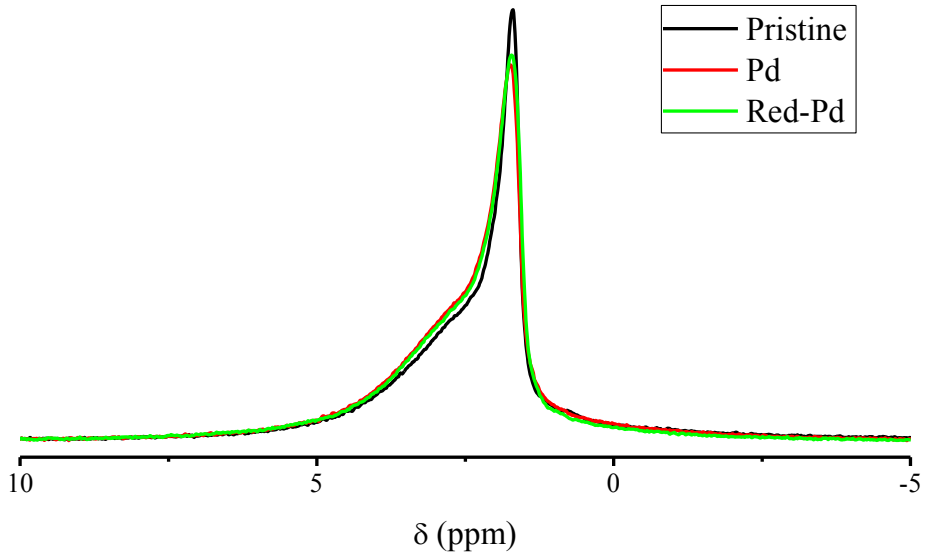

Figure 28: Comparison of ^{1}H MAS NMR spectra of dry samples of pristine MCM-41, Pd-MCM-41 and reduced Pd-MCM-41.

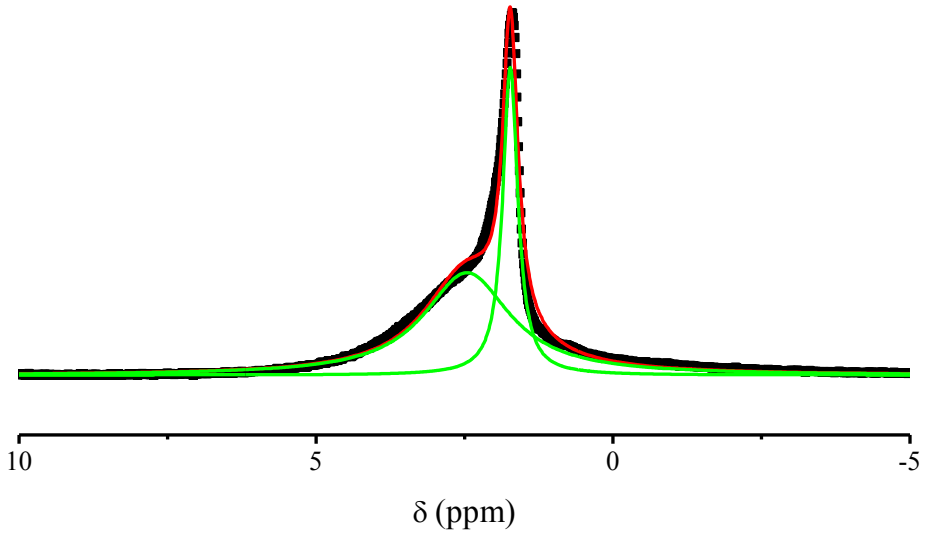

Figure 29: Spectral fitting of two Lorentzian lines to the ^{1}H MAS NMR spectrum of dry, pristine MCM-41.

By obtaining the signal from a known volume of water at the same gain setting as those used for sample measurement, the proportionality of received signal to the number of protons in the sample can be determined. In this way, the absolute number of hydroxyl groups in a particular sample is calculated. Using the mass of the sample, the specific surface area from Table 1 and the hydroxyl content, the surface hydroxyl density is calculated. Relative populations of the two types of hydroxyl groups, single OH (SOH) and hydrogen-bonded OH (HBOH), are calculated as well, based on the relative areas of their associated peaks. This information is summarized in Table 3.

Material Type	Sample Mass (g)	Number of Hydroxyl Groups, n_{OH} (x 10^{19})	Hydroxyl Density (n_{OH}/nm^2)	Relative Population of SOH Hydroxyls	Relative Population of HBOH Hydroxyls
Pristine MCM-41	0.02550	8.64	3.61	0.36	0.64
Pd-MCM-41	0.03798	8.77	4.02	0.39	0.61
Reduced Pd-MCM-41	0.03229	7.21	4.04	0.40	0.60

Table 3: Hydroxyl content of each sample.

For a qualitative comparison to the above dry (and later wet) spectra, a measurement was made of dry NH_4-MCM-41. This spectrum is shown in Figure 30, revealing an additional peak at ~ 7 ppm, attributed to the NH_4 groups on this sample's pore surface.

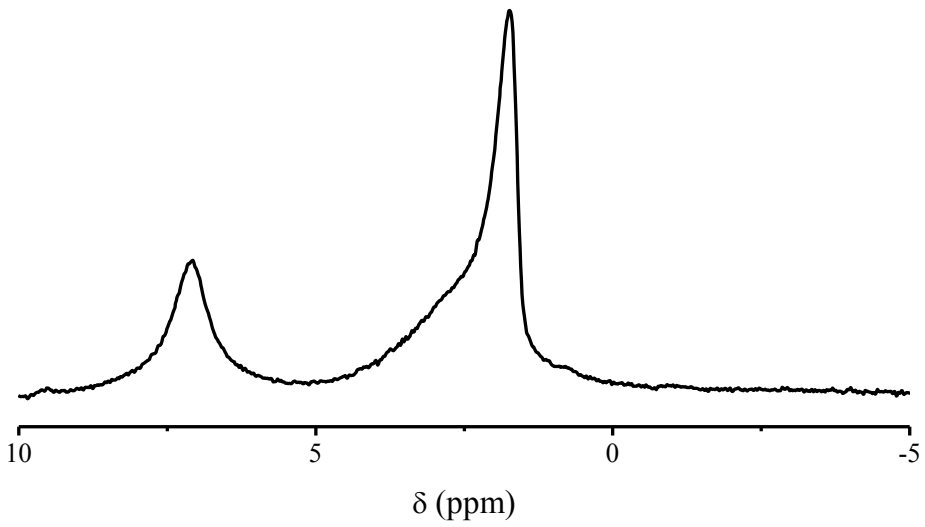

Figure 30: ^1H MAS NMR spectrum of dry NH_4-MCM-41.

6.3. Hydration Study

Due to the small amounts of water being studied on such large surface areas, the amount of water in a sample will be reported as the fraction of a monolayer of water molecules (ML) present on

the surface. The hydration level is defined this way in order to normalize the amount of water to the surface area of each sample, which varies based on the material, as shown in Table 1. In this definition, a common [21] approximation is made: a single water molecule occupies a square patch of surface whose side length is 3 Å. The number of monolayers of water is determined by multiplying the number of water molecules, determined based on water mass, by 9 $Å^2$, then dividing this by the total area contained in the sample, determined from the BET surface area and the mass of the sample. To be clear, this method of defining the hydration level does not make any suggestions about how the water molecules coordinate themselves on the surface (since well before one ML is reached, water molecules will begin layering themselves), rather it reports the two-dimensional area the water could occupy, if arranged in a single layer, per unit of material surface area. These values, the water mass and the number of ML of water, along with the duration of exposure to ambient lab air required to obtain them, are reported for each sample in the table at the start of each of the following sections (Tables 4, 5 and 6).

Selected, representative spectra of similarly hydrated samples (0.08, 0.15, 0.24 and 0.50 ML) are also presented at the start of each section in order to provide a visual reference for the spectral features being discussed (Figures 31, 34 and 39). Each graph shows the original data, the modeled spectrum resulting from the fitting process and the individual peaks which it is composed of. Graphs of all spectra obtained and fit are shown for all samples in Appendix A. Each graph again contains a plot of the original data and the modeled spectrum.

The general approach to fitting the spectra resulting from the experiments outlined in the Materials and Methods section is to apply and extend the Walia model [21], which is detailed in section 4.3.1. As mentioned there, this model was originally applied to a commercially prepared pristine MCM-41 up to a hydration of 0.2 ML. The current study applies this model to hydration levels up 0.5

ML in laboratory synthesized pristine and palladized MCM-41. Therefore, minor refinements and adjustments are required to successfully apply the model in the current study.

As in its original application, the model assumes that the HBOH group remains unchanged with hydration, particularly in population, and thus peak area. As such, this parameter is fixed in all fittings. For the initial fitting attempt, this is the only fixed parameter. All other parameters, for the HBOH and other peaks, are left as floating variables to be fit by the minimization routine. Based on the results of this first attempt, the need for a more "global minimum fit" is indicated, refinements are added to the fitting routine, based on sound physical arguments, in order to correct inconsistencies in data trends and arrive at the most reasonable fitting of the entire data set. Below, the details of this process are outlined for each sample along with the results. Further discussion for the choices made in fitting refinements, and why some of the issues in the fitting arise in the first place, are found in the next chapter. The parameter values presented below, summarized in graphs, are those from the final fitting procedure, with all refinements and adjustments included.

6.3.1. Pristine MCM-41

Water Mass (mg) (± 0.02 mg)	Air Exposure (min) (± 1 min)	Hydration Level (ML)
0	0	0
0.27	12	0.035
0.35	21	0.044
0.67	34	0.086
0.82	51	0.10
1.09	65	0.14
1.52	126	0.19
1.78	134	0.23
3.10	460	0.39
3.97	699	0.51

Table 4: Summary of the vapor phase hydration of pristine MCM-41.

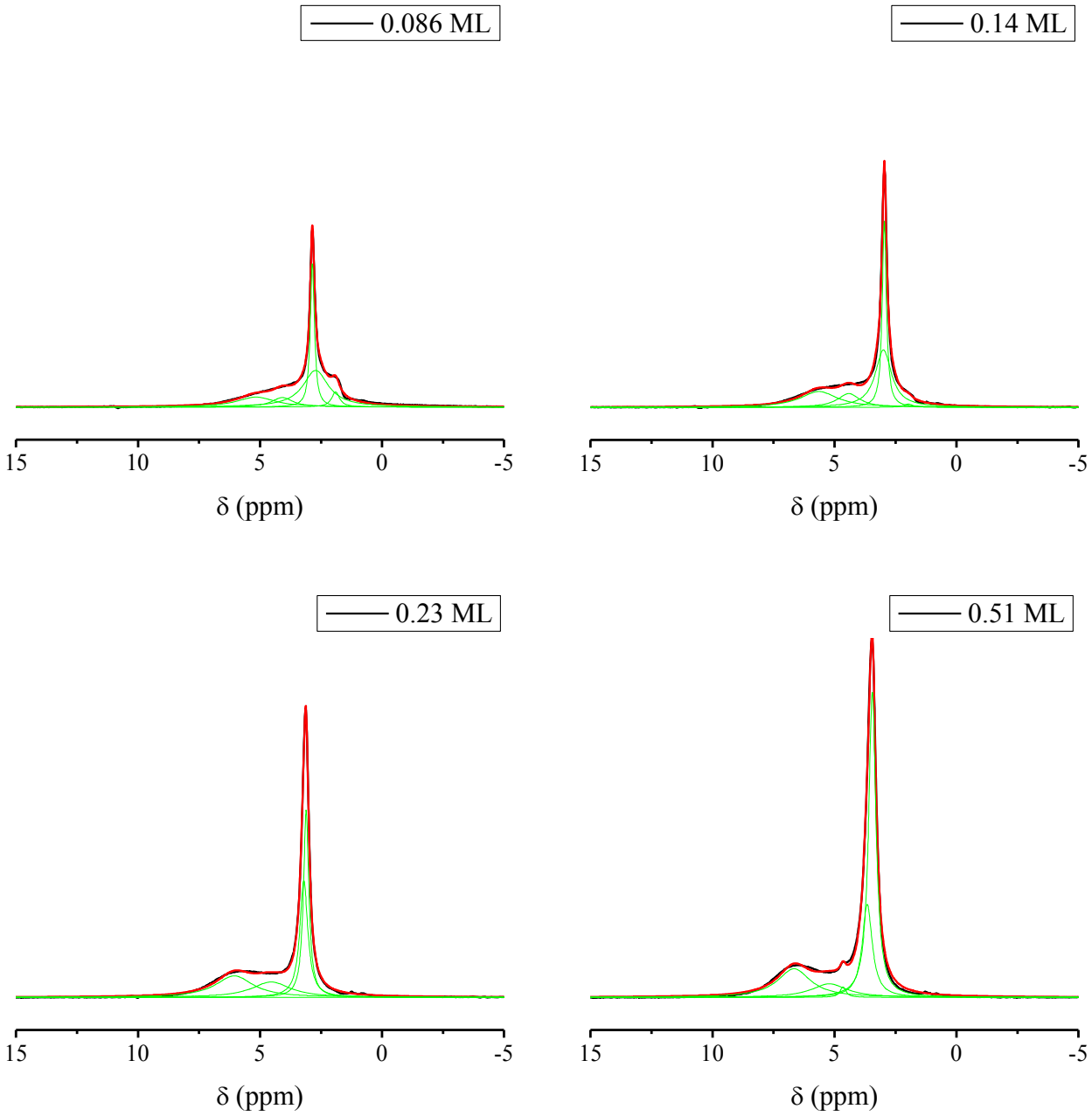

Figure 31: Selected, representative ^{1}H MAS NMR spectra of pristine MCM-41. The hydration level of each spectrum is noted next to its graph. Each graph shows the original data (black), the calculated model (red) and the individual peaks (green) that the model is composed of. The same scale is used in each graph.

The results of the first fitting of the pristine MCM-41 spectra with all parameters floating, except the area of the HBOH peak, was successful for most of the hydration range. The only issue with the fitting occurred in the vicinity of the upper hydration limit used by Walia in the application of

the original fitting model, 0.10 – 0.19 ML. Before and after this hydration range, clear trends exist in area, chemical shift and width for all peaks. In the 0.10 – 0.19 ML hydration range, the results of the initial fitting suggest different trends. For example, the initial fitting suggests that the HBOH peak might become wider with increasing hydration and the area of the HBOH water peak might become very small. Investigation of these alternative trends (ie. refitting the entire data set in a way to encourage these trends to develop across the entire hydration range) results in values for many parameters that are essentially non-physical and cannot be supported by the model's understanding of the material. Specifically, the HBOH peak has a tendency in this hydration range to be pushed far downfield and eventually become very broad, which is highly unlikely since the HBOH is presupposed to be the least affected by the presence of water. The chemical shift of the hydrated SOH peak is also pushed downfield as far as 6.5 ppm at higher hydration levels, but the theoretical limit for this peak is 5.5 ppm, the shift of a hydrogen-bonded silanol group [21]. Therefore, these alternative trends are deemed to be invalid and the intermediate hydration range, 0.10 – 0.19 ML, requires an additional constraint in the fitting process. In keeping with the assumption that the HBOH groups are least influenced by water, the width of this peak is fixed in the spectra of the samples containing 0.10, 0.14 and 0.19 ML.

The widths of the HBOH peak at 0.10, 0.14 and 0.19 ML are chosen to be 1.1, 0.8 and 0.6 ppm, respectively. These values are selected in order to establish a smooth transition in parameter trends between the lower and higher hydration ranges. Overall, the width is decreasing smoothly until 0.2 ML, then roughly constant above that point. In making these choices, particular attention was paid not only to the trend of the HBOH peak's width, but that of the hydrated SOH groups as well, since this peak is affected the most by changes to the HBOH peak. The SOH water peak, though closer in chemical shift to the HBOH group than the hydrated SOH group, is large and narrow (seen at around 3

ppm in Figure 31), making it well-defined and very tolerant to changes in other peaks.

Another refinement to the model has to be made for the highest hydration measure where, as can be seen at 4.5 ppm in the 0.51 ML graph of Figure 31, an additional peak forms. This is evidence of a new spin environment developing at this hydration, which will be called pore filling water for the time being.

The parameters from the fitting procedure that includes the fixed HBOH widths and new pore filling water peak are shown in Figures 32 and 33.

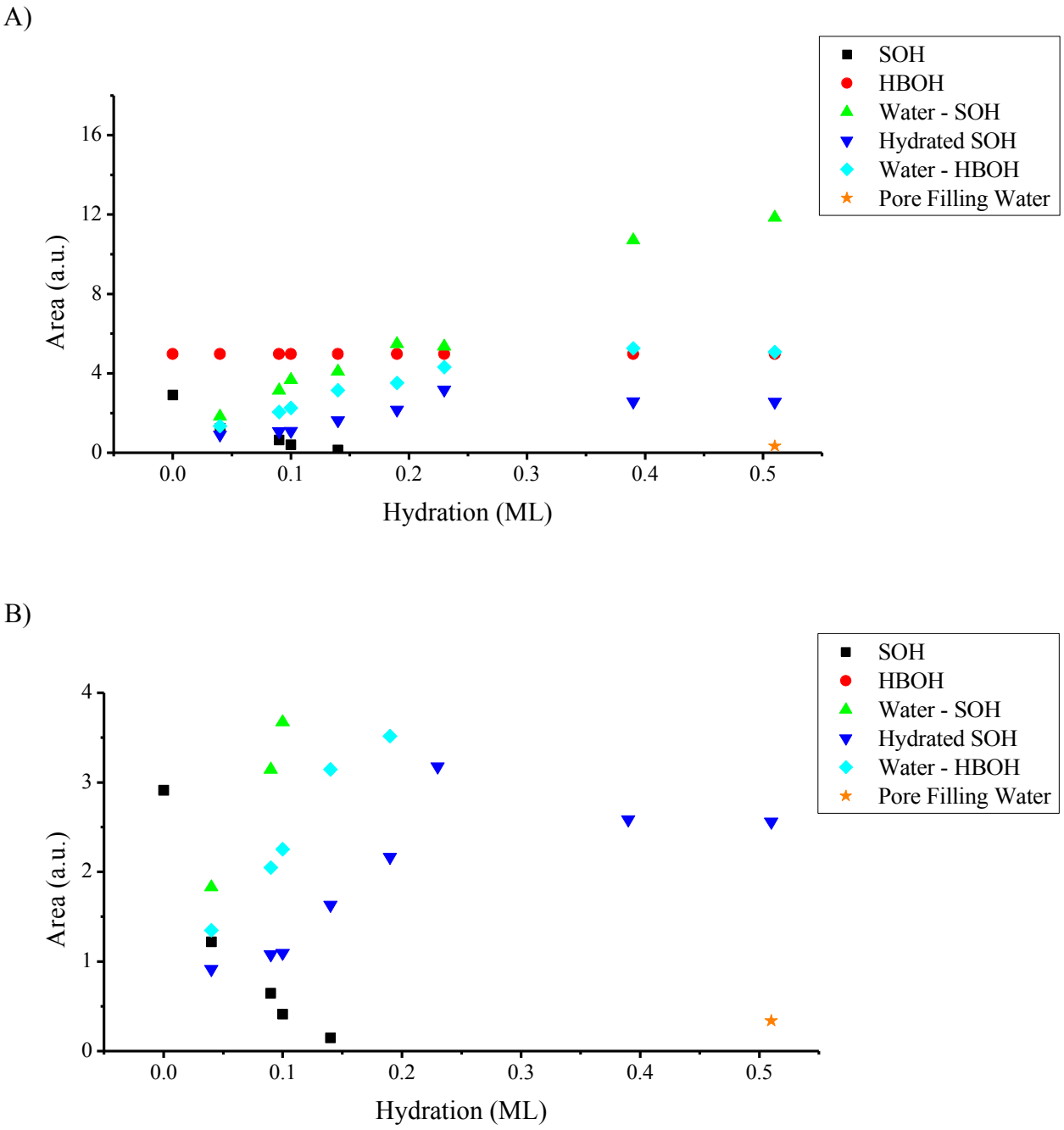

Figure 32: (A) Plots of the peak areas for pristine MCM-41. (B) The same plot as (A) but with a reduced vertical scale in order to show the details of the smaller peak areas.

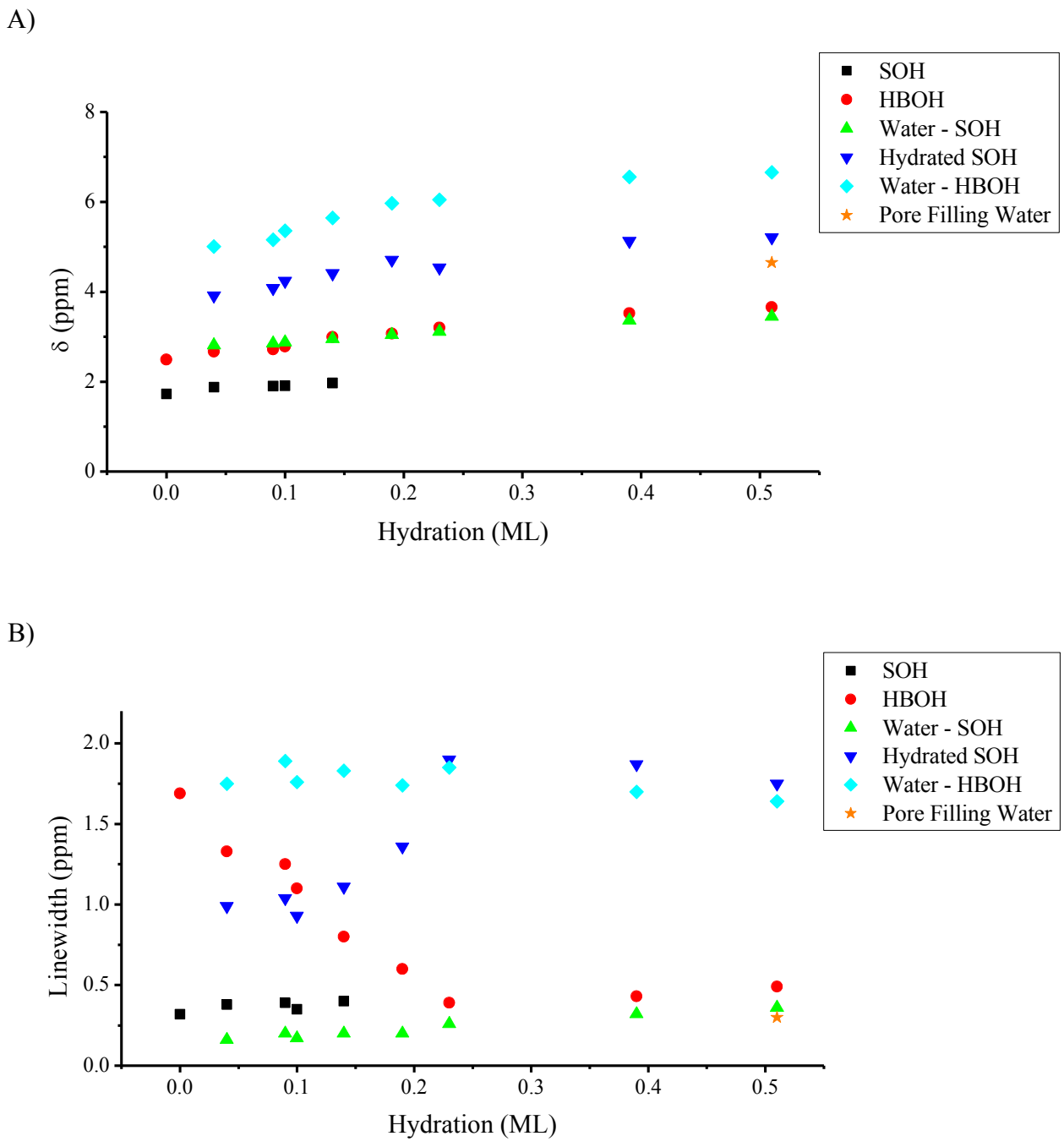

Figure 33: Plots of the chemical shift, δ (A) and linewidth (B) for pristine MCM-41.

6.3.2. Pd-MCM-41

Water Mass (mg) (± 0.02 mg)	Air Exposure (min) (± 1 min)	Hydration Level (ML)
0	0	0
0.49	22	0.069
0.55	23	0.075
1.02	40	0.14
1.45	62	0.20
1.76	111	0.25
1.97	92	0.27
2.51	128	0.34
3.03	170	0.41
3.64	321	0.51

Table 5: Summary of the vapor phase hydration of Pd-MCM-41.

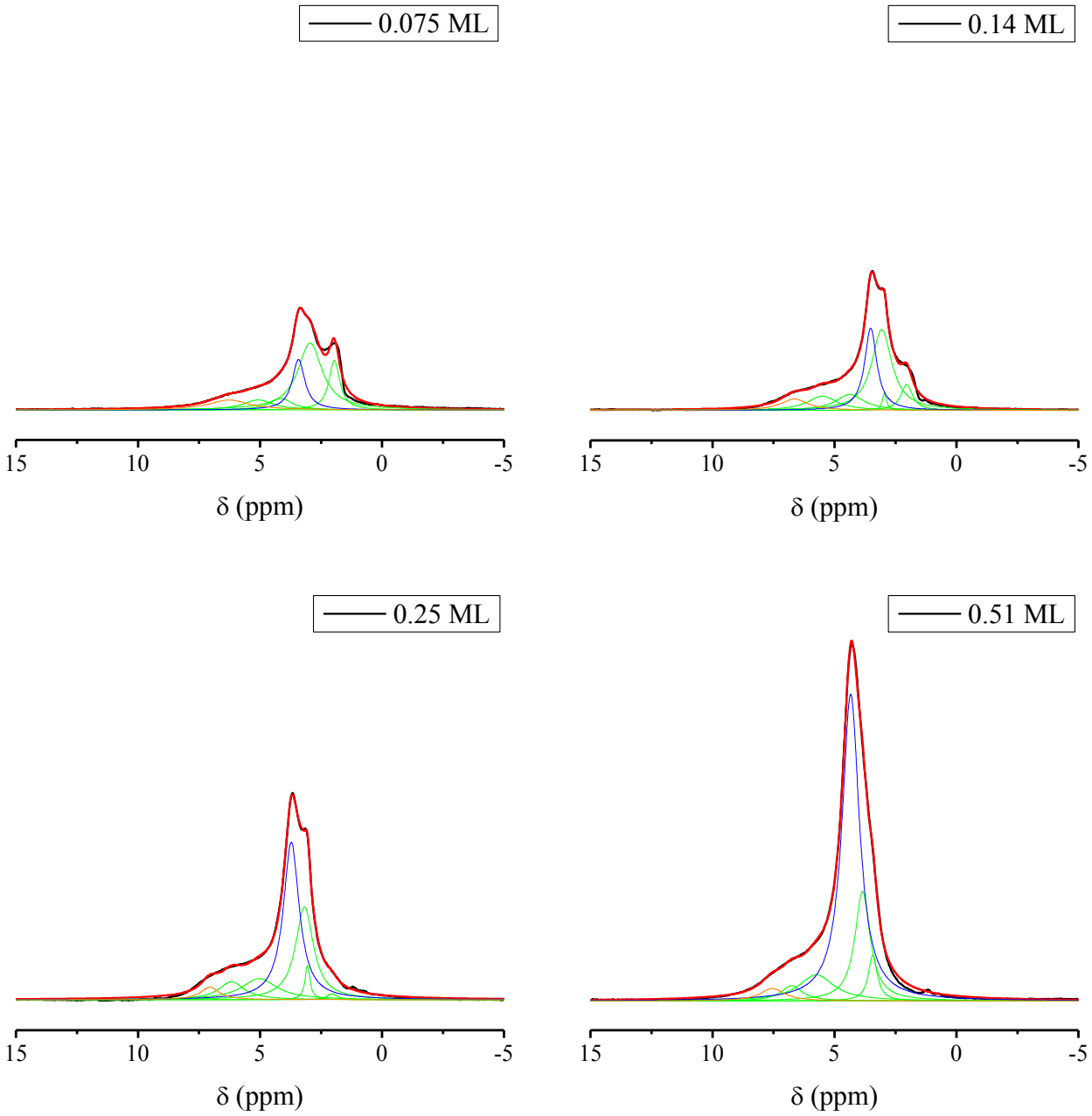

Figure 34: Selected, representative ^{1}H MAS NMR spectra of Pd-MCM-41. The hydration level of each spectrum is noted next to its graph. Each graph shows the original data (black), the calculated model (red) and the individual peaks (green – groups found in pristine MCM-41, blue – Pd Water Group 1, orange – Pd Water Group 2) that the model is composed of. The same vertical scale is used in each graph.

What is immediately obvious from the NMR spectra of Pd-MCM-41 in Figure 34 is that there is an additional peak at around 4 ppm. This large, broad peak seems to dominate the spectrum and so

an additional peak must be added in the fitting routine to account for it. As it is not present in the pristine MCM-41 samples, it must be due to the Pd clusters present in Pd-MCM-41. Also, it is not present in the dry spectrum, so it must be caused by the protons added in the form of water molecules. This peak will therefore be referred to as Pd Water Group 1. This peak is shown in blue in Figure 34.

Due to the overall broad and poorly defined nature of these spectra, the initial attempts to fit them has several difficulties. These spectra are separated into two chemical shift ranges 2.0 – 4.5 ppm and 4.5 – 8.0 ppm. Changes made to the peaks in either of these two regions essentially only affect the peaks within the same region.

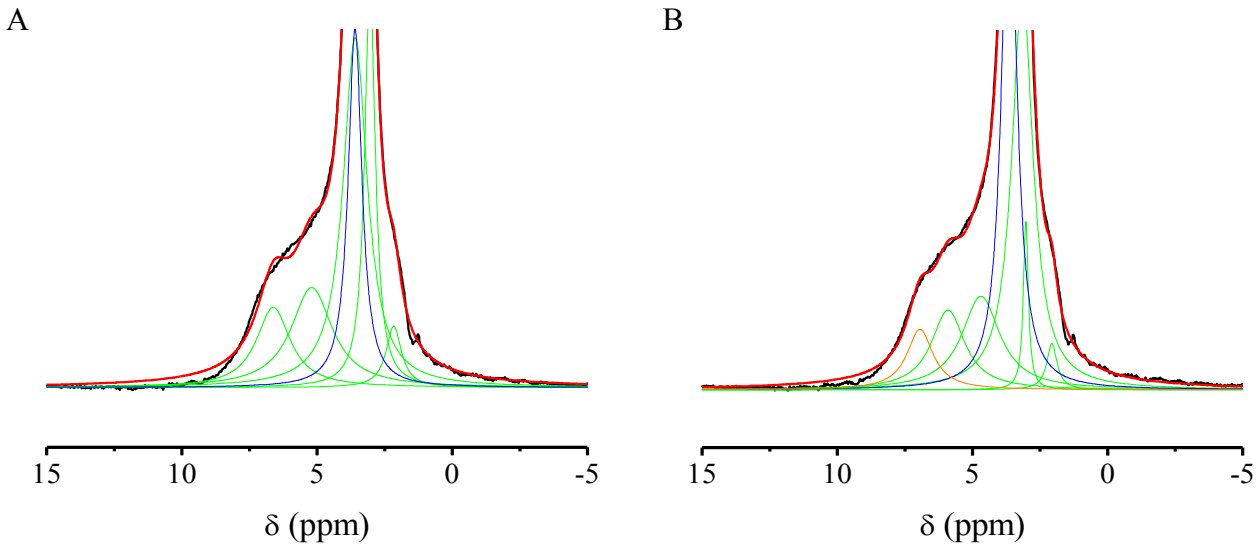

Figure 35: Comparison of the results of the fitting procedure, without (A) and with (B) a peak for Pd Water Group 2 in the model. The vertical scale has been reduced to emphasize the high ppm region of interest. Each graph shows the original data (black), the calculated model (red) and the individual peaks (green – groups found in pristine MCM-41, blue – Pd Water Group 1, orange – Pd Water Group 2) that the model is composed of.

The fitting attempt with all variables floating results in the high ppm region not fitting properly with only two peaks, as illustrated in Figure 35. Also shown in this Figure is the solution to this problem, which is to add another peak in the high ppm region. Similar to the peak identified as Pd

Water Group 1, this peak due to water that is influenced by the Pd metal clusters, and so it will be identified as Pd Water Group 2. It is located downfield from the HBOH water peak, since without this additional peak in the fitting, the HBOH water and hydrated SOH peaks move to chemical shifts that are too high for their nature. This peak is shown in orange in Figure 34.

The issue in the lower ppm region is that, although it is clear that there are three peaks present (the two known from the pristine sample – SOH water and HBOH – and the new Pd Water Group 1), they are not well defined. This makes it difficult for the fitting routine to conclusively identify their details, especially since, other than the HBOH area, all the other parameters are floating. With different starting values for chemical shift, the fitting process yields different results. Carrying any of these trends through the entire data set leads to unlikely results for several peaks. In some cases, the HBOH peak has a chemical shift at 0.50 ML that is between 1.0 and 1.5 ppm downfield from its position in the dry spectrum. As mentioned previously, this peak is presupposed to be the least affected by the presence of water and so these fitting results are likely erroneous. Despite numerous changes to the fitting approach, phasing or baseline subtraction, this data set cannot be satisfactorily fit with the current number of floating variables; the parameters for both the SOH water and HBOH peaks stray from expectation, leaving too much uncertainty in the quality of the fit. Therefore, additional information is required.

In Figure 36, the NMR spectrum of hydrated, oxide-free Pd-MCM-41 is shown, along with spectra of similarly hydrated (untreated) Pd-MCM-41 and pristine MCM-41 for comparison. It is clear that the effect seen in Pd-MCM-41 is not caused by the Pd metal itself, but rather the oxide layer coating the metal clusters. The NMR spectrum of a hydrated, completely oxide-free sample of Pd-MCM-41 behaves much like that of pristine MCM-41. Therefore, the reduced Pd-MCM-41 provides a midway point between the pristine MCM-41 and Pd-MCM-41 systems, since only some of the oxides

have been removed in this sample. This sample essentially has the effect of the Pd reduced, but not eliminated, making it easier to discern its extent and details.

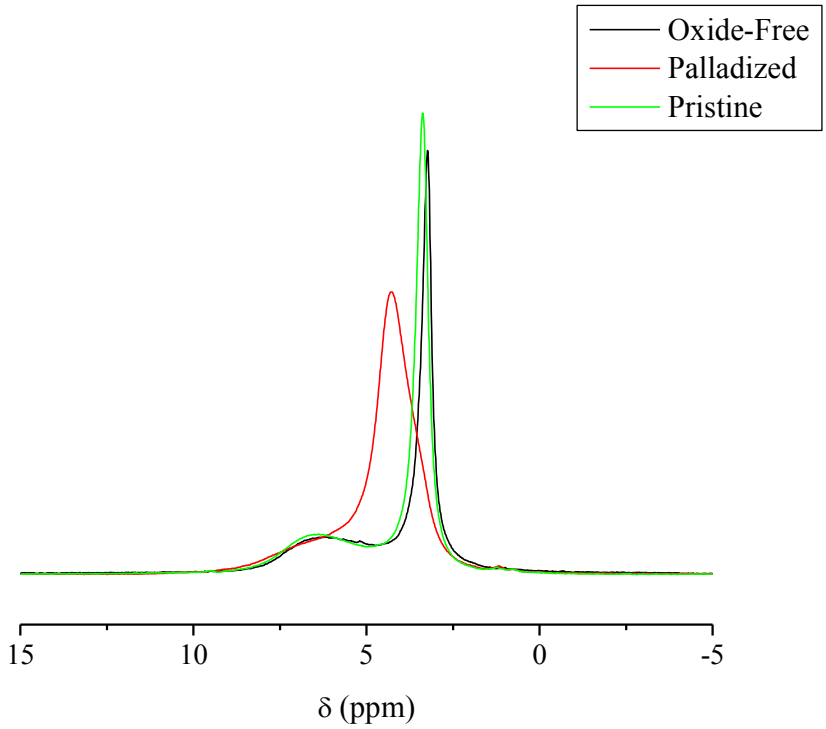

Figure 36: Comparison of the oxide-free Pd-MCM-41 to pristine MCM-41 and (untreated) Pd-MCM-41. The hydration level of each sample is around 0.5 ML.

It is at this point that the reduced Pd-MCM-41 sample is fit in order to provide the required additional information for the fitting of the Pd-MCM-41 sample. Covered in more detail in the following section, fitting this sample is straightforward. Due to the diminished effect of Pd (really the PdO), the peaks in the 2.0 – 4.5 ppm region are more resolved, and the data can be conclusively fit. It is found that the chemical shift of the HBOH group is almost identical to that of the pristine MCM-41 sample (a thorough comparison of the fitting of each sample can be found in the next chapter). It is therefore concluded that the HBOH chemical shift can be fixed in the Pd-MCM-41 sample to these same values.

By fixing the HBOH chemical shift, the ambiguity in the 2.0 – 4.5 ppm range is resolved. The only remaining issue is that the area of the hydrated SOH peak does not reach its expected maximum, the area of the SOH peak in the dry sample, despite the SOH peak having disappeared completely. It is deemed to be very reasonable to fix this area because of the successful results in the pristine MCM-41 sample. There, the hydrated SOH peak reached a maximum close to the dry SOH area. The introduction of the Pd does not affect the silanol groups, as seen in the section on dry samples above. There is no reason to believe that the SOH protons would have a different chemical shift in the Pd-MCM-41 sample as compared to the pristine MCM-41. Therefore, the area of the hydrated SOH peak is fixed at hydration levels above 0.20 ML. The trend of increasing hydrated SOH proton signal with decreasing SOH is maintained and continued until the SOH area drops to zero and the hydrated SOH peak is fixed at its maximum value.

The parameters that result from the fitting process that includes the above modifications to the fitting procedure are shown in Figures 37 and 38.

A)

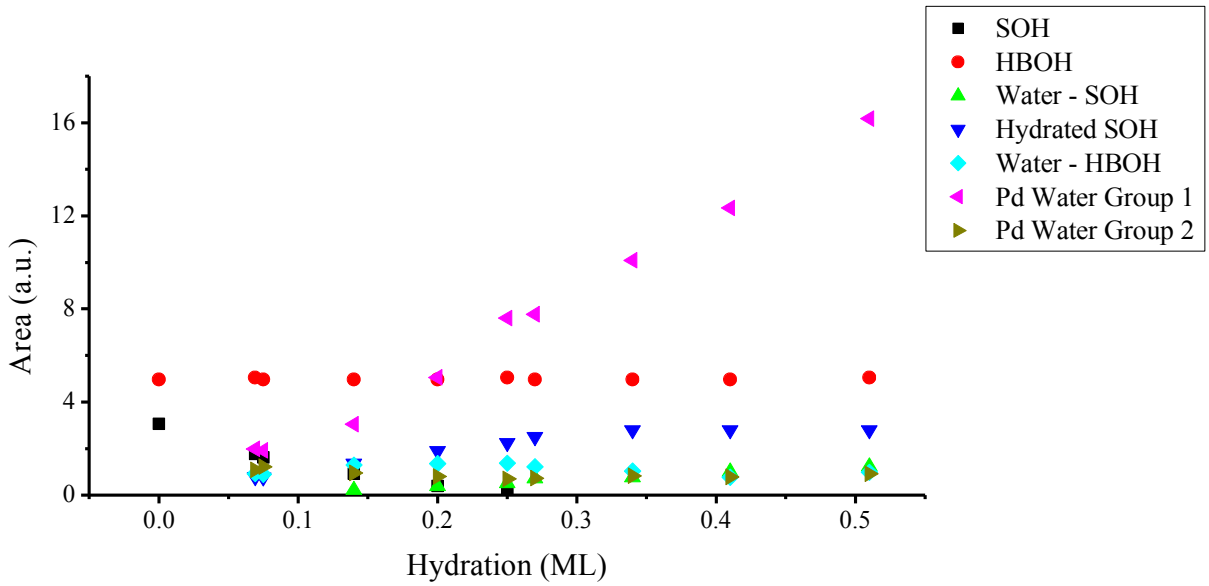

B)

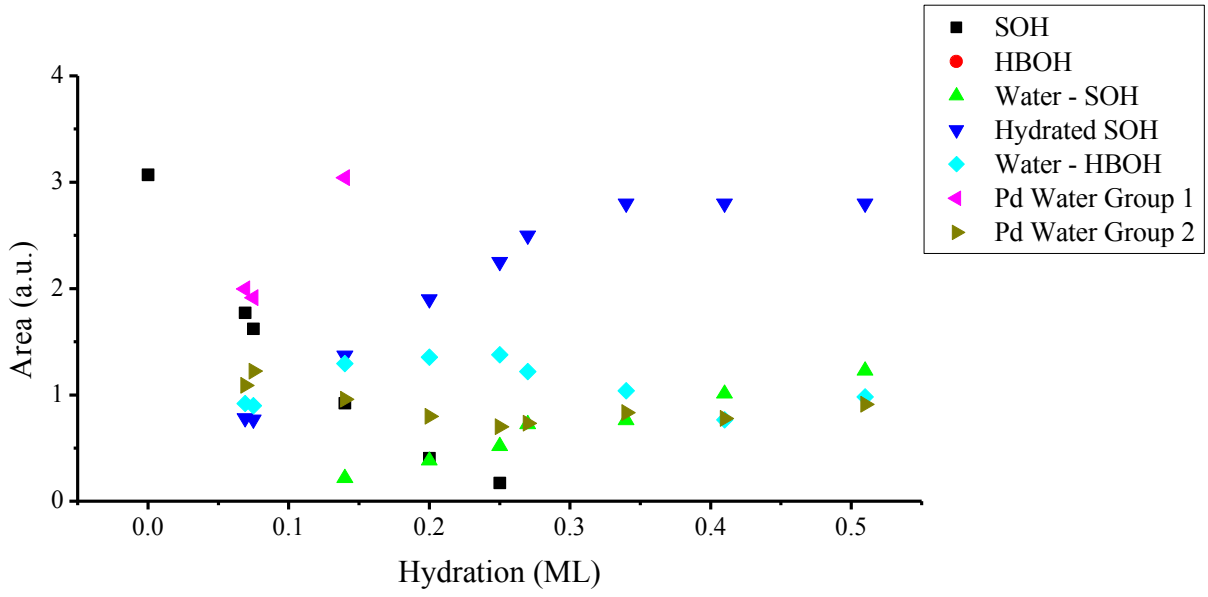

Figure 37: (A) Plots of the peak areas for Pd-MCM-41. (B) The same plot as (A) but with a reduced vertical scale in order to show the details of the smaller peak areas.

A)

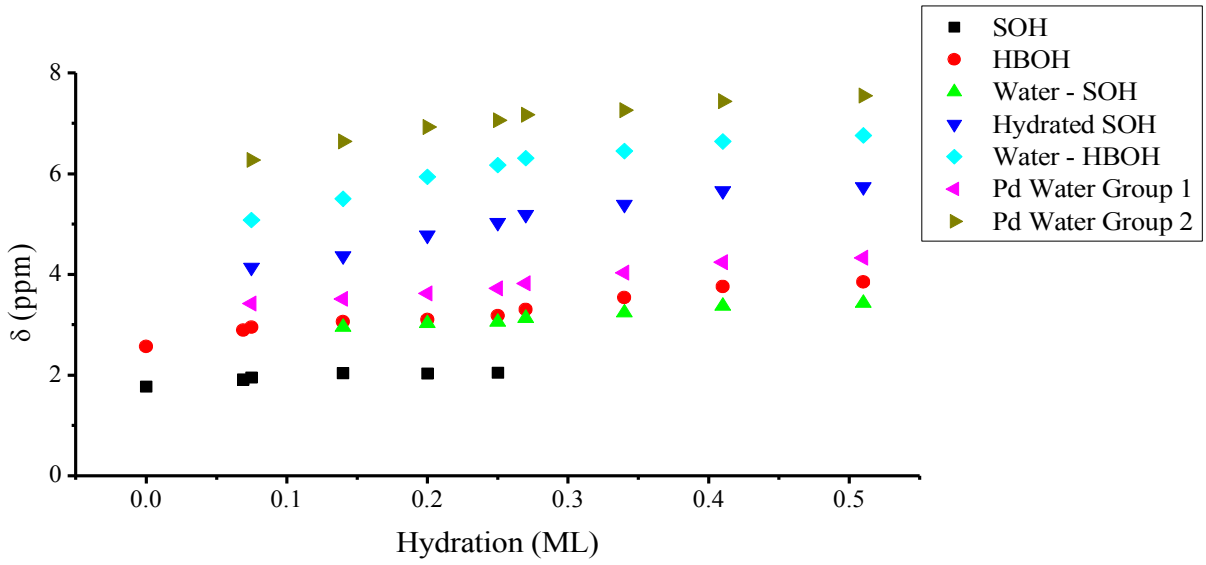

B)

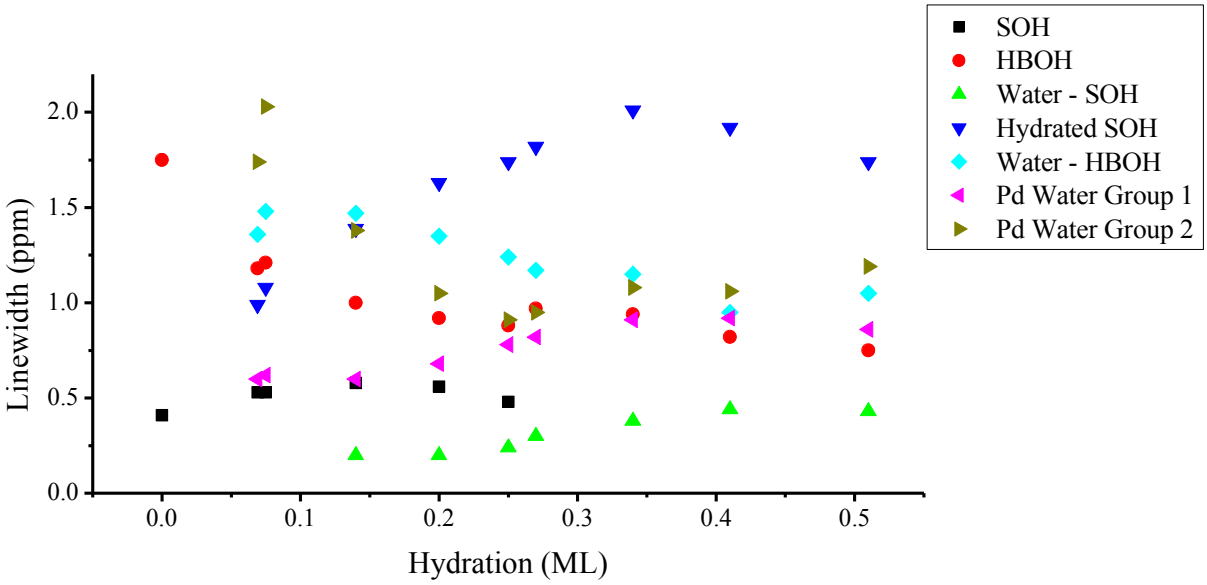

Figure 38: Plots of the chemical shift, δ (A) and linewidth (B) for Pd-MCM-41.

6.3.3. Reduced Pd-MCM-41

Water Mass (mg) (± 0.02 mg)	Air Exposure (min) (± 1 min)	Hydration Level (ML)
0	0	0
0.47	20	0.076
0.98	45	0.16
1.17	67	0.21
1.50	80	0.24
1.96	118	0.32
2.40	155	0.39
2.83	263	0.50

Table 6: Summary of the vapor phase hydration of reduced Pd-MCM-41.

As mentioned in the previous section, fitting the reduced Pd-MCM-41 sample succeeds easily. Comparing the reduced Pd-MCM-41 spectra in Figure 39 to the spectra for the pristine and palladized samples in Figures 31 and 34, respectively, it is clear that the qualitative character of the reduced Pd-MCM-41 spectra falls in between that of the other two samples, as mentioned in the previous section. Contrary to the difficulties in the Pd-MCM-41 sample, the 2.0 – 4.5 ppm region is more defined and so there are no issues with peak ambiguity. Similar to the other palladized sample, the hydrated SOH peak in the reduced Pd-MCM-41 sample does not reach its expected maximum value when left floating. For the same reasons as discussed in the previous section, fitting this area is considered to be acceptable. This and the addition of peaks for Pd Water Groups 1 and 2 are the only adjustments to the fitting procedure required for the reduced Pd-MCM-41 sample. The parameters from the fitting procedure that includes these changes are shown below in Figures 40 and 41.

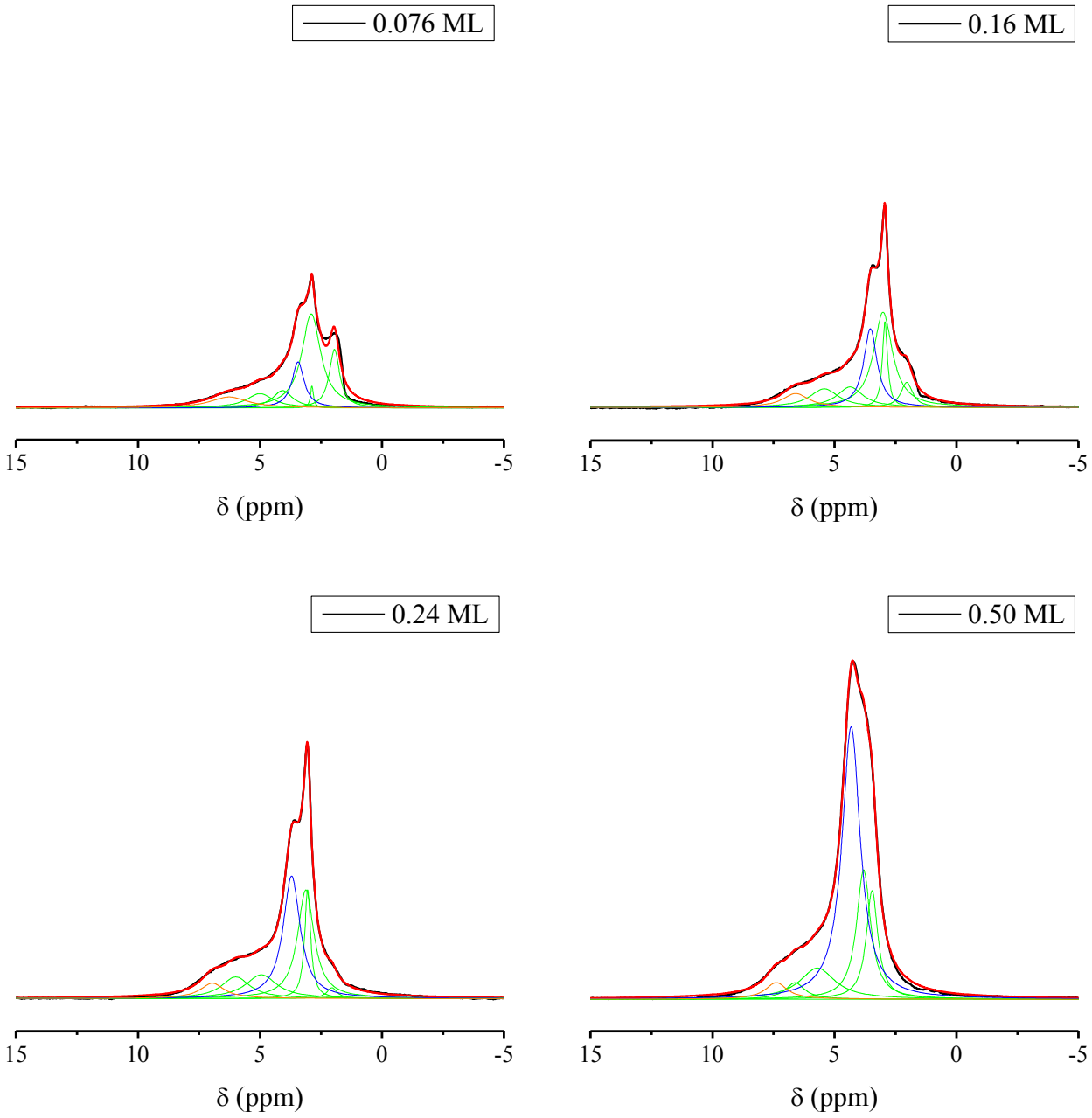

Figure 39: Selected, representative ^{1}H MAS NMR spectra of reduced Pd-MCM-41. The hydration level of each spectrum is noted next to its graph. Each graph shows the original data (black), the calculated model (red) and the individual peaks (green – groups found in pristine MCM-41, blue – Pd Water Group 1, orange – Pd Water Group 2) that the model is composed of. The same vertical scale is used in each graph.

A)

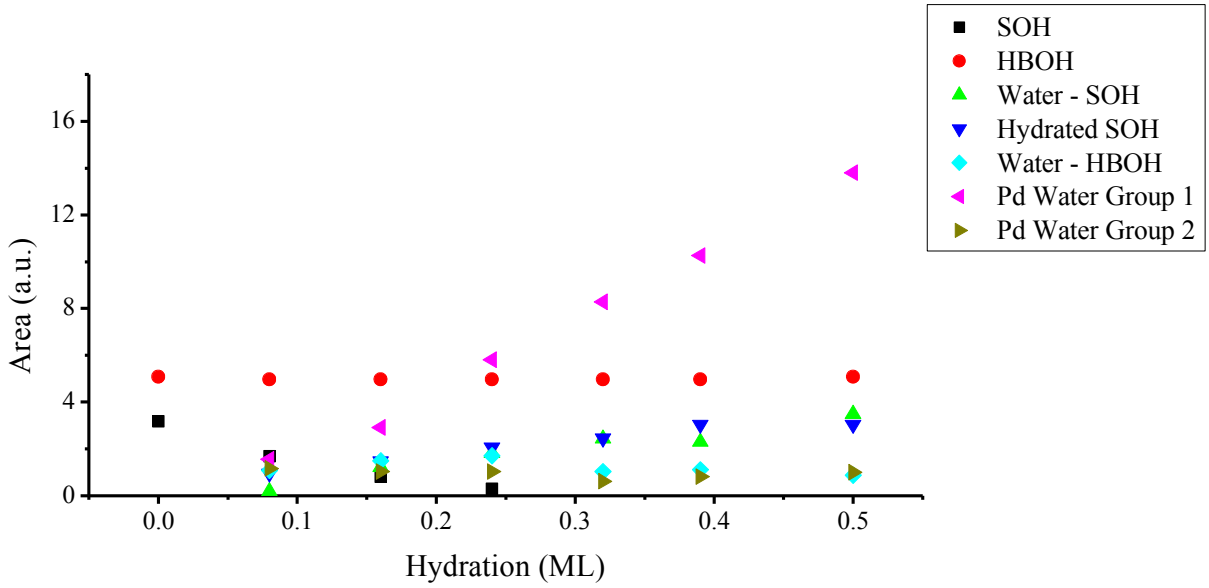

B)

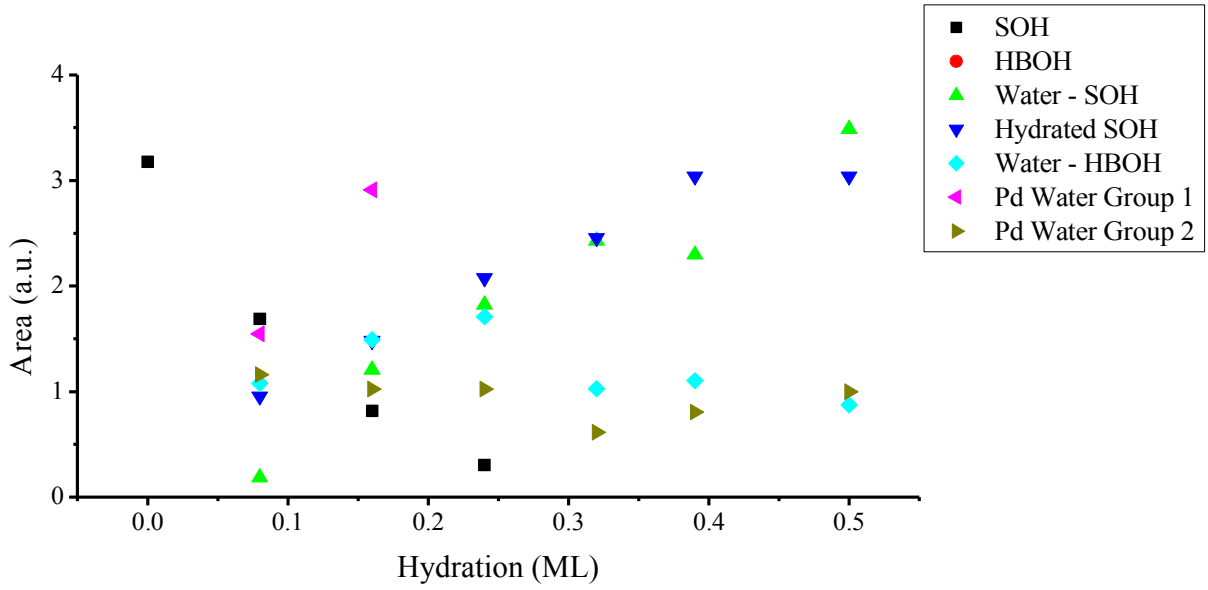

Figure 40: (A) Plots of the peak areas for reduced Pd-MCM-41. (B) The same plot as (A) but with a reduced vertical scale in order to show the details of the smaller peak areas.

A)

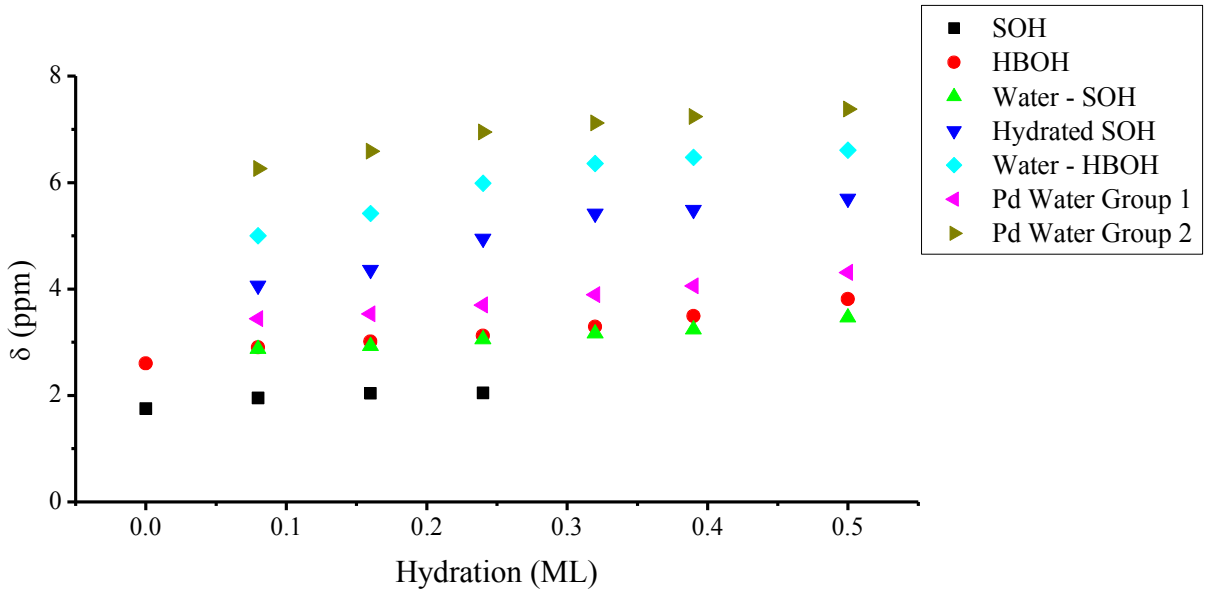

B)

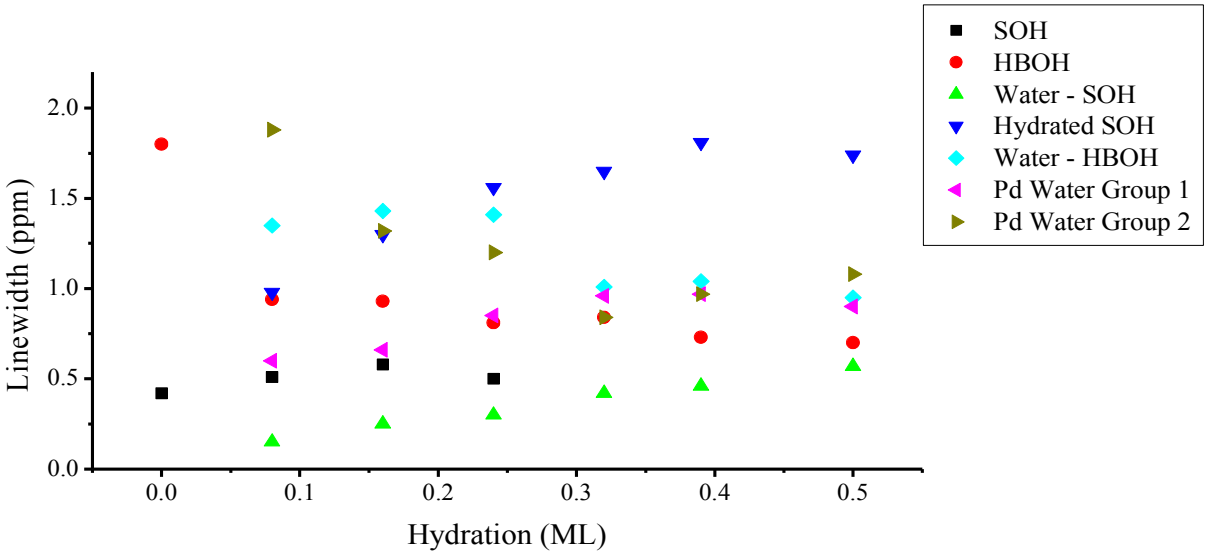

Figure 41: Plots of the chemical shift, δ (A) and linewidth (B) for reduced Pd-MCM-41.

7. Discussion

7.1. Sample Characterization

7.1.1. Pristine MCM-41

The pristine MCM-41 sample was included essentially as a control; a benchmark for comparison to see the effect of the Pd clusters. There are many results in the literature for characterization of this type of MCM-41 [19 – 21, 28 – 30, 73] that the present results can be compared to in order to judge the quality of the material.

The BET isotherm in Figure 22 exhibits a Type IV character, as expected for mesoporous materials [75] and as seen previously for MCM-41 [73]. The specific surface area (SSA) calculated from the partial isotherm in Figure 21 and presented in Table 1, is an appropriate value for well-formed MCM-41 [19 – 21, 28 – 30, 73]. The pore size distribution in Figure 23 exhibits a single, narrow peak at a pore radius of about 1.1 nm (d_{pore} of 2.2 nm), falling within the limits of a mesoporous material and comparable to other preparations of MCM-41 [73, 87, 91]. These results point to a sample containing a large number of nearly identical pores, as expected.

Figure 24 shows the measured XRD diffractogram for the sample used, which is essentially identical to that of previous work, seen in Figure 14 [73]. The distribution of peaks indicate a hexagonal arrangement of pores, while their sharpness points to this pore structure existing over the majority of any one crystallite. The values of d_{pore} and d_{wall} shown in Table 2 are well within the range of previously reported values [73, 87, 91]. The discrepancy in d_{pore} between the XRD and adsorption measurements has been seen in other studies [73]. The latter technique has been shown to underestimate d_{pore}, leading to the development of the former, which is more accurate [91]. The adsorption results are included here to determine the SSA and to show the distribution of pore sizes,

rather than as an accurate measurement of d_{pore}.

Finally, the TEM image in Figure 25 further confirms that the MCM-41 material is well-formed. The mottled pattern visible in the image is a result of the hexagonal arrangement of pores [87].

All of the above characterization measurements for the pristine sample were as expected, indicating that the sample is indeed well formed MCM-41, making it an ideal control for the remaining experiments.

7.1.2. Pd-MCM-41

Similar to the case of pristine MCM-41, there is a wealth of research regarding modified MCM-41, including metal-loaded MCM-41 [25, 26, 38 – 44], again providing reasonable benchmarks and comparisons for the sample used in the current study.

The BET isotherm for Pd-MCM-41, shown alongside the pristine MCM-41 results in Figure 22, exhibits a type IV character. Though the absolute magnitude of the isotherm is less than that for pristine MCM-41, there are still the distinct features required for the type IV determination: monolayer adsorption, capillary condensation and saturation. The reduced quantity of adsorbed gas, which is also shown in the more detailed measurement of the linear portion of the isotherm in Figure 21, is a reflection of the material's lower SSA as compared to the pristine MCM-41 (see Table 1).

It is common for a mesoporous material that has been loaded with metal particles or other molecules to exhibit a reduced SSA as compared to the unmodified material [43, 44, 83, 87, 92 – 94]. Blocking of the pores by an accumulation of added material is often cited as the cause for the loss of surface area in the resulting loaded sample [43, 87, 92], but this does not seem likely, at least for the present case.

A blockage in the context of adsorption-based surface area determinations means a boundary that an adsorbate molecule or atom cannot pass. In the case of the Pd-MCM-41 sample, this pore blocking idea means that a metal cluster has clogged the pore so that a nitrogen molecule cannot pass. The Van der Waals radii of gaseous, molecular nitrogen are 1.70 Å in the direction of the N-N bond and 1.95 Å in the direction perpendicular to this [95]. Water is larger, possessing an average Van der Waals radius of 2.82 Å [96] (molecular models find radii from 3.0 [97] – 3.6 Å [98]). It stands to reason then that if nitrogen molecules are unable to reach parts of the sample's pores because of a blockage, then water molecules wouldn't be able to either, since they are larger. But Figure 37 shows that at a hydration of around 0.3 ML, all of the SOH groups on the Pd-MCM-41 surface have been hydrated. Comparing the SSA of the Pd-MCM-41 (SSA = 582 m^2/g) to that of the pristine MCM-41 used as a precursor in its synthesis (SSA = 874 m^2/g [99]) shows a loss of one third of the surface area. This means that at least one third of the pore volume (as opposed to one third of the total number of pores, since the length of an individual pore would vary) would have to be blocked in this manner. If water molecules were unable to reach these surfaces, then the SOH peak should remain at one third of its maximum area regardless of hydration level.

It could be argued that perhaps there are no hydroxyl groups in these blocked off regions of pore surface, especially since the pristine MCM-41 used as the precursor to the Pd-MCM-41 is dehydroxylated to start with, having been calcined at 923 K as its final synthesis step. There are, however, several steps in the synthesis procedure of the metal loaded sample that occur in solution, when introducing new molecules or rinsing the sample. The rate constant for rehydroxylation (ie. the time required for the sample to replenish 63% of its hydroxyl groups) has been estimated to be 17 hours [90]. Even if a reasonable approximation of two to three hours is used to estimate the contact time between the material and water, there should still be 10 – 15 % of the surface's hydroxyl groups

(in reality it is likely more, since the hydroxyl group signal of as-synthesized Pd-MCM-41 is higher than this). If one third of the surface remains unhydrated, 3 – 5 % of the SOH peak should remain. We can ignore the fact that, in a fully hydroxylated sample, only 33 % of the hydroxyl groups are SOH type, since the HBOH groups are formed only after the SOH groups. Since the SOH peak is found in a region of the NMR spectrum that is unoccupied by any other species, any residual SOH groups would be readily identifiable. Therefore, based on the lack of signal from SOH groups at higher hydration levels in Pd-MCM-41, the theory of pore-blocking as the cause of the drop in SSA in this sample is unlikely.

An alternate explanation is that the material has been degraded during the synthesis process. The stability of MCM-41 is a debated topic, with many contradictory results being presented in the literature. One report shows MCM-41 degrading in ambient conditions after a period of three months [100], while another shows repeated saturation with water vapor is sufficient [101]). Others have found the pore structure and surface area to be very tolerant over these extended time periods [90, 102]. MCM-41 has been shown to be particularly susceptible to basic environments [103]. One case of Pd incorporation, using the same Pd source as the present study, cited pore collapse as the cause for their significant loss of surface area [83]. Since the stability of MCM-41 is questionable, and a similar Pd incorporation attempt led to collapsed pores, degradation of the material is a plausible explanation for the observed drop in SSA.

Similar to the adsorption results, the XRD diffractogram of Pd-MCM-41 differs from that of pristine MCM-41, both shown in Figure 24. The main peak is shifted to higher Bragg detection angle, while the peaks attributed to reflections from other crystal planes appear to be broadened. These effects can be attributed to a loss of regularity in the material's pore structure (ie. degradation), scattering caused by the introduction of the metal or a loss of scattering contrast between the material's

silica wall and the pore channel. The latter of these was explored by Marler et. al. [71], who adsorbed nine organic sorbates into the mesopores of MCM-41. It was found that as the difference between the electron density, ε, of the pore wall and the sorbates decreased, the intensity of the XRD peaks decreased and were broadened. The pore wall was calculated to have an ε of 665 e / 1000 $Å^3$. The sorbates' ε varied from 217 to 852 e / 1000 $Å^3$. Using their same formula, the ε of Pd is 3130 e / 1000 $Å^3$. The sharpest XRD peaks in Marler's study were found when the pores were empty, as this yielded the largest ε difference. Adding a substance with as large a ε as Pd will only increase the contrast with the pore wall, and so this mechanism cannot be the cause of the broadening seen in the current results.

X-ray scattering caused by the introduction of a strong, metallic scattering agent is also not the likely cause of the broadening. Mokhonoana et. al. [39] introduced Fe into MCM-41 and required 8.8 % Fe by weight before broadening developed that was similar to what the current results show. The x-ray cross section (in cm^2/g) of Fe is 1.4 times higher than that of Pd at the wavelengths being considered [104] (Cu Kα x-rays are used both by Mokhonoana and in the present study). Therefore, 8.8 % Fe by weight has the same scattering power as 12.5 % Pd, six times more than what is present in the current sample. Reversing this calculation, the 2.0 % Pd by weight present in the current sample translates into about 1.4 % Fe by weight in Mokhonoana's study. At the 2 % Fe loading in that study, there is almost no discernible difference in the XRD diffractogram, as compared to the pristine case.

In another study [38], it was shown that the decrease in SSA and intensity of XRD spectrum in Co loaded MCM-41 was not likely due to the metal itself. In this publication, Khodakov et. al. performed the metal impregnation procedure on their MCM-41, but without the Co source, finding that introducing this slightly acidic solution to the pore volume produced similar detrimental results to the MCM-41 structure. Therefore, in the present sample, the presence of the Pd metal itself is deemed to not be the cause of the broadening in the XRD results, leaving material degradation as the most likely

cause of the observations, just as it was for the N_2 adsorption results.

The shift in position of the peak due to the (100) reflection in the Pd-MCM-41 XRD diffractogram, as compared to the pristine MCM-41 sample, is the cause of the differences between the two samples in all of the other parameters in Table 2. Either the presence of the Pd clusters or the Pd impregnation procedure itself has caused a decrease in the measured cell parameter of the material. One explanation is that the Pd introduction procedure has caused a contraction of the pore structure, similar to what is observed when pristine MCM-41 is calcined to remove the surfactant template [69, 70, 73]. Alternatively, the shift of the (100) reflection might be related to the deposition of material on the pore walls, either Pd metal or SiO_2 that dissolved from other parts of the material during the metal impregnation procedure.

The final results that provide information on the state of the Pd-MCM-41 material are the SEM (Figure 26) and TEM (Figure 27) images. These images show details of samples that were prepared using the same synthesis procedures as those in the present study. These samples exhibit decreased SSA and broader XRD peaks as compared to pristine MCM-41, similar to the results of the present samples [87].

A repeating pattern of light and dark lines is visible in certain areas of the TEM image in Figure 27. This can be be attributed to the pore channels viewed lengthwise. The periodicity of these lines is 3.6 nm; similar to the lattice parameter in Table 2. A direct comparison to the current samples is not appropriate, since these images are not of the same material. They are included to show the success of the synthesis procedure in creating well formed MCM-41. There is, however, a distortion of some kind, likely due to resolution constraints. This is deduced from the fact that the light and dark lines are equal in width. If this is an accurate image of the pore walls (dark lines) and pore channels (light lines), then this would mean that they are equal in thickness, each about 1.8 nm across. This cannot be

the case since the XRD results both above, and from the original report that these images are obtained from [87], indicate otherwise. Therefore, this pattern will be interpreted as indicating that the pores, at least those seen in this particular image, are well formed and not collapsed. This does not eliminate pore collapse, or material degradation of any other kind, as a possible explanation for the aforementioned XRD and gas adsorption results. It simply means that there are definitely regions that have maintained their structure, which explains why the SSA is as high as it is and why there are still details in the XRD and N_2 adsorption results that indicate the material is a MCM-41 type material.

The other piece of information these electron microscopy images provide is that there are definitely Pd particles in the sample. Pd clusters are clearly visible in the SEM image (Figure 26) that that have diameters from 8 to 30 nm. Due to the nature of the technique, these clusters must be located on the surface of the MCM-41 particle. Due to the image's limited resolution, this is the extent of the conclusions that can be made from it. There are hints in the image, highlighted by the dashed circle in Figure 26, that there could be smaller particles shown, but the small white dots could just as easily be noise. Similarly, in the TEM image (Figure 27), there are large dark areas that are identified as Pd metal clusters, roughly 25 nm in diameter. Due to the penetrating nature of the technique, the Pd cannot be definitively located as being inside or on the surface of the MCM-41 particle. It also cannot be concluded that there are not Pd clusters smaller than the resolution limit of the image. Furthermore, as mentioned previously, these images are representative and not an extensive survey of the electron microscopy results for the current samples. They are intended to show the presence of Pd in the samples and provide some information on the details of these metal clusters. Therefore, while it is certain that Pd has been successfully introduced into the samples, it cannot be conclusively stated that there are or are not Pd particles present that are small enough to reside inside the pores themselves.

7.1.3. Reduced Pd-MCM-41

It is assumed that the reduced Pd-MCM-41 sample's structure is identical to that of the Pd-MCM-41 sample, since the only difference between the two is a treatment with H_2 gas. This assumption is supported by the SSA and selected N_2 adsorption isotherm of reduced Pd-MCM-41, shown in Table 1 and Figure 21, respectively, being essentially identical to that of Pd-MCM-41. The only noticeable difference in terms of sample characterization is a change in color. Pd-MCM-41 is a light brown powder, while the reduced sample changed to a dark gray upon exposure to H_2 gas, verifying that a chemical reaction, undoubtedly reduction of PdO to Pd metal, has taken place.

7.2. Dry Samples

The NMR spectra of the three main samples studied (pristine, Pd- and reduced Pd-MCM-41) in a dry state are nearly identical, as can be seen in Figure 28. Qualitatively, the spectra of the two Pd loaded samples are essentially indistinguishable. Quantitatively, the hydroxyl (OH) density and relative OH populations, shown in Table 3, vary by less than 1%. This result is expected, since both Pd loaded samples are taken from the same synthesis batch. The only difference between them, as mentioned previously, is that the reduced sample received a treatment in H_2 gas. What this result shows is that this H_2 treatment did not have any effect on the OH groups. This provides further confirmation that it was correct to assume that the physical structure of the two Pd loaded samples are identical.

There is a slight discrepancy in the OH density between the pristine and Pd loaded samples; the former is 10 % lower than the latter. The relative OH populations differ as well. For every 100 OH groups, the pristine MCM-41 has 3 fewer SOH group than the Pd loaded samples, and concomitantly, 3 more HBOH groups. These differences can be explained by the fact that the pristine MCM-41 used in this study is not the same material used in synthesizing the Pd loaded samples; they come from

different batches. Considering the fact that all of the MCM-41 samples are synthesized in the laboratory, rather than in a more controlled commercial setting, small variations are to be expected. Despite the differences between the two types of samples, both the density and relative populations of OH groups of all samples studied fall within the reported range for MCM-41 [21, 28, 29].

The chemical shifts for the unhydrated SOH group range in value from 1.72 to 1.77 ppm across the six dry samples (each sample was measured twice in the dry state), while those for the HBOH group are from 2.49 to 2.60 ppm. These are in good agreement with the previously reported values of 1.70 – 1.85 ppm for SOH and 2.6 – 3.6 ppm for HBOH [21, 28].

The dry NH_4-MCM-41 sample, whose NMR spectrum is shown in Figure 30, exhibits an additional peak at 7 ppm, as mentioned in the Results section. The chemical shift of this peak matches well with results in the literature for the introduction of NH_4 by ion exchange on the pore surfaces of zeolites [105, 106] and MCM-41 [107]. Therefore, the observed peak is identified as NH_4 groups on the pore surface of MCM-41.

7.3. Hydration Study – Quality of Fitting

7.3.1. Pristine MCM-41

The results of the hydration study for the pristine MCM-41 sample is essentially an exercise in applying the Walia model [21] to the sample under study. This model was originally developed for a commercially prepared MCM-41 over the hydration range of 0.0 to 0.2 ML. The samples in this report are prepared in a laboratory setting and the hydration levels studied include 0.0 to 0.5 ML. Therefore the pristine MCM-41 sample is included as a control for this study, verifying the validity and applicability of the model to the laboratory-prepared samples in this report, as well as the viability in extending the model beyond the 0.2 hydration level. Comparisons will be made – between the results presented here and those in the original presentation of the Walia model – throughout the discussion of

this sample in order to assess these points. By comparing the results of each study, it will be shown that the Walia model has been successfully applied to the present pristine MCM-41 sample, making it a viable control sample that can be used as a benchmark for studying the effect of Pd metal in the other samples.

The trends in plots of peak areas, shown in Figure 32, are fairly smooth with limited scatter. In nearly each case, the behavior of a peak's area matches that predicted by the Walia model. The HBOH group's area remains constant throughout the entire hydration range, since it is fixed. The peak for the unhydrated SOH silanols decreases in area with increasing hydration, while the hydrated SOH peak increases in area. This can be explained by the increasing population of water molecules causing an increased number of SOH groups, on average, whose H atom is hydrogen-bonded to the O of a water. This bond shifts the δ of that H downfield from its unhydrated position, so it contributes to the area of the hydrated SOH peak. Between 0.15 and 0.20 ML, the SOH peak area reaches zero. This is the hydration level where the model predicts that there is a sufficient number of water molecules for all the H atoms in SOH groups to be hydrogen-bonded to an O of water. Converting the peak areas into a H atom count, it is found that in the 0.19 ML sample, there are 2.81×10^{19} water molecules in the SOH water peak, while in the dry spectrum there are 2.99×10^{19} silanol groups in the unhydrated SOH peak. This confirms the above prediction. As such, nearly all of the SOH groups should appear at the shifted, hydrated position. Accordingly, the hydrated SOH peak's area reaches its maximum, at a slightly later hydration level, at a value near the maximum area of the SOH peak, as expected.

The area of both water peaks, for water molecules associated with the SOH and HBOH groups, increase with increasing hydration, as expected. Up until a hydration level of 0.2 ML, the ratio between these areas is between 1.5 and 2 SOH water for every one HBOH water. This ratio is predicted by the Walia model and is explained by the different number of sites available for water to

hydrogen bond to each type of surface silanol. A SOH silanol is capable of participating in three hydrogen bonds: one at its H atom and two its O, one for each lone electron pair. Therefore, SOH groups have three available sites. But the H in HBOH groups are already, by definition, involved in a hydrogen bond. Also, in order for the populations of SOH and HBOH groups observed in the dry spectrum to be produced, the HBOH groups are expected to exist in chains [21]. This leaves only one lone electron pair on their O atoms, and thus only one available hydrogen bonding site per group. The population distribution is approximately three HBOH groups for every two SOH. Therefore, in total, there are two sites for water to bond to SOH groups for every one on HBOH groups.

The predicted ratio between water groups does not persist in the results above the 0.2 ML hydration level. After this point, the SOH water area grows faster than the HBOH water. This is not an unexpected development; the Walia model was intended for application up to a hydration level of 0.2 ML. Part of the reason for this is that 0.2 ML is roughly the point where there is one water molecule for each surface silanol group. This means that any additional water cannot occupy a surface site and therefore will interact with other water molecules; these water molecules will be referred to as non-surface water. It is likely that water-water interactions begin to develop before this point, but are sufficiently small to be neglected for the most part. This might, however, explain why the hydrated SOH peak appears to reach a maximum at a slightly higher hydration level than where the unhydrated SOH peak disappears.

The increased area ratio of the SOH water peak to the HBOH water peak that develops at hydration levels above 0.2 ML suggests that the non-surface water molecules have a similar chemical shift to the SOH water. Specifically, these additional water molecules are binding to surface-bound water with only single hydrogen bonds. If they were binding via two hydrogen bonds, either by binding to two separate surface waters or a water and surface O atom, then the area of the HBOH water

peak would increase its area, since these water molecules are mostly involved in two hydrogen bonds. While there are no doubt sites available for these non-surface water molecules to form two hydrogen bonds, it is reasonable to assume that there are simply more available where only one bond is possible or favorable.

The appearance of an additional peak at 0.51 ML is another feature of the higher hydration levels that must be explained with an extension of the Walia model. Grunberg et. al. [30] observed an additional peak in their MCM-41 at 0.61 ML which was not present in their previous sample at 0.15 ML. At 0.61 ML it already constituted about 75 % of the total spectral area. Grunberg identified the peak as pore-filling water. They argued that since both surface water and pore-filling water were present in the same spectra, the pore-filling mechanism was such that once the surface hydration sites were saturated, water would condense spontaneously over the entire pore radius in a few locations. These regions of water-filled pore grow axially with increasing hydration. Figure 42 is reproduced from Grunberg's publication and describes this filling mechanism. It also shows the converse situation in SBA-15, where subsequent layers build upon the first surface layer, growing towards the pore center, each successive layer only beginning once the previous is filled. The cause for two different mechanisms is the difference in pore diameter; SBA-15 is assumed to have too large of a pore diameter for the condensation that is seen in MCM-41 to occur. In the current study, the additional peak that appears at 0.51 ML is attributed to pore-filling water.

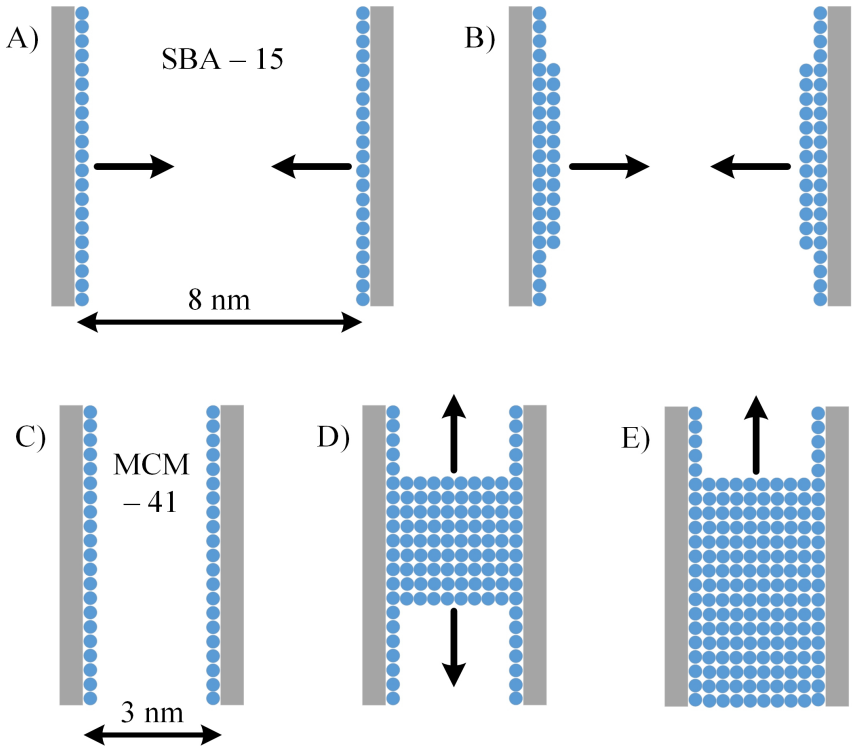

Figure 42: Pore filling mechanisms for small and large diameter pores, as proposed by Grunberg [30]. For materials with larger pore diameters, such as SBA-15, water is initially adsorbed into a monolayer (A). Multilayers start to form with the addition of more water (B); water layers grow radially towards to the pore center. In the small pore diameters of MCM-41, after the monolayer has formed (C), capillary condensation occurs, filling the pore across its entire diameter (D). Additional water in this case causes these water-filled regions of the pore to grow axially (E). Taken from reference [30].

In addition to the hydration level at which the additional peak appears, and the spontaneous nature in which it does so, its chemical shift also helps to identify it as the pore-filling water seen by Grunberg. As seen in Figure 33A, the chemical shift of this water peak is 4.6 ppm, which is nearly identical to the 4.7 ppm reported by Grunberg. Therefore, this additional peak can be conclusively identified as pore-filling water.

For the remaining peaks, the trend in chemical shift (Figure 33A) is to increase with increasing hydration. None of the shifts change by more than 1.6 ppm across the entire hydration range studied. A more concise assessment of how successfully the Walia model has been applied to the current pristine MCM-41 sample is found in Figures 43 and 44. In these plots, the chemical shifts of each of

the five peaks in the fitting model are plotted. The results for both the current experiments as well as those from the paper by Walia are plotted on the same graph to show how well they compare.

In general, Figures 43 and 44 show that the peaks comprising the NMR spectra for the pristine MCM-41 in the current study are found in similar shift positions as those from the Walia study; the two data sets have comparable absolute values of shift and follow identical trends with increasing hydration. The chemical shifts of the SOH and HBOH groups are intrinsic to their nature, while the other three groups (hydrated SOH, SOH water and HBOH water) are explained by the averaging of the various hydrogen bonding configurations (Figure 19) for each group, as outlined in equations (62) – (64).

The chemical shifts of the unhydrated SOH, HBOH and hydrated SOH groups are nearly identical in both data sets, falling within 0.1 – 0.2 ppm of each other for the hydration levels that coincide between the two sets of experiments (0.0 – 0.2 ML). The SOH water is off slightly more, 0.2 – 0.3 ppm lower than Walia's results. The HBOH water peak differs the most between the two sets of results. At the lowest hydration, the current results are 0.9 ppm lower than Walia's, but this discrepancy decreases at higher hydration levels.

The trends in chemical shift at hydration levels above 0.2 ML, which is the limit of Walia's results, are essentially unchanged compared to those below 0.2 ML; the trend of increasing chemical shift with increasing hydration continues. The same arguments that explain this trend below the 0.2 ML hydration level can be used above it as well. The two main explanations originally provided by Walia were an increased strength of hydrogen bonds and a higher occupation probability of molecular configurations (Figure 19) that result in higher average chemical shifts for the protons concerned. For the case of the SOH water, which has already been discussed above, any change in shift is still likely associated with shifting occupation probabilities, though not involving any of the configurations in

Figure 19, but those involving water-water interactions instead.

Most of the discrepancies in chemical shift between the present work and the results presented by Walia are small (< 5 – 10%), while one is larger (~ 15 %). Even without a cause, it could be argued that these differences are small enough to conclude that the Walia model has been successfully applied to the sample and can therefore be used to interpret the behavior of water in laboratory-prepared MCM-41. There is, however, a likely explanation for the differences seen, which is that the widths of the spectra observed in the present study are much narrower than those seen by Walia. This could have an effect on where the minimization fitting routine identifies the center of a peak to be, contributing to the discrepancies. Another possibility is that the differences in width are in fact connected to these small differences in chemical shift.

The plot of linewidths (Figure 33B) have more complex behavior than that of the chemical shifts. The widths of the SOH groups, SOH water and HBOH water are essentially constant across all hydration levels, with SOH water showing a slight trend to increase with hydration. The other peaks show a bimodal behavior, with the transition between the two occurring around 0.20 ML. The HBOH width changes the most, decreasing from 1.7 ppm in the dry sample, to about 0.5 ppm at around 0.25 ML, where is remains for the higher hydration levels. Finally, the width of the hydrated SOH peak is roughly constant or slowly increasing around 1 ppm, then increases quickly to about 1.8 ppm between 0.15 and 0.25 ML, where it remains until 0.50 ML.

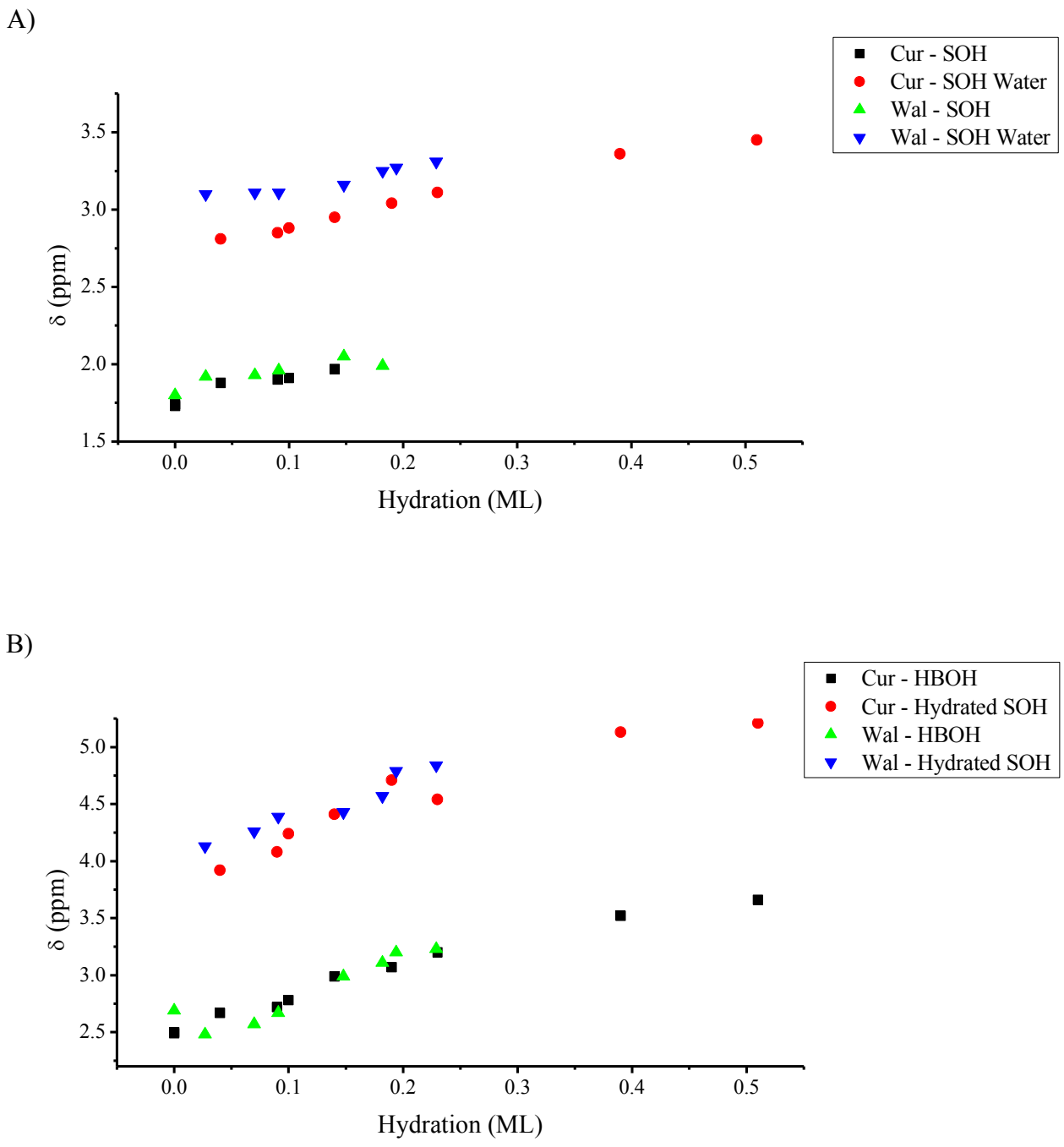

Figure 43: Chemical shift comparison of the unhydrated SOH peak (A), SOH water peak (A), HBOH peak (B) and hydrated SOH peak (B) between the current (Cur) results and those of Walia (Wal).

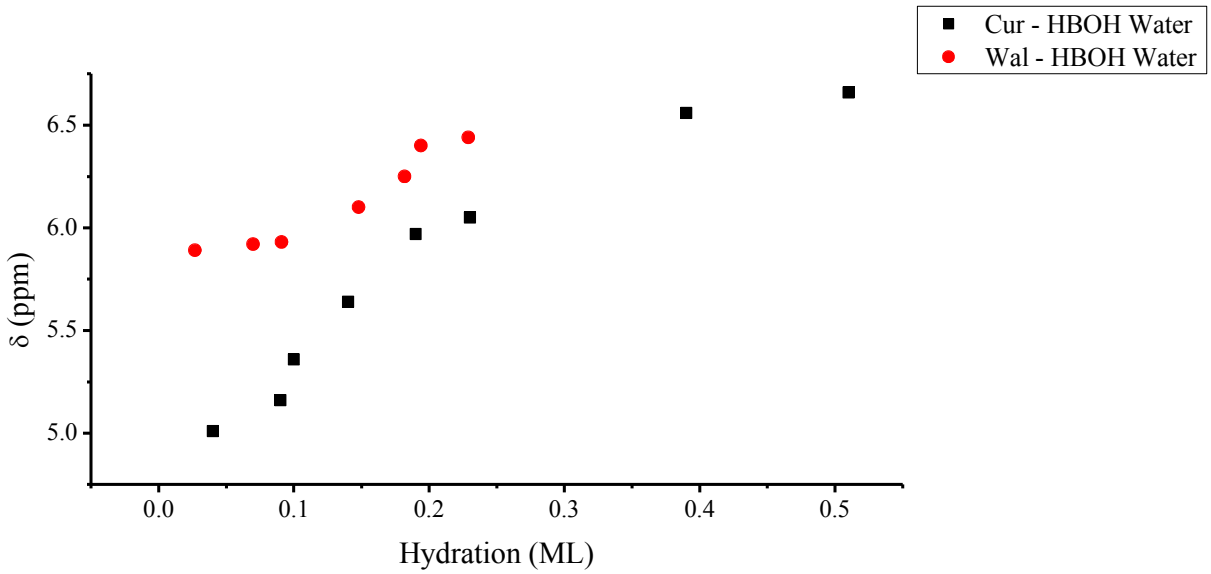

Figure 44: Chemical shift comparison of the HBOH water peak between the current (Cur) results and those of Walia (Wal).

As is the case for chemical shift, comparison of the peak widths in the current results to those of Walia are most compactly presented graphically, which are shown in Figures 45 and 46. The linewidths of the unhydrated SOH group are identical for both data sets. Those of the HBOH and hydrated SOH groups show similar trends, but dissimilar values; Walia's results are consistently larger by as much as 0.8 ppm. The width of the HBOH water peak is similarly wider in Walia's results for hydration levels up to 0.15 ML, then begin to narrow, approaching the essentially constant width seen in the current results. The width of the SOH water differs in both value and trend between the two data sets. The current results show the peak width to begin fairly narrow (0.20 ppm), stay constant until about 0.2 ML, and then slowly increase with hydration. Walia's results show the SOH water starting much wider (1.15 ppm) and decrease rapidly with hydration, again approaching a value similar to that of the current results.

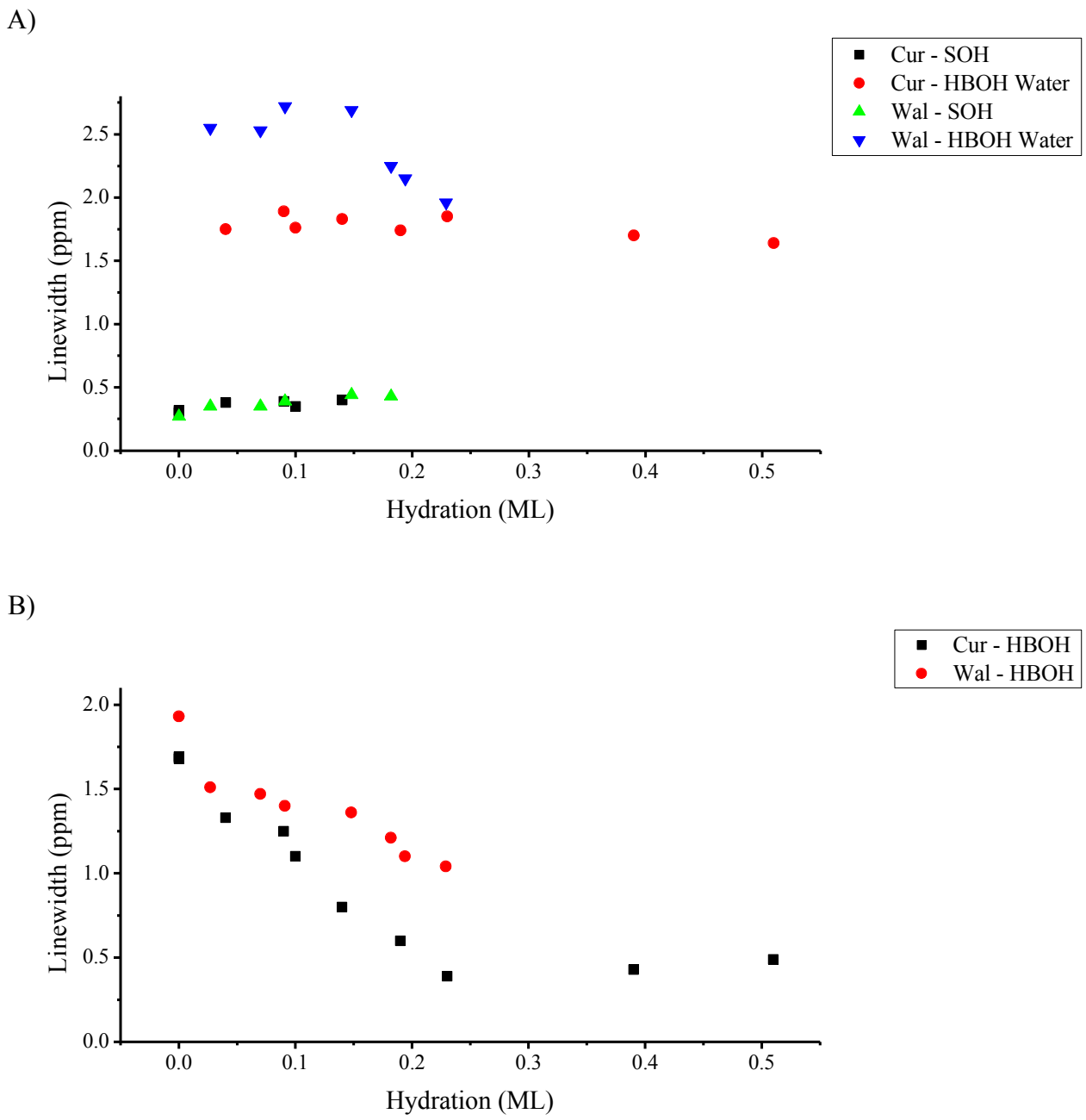

Figure 45: Comparison of the width of the unhydrated SOH peak (A), HBOH water peak (A) and HBOH peak (B) between the current (Cur) results and those of Walia (Wal).

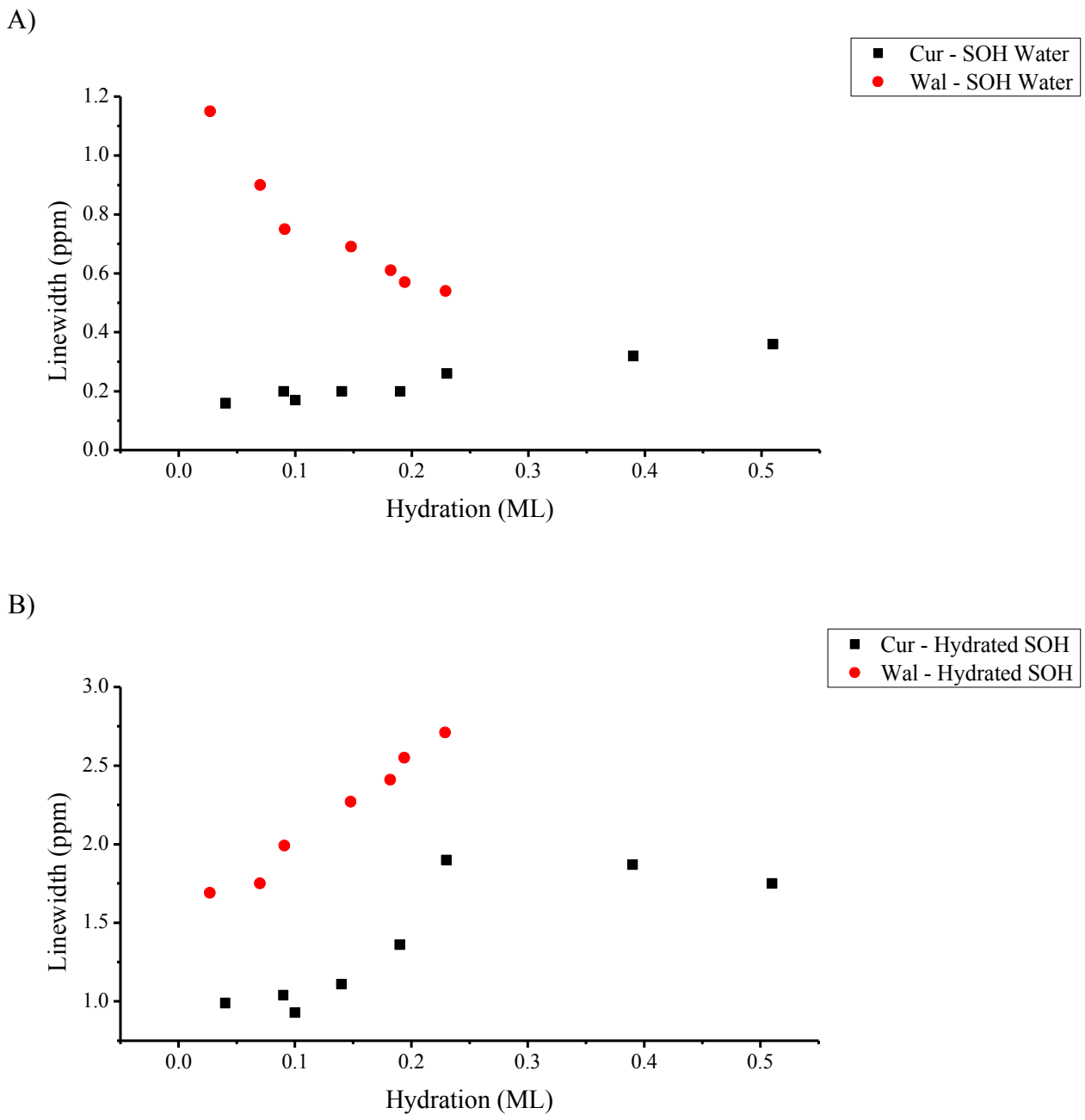

Figure 46: Comparison of the width of the SOH water peak (A) and hydrated SOH peak (B) between the current (Cur) results and those of Walia (Wal).

It is important to note that the overall smaller widths found in the current study compared to those of Walia are not artifacts of a poorly applied or otherwise inadequate fitting model. The spectra simply have very different widths, as demonstrated in Figure 47. This graph compares the NMR spectra of two pristine MCM-41 samples of similar hydration level. The only difference is that one (shown in black) is from the current study, which is prepared in a laboratory setting, while the other (shown in red) is a commercially prepared MCM-41 from Sigma-Aldrich, the same material used in Walia's study. It is obvious that the peaks comprising the spectrum of the commercial sample are wider. Based on the sample characterization performed, which consisted of all the standard methods used in the literature (XRD, gas adsorption and TEM), the samples used in both the current study and in Walia's are definitely MCM-41. The widths of the peaks in the dry samples (ie. widths of SOH and HBOH at 0.0 ML) are essentially identical. The discrepancies develop when water is present. Since XRD, gas adsorption and TEM measurements cannot detect a difference, the only factor separating these two materials is their means of synthesis, which could perhaps lead to some physical discrepancy (or discrepancies) between them. What these physical differences are that could cause the different widths in the measured NMR peaks are beyond the present understanding of MCM-41 that exists in the literature and is the topic of ongoing investigation. The results here, however, will permit some preliminary hypotheses, contingent on a way to connect the widths with physical phenomenon.

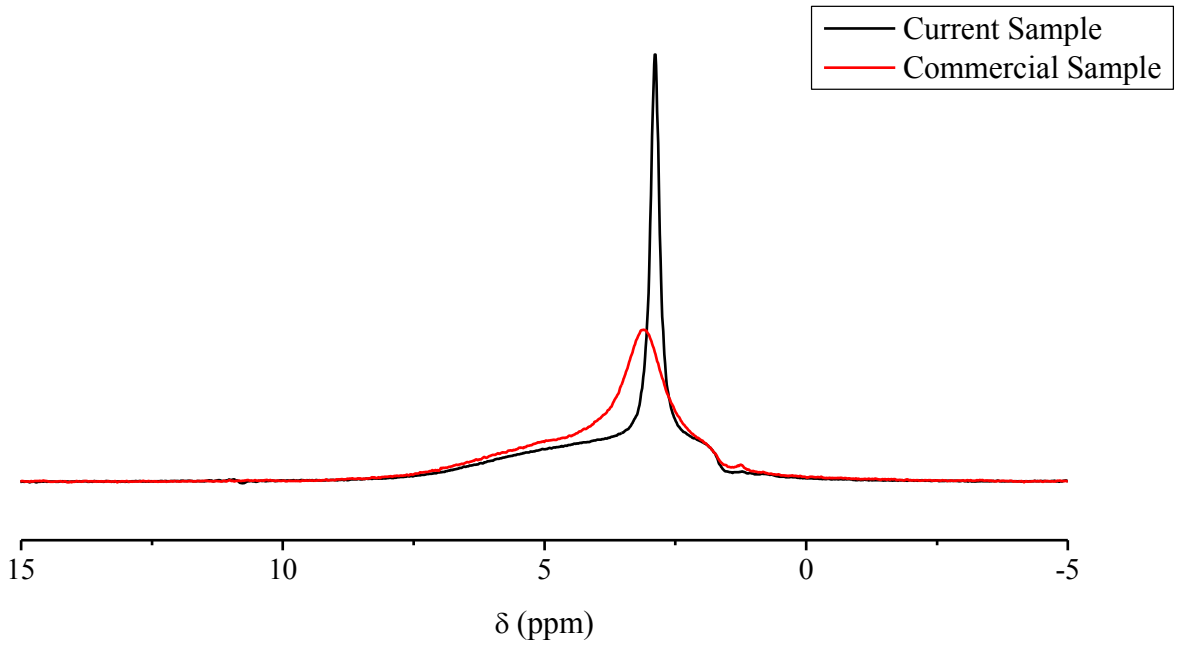

Figure 47: Spectral comparison of the current, pristine MCM-41 (black) to a commercially synthesized sample (red). Both samples are hydrated to 0.1 ML.

Under static conditions, the width of a NMR signal from a solid sample like MCM-41 will be largely due to dipolar interactions. The chemical shift distribution also plays a role. That is, the width of the NMR peak for a particular group is influenced by how large the range of magnetic environments, and thus chemical shifts, the protons of that group are experiencing. When the sample is undergoing MAS, the dipolar effect is assumed to be removed by this spinning. One study [28], however, has found that the motion of water molecules in hydrated MCM-41 has components both faster and slower than 4 kHz. Therefore, in both the current study and in Walia's, a part of the dipolar interaction contributing to the linewidth may be averaged out by 10 kHz MAS and a part by molecular motion. This leaves chemical shift distribution as a significant line broadening agent.

It is important to note that Walia concluded that linewidth was the least well defined of the three peak parameters, limiting the certainty of any rigorous interpretation of them. With this and the above

points in mind, a possible interpretation for the overall wider nature of Walia's results is that the pore surface of the commercially prepared MCM-41 used in that study is more amorphous than the material prepared in the laboratory. The wider peaks, if interpreted as being mostly due to a larger chemical shift distribution, are suggesting that the water and silanol groups are in more varied environments. This could be due to a surface that has a more random distribution of silanol groups, resulting in less regular arrangements of water-silanol associations. More specifically, the wider peaks suggest that more of the bonding configurations shown in Figure 19 are being accessed. This would lead to the population distribution of these configurations differing between Walia's sample and that of the current study. Not only would this affect the chemical shift distribution, but also the average chemical shift, since, according to equations (62) – (64), each bonding configuration contributes to the average chemical shift differently. This could explain some of the chemical shift discrepancies mentioned previously.

It is the width of water peaks that differ the most between the current results and those of Walia. Walia concludes [21] that as more water is added to his sample, more water molecules assume fewer bonding configurations, perhaps just one even, since the width of both water peaks decrease with increasing hydration. Conversely, in the present results, the widths of the water peaks stay essentially constant. The SOH water peak increases in width at hydration levels above 0.2 ML, but this can be attributed to the water molecules involved in water-water interactions contributing to this peak.

It is difficult to attribute any meaningful interpretation to the width of the pore-filling water, since its area is so small and it is only present at the highest hydration level. The fact that it is narrow is reasonable though, since the water in this group is in a very liquid-like environment. The narrowness in this case would then have less to do with a narrow chemical shift range, and more with motional averaging of the dipolar interactions at rates above the MAS spinning rate.

To comment briefly on the actual process of fitting the data using the Walia model, the only difficulty, as was discussed in the Results section, had to do with the width of the peak representing the HBOH group. This issue likely arises because of the discrepancies in width mentioned above. With the individual peaks that comprise the full NMR spectrum being sharper, there is less tolerance for such a precise model. Small issues with the experimental process, such as phasing or baseline subtraction, could distort the data, requiring the measures taken above in order to obtain a proper, physically relevant fitting of the data.

Regardless of the challenges in applying the Walia model to the pristine MCM-41 sample in the current study and the minor discrepancies in results between this and Walia's original results, the model can adequately fit the data. This means that the model can be successfully applied to pristine MCM-41 samples other than the commercially prepared type used in Walia's study. Furthermore, the model can be extended, given certain additional considerations, to hydration levels above the original 0.2 ML it was intended for. Therefore, the pristine MCM-41 results will act as a control data set for the palladized samples in the following section, providing a benchmark for the fitting process and results. In addition, the model can be confidently applied to these palladized samples, allowing that any additional effects will be due to the presence of the Pd clusters they contain.

7.3.2. Pd-MCM-41 and Reduced Pd-MCM-41

The previous section establishes that the Walia model can be applied to MCM-41 samples that are synthesized in a laboratory setting and at hydration levels up to 0.5 ML. These pristine MCM-41 results will now be used to judge the effectiveness of the fitting when applying the Walia model to the palladized MCM-41 samples, with two additional peaks to account for the additional effects of the Pd clusters on the NMR spectrum. There are certain parameters that are not changed by the addition of the metal. A comparison of these parameters in Pd-MCM-41 and reduced Pd-MCM-41 to those in

pristine MCM-41 will demonstrate that a similar quality of fit has been achieved in the palladized samples.

With the self-consistency of the fitting established, any discrepancies between the Pd-containing samples and the pristine sample are deemed to be caused by the presence of the metal. Differences between the results of the Pd-MCM-41 and reduced Pd-MCM-41 are deemed to be caused by the presence of the metal oxide. Interpretation of these differences will provide the basis for a model of how water behaves in Pd-MCM-41, which will be discussed in the next section.

The parameters that provide the best evidence that the model is being applied equally well in each sample are the chemical shifts. The comparisons of chemical shifts for the unhydrated SOH, HBOH, hydrated SOH, SOH water and HBOH water are shown in Figures 48 and 49. It can immediately be seen that these peaks are found at essentially identical chemical shifts in each of the three samples. The shifts of unhydrated SOH fall on a single line with almost no scatter; the values are considered identical. The same is true for SOH water. The HBOH and HBOH water chemical shifts similarly fall on a line, but with more scatter, though there is never more than 0.2 ppm separating corresponding peaks in the three samples. Finally, the greatest difference lies in the chemical shift of the hydrated SOH peak, where at most 0.5 ppm separates corresponding peaks in the three samples. These results indicate that despite the three samples having different features, the model is finding the same peaks in the palladized samples as it did in the pristine case. Furthermore, Figure 49B shows that Pd Water Groups 1 and 2 are being consistently identified at the same chemical shifts in both Pd-MCM-41 and reduced Pd-MCM-41. All of these consistencies are further, encouraging evidence that the model has accurately fit the spectra of each of the three samples. The discussion on the origin of the shifts of Pd Water Groups 1 and 2 are found in the next section.

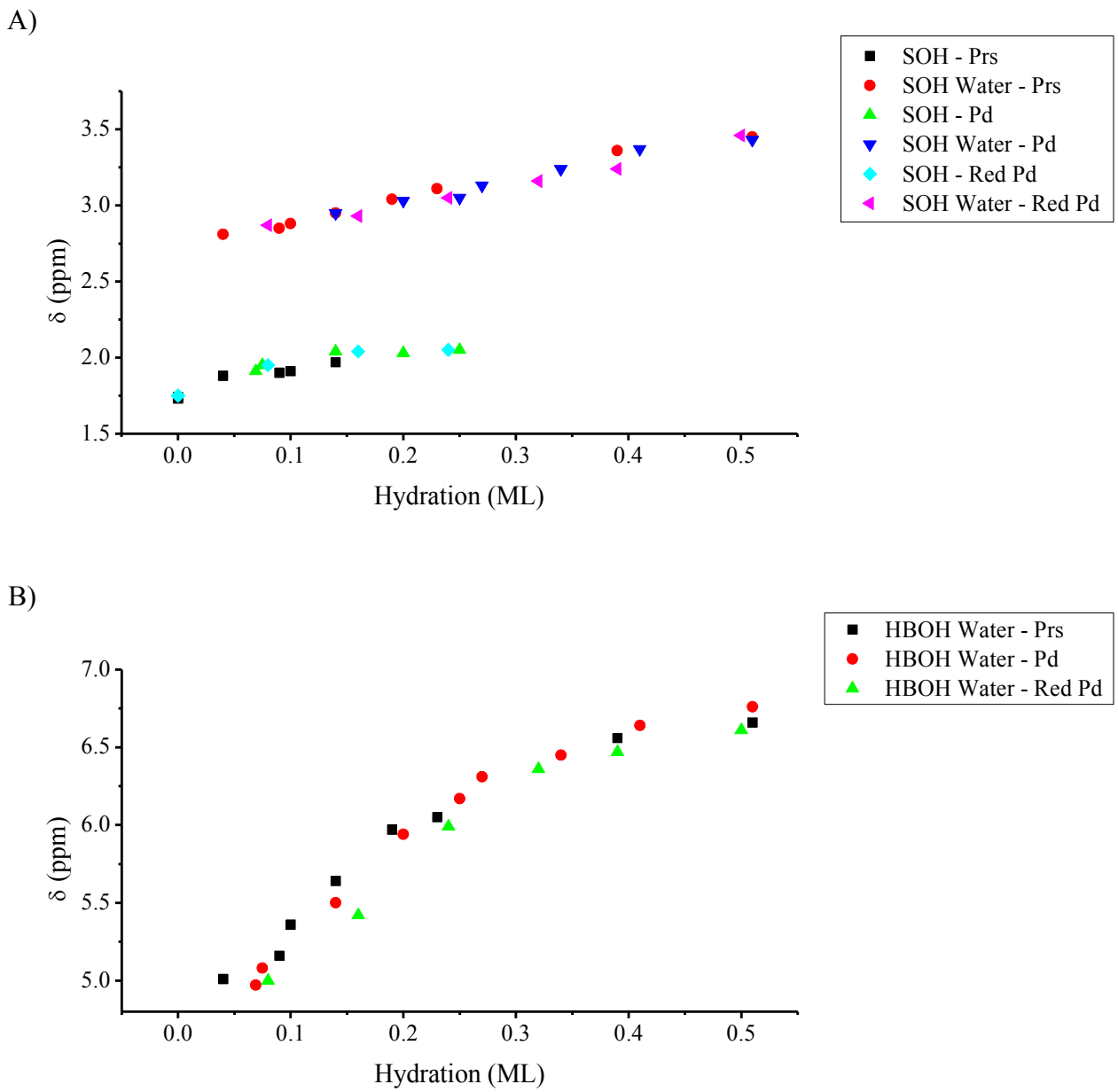

Figure 48: Comparison of the chemical shift of the unhydrated SOH peak (A), SOH water peak (A) and HBOH water peak (B) between the three samples.

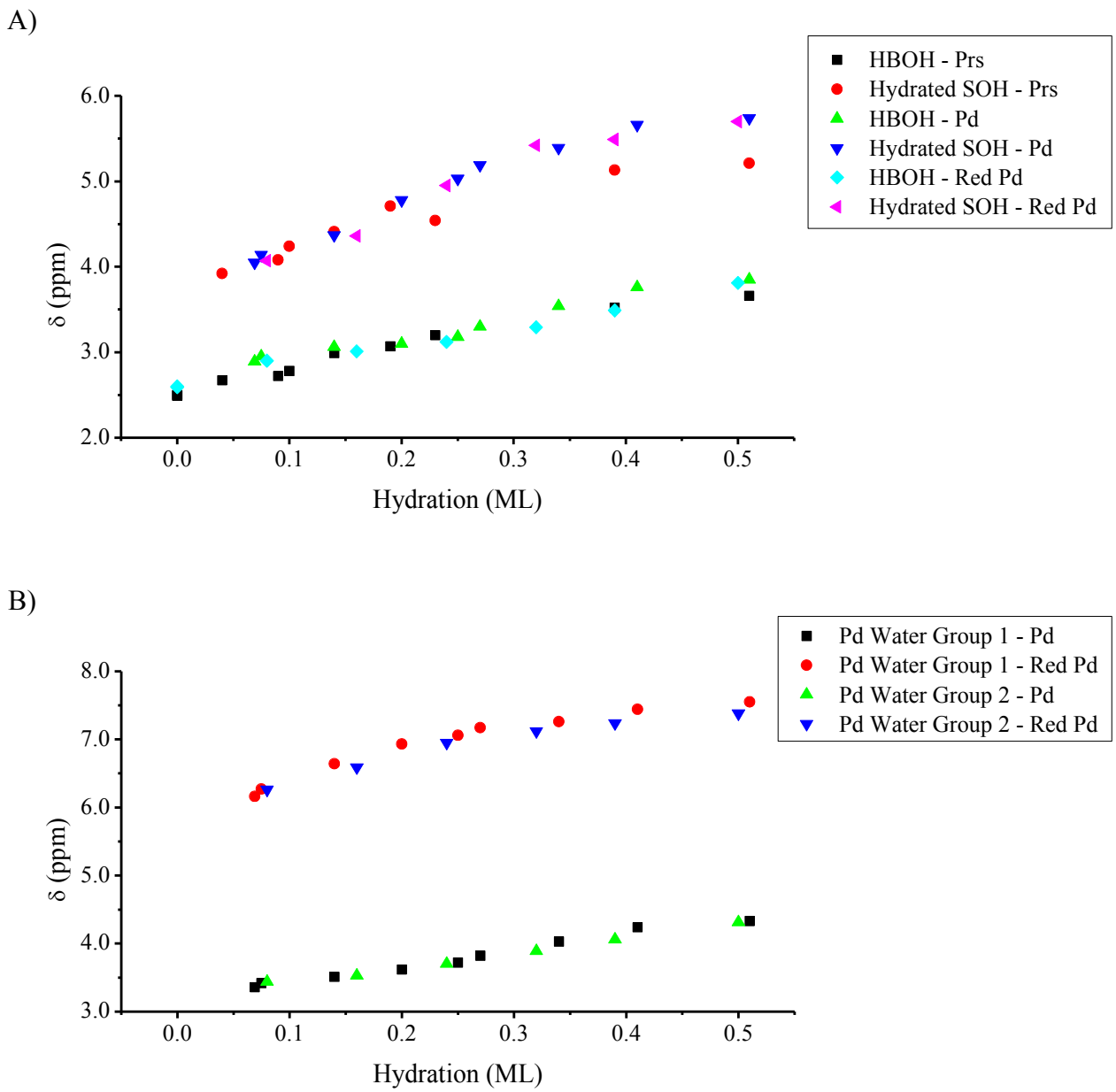

Figure 49: Comparison of the chemical shift of the HBOH peak (A), hydrated SOH peak (A), Pd Water Group 1 peak (B) and Pd Water Group 2 peak (B) between the three samples.

Figures 50 – 52 show a comparison between the peak areas for each of the three samples. The areas have been normalized so that the HBOH area is equal in all cases. This area is fixed in the fitting procedure, and so is constant across all hydration values. Differences between the three samples become apparent in the comparison of the areas of the hydrated and unhydrated SOH peaks, shown in Figure 50A. The differences in maximum unhydrated SOH area, and equivalently the maximum hydrated SOH area, are attributed to the slight differences in silanol populations given in Table 3. The unhydrated SOH area decreases faster with increasing hydration in the pristine MCM-41 sample, as compared to the palladized samples. For this same peak area, there is no significant difference between the two Pd loaded samples. The concomitant increase in hydrated SOH area behaves similarly: the area of this peak in the pristine sample increases slightly faster than in the Pd loaded samples. These results suggest that the presence of the metal is causing the SOH groups to require higher hydration levels for them to become hydrated.

The areas of the water peaks (Figures 50B and 51B) behave very differently when Pd clusters are present. The loaded samples see lower growth rates in the water peak areas, as well as lower total areas. The trend of the SOH water appears to be essentially the same for each sample: increasing linearly with hydration, perhaps with a slight logarithmic character. The values are quite different, however, with the pristine sample having the largest area for SOH water, Pd-MCM-41 having the lowest and the area for the reduced Pd-MCM-41 being roughly two to three times larger than Pd-MCM-41. Similarly, the area of the HBOH water peak is also smaller in the Pd loaded samples, but the trend is different from the pristine case. The area still increases until the SOH saturation, then stops increasing and decreases slightly after that point.

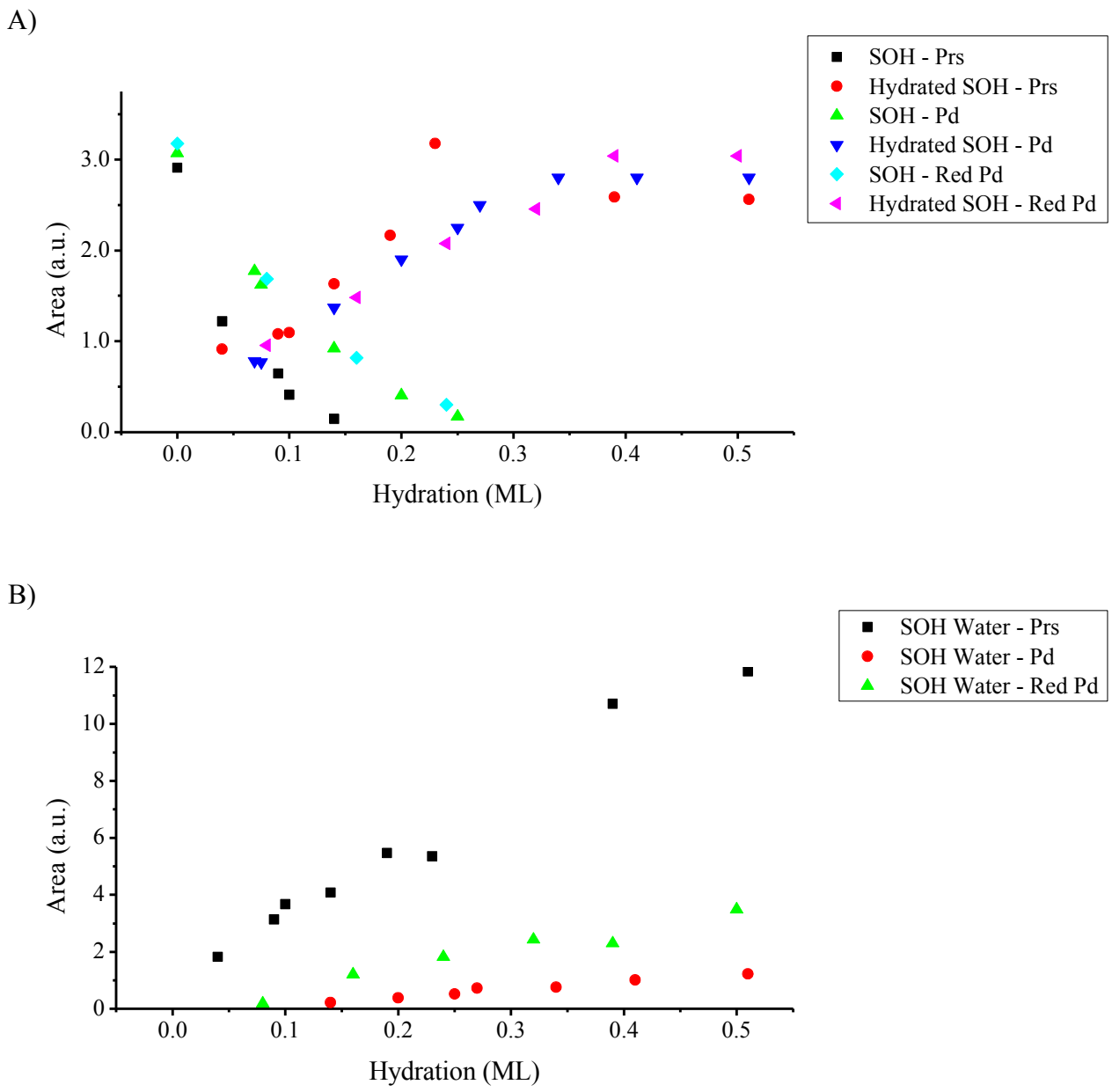

Figure 50: Comparison of the area of the unhydrated SOH (A), hydrated SOH (A) and SOH water peak (B) between the three samples.

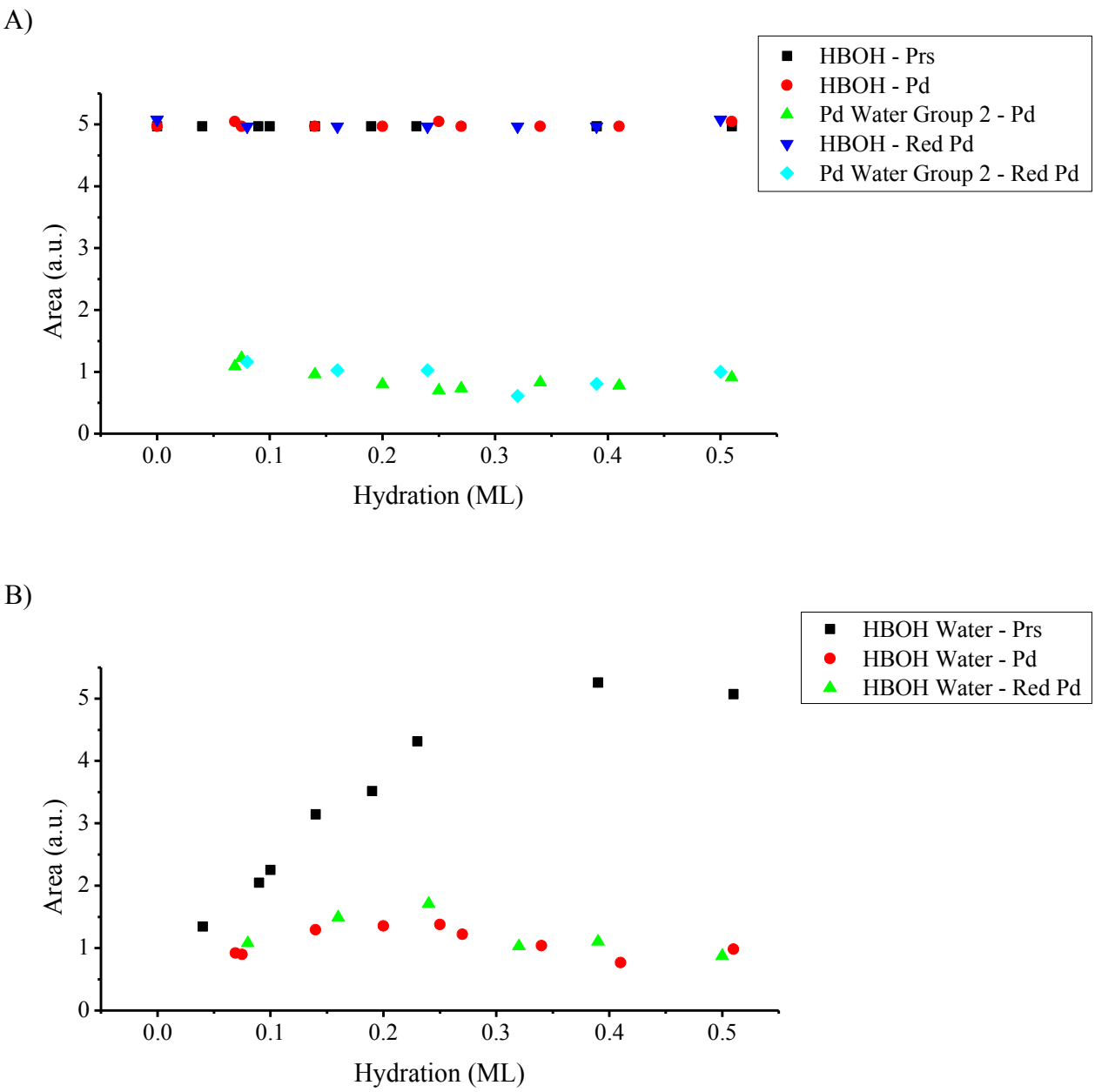

Figure 51: Comparison of the area of the HBOH peak (A), Pd Water Group 2 peak (A) and HBOH water peak (B) between the three samples.

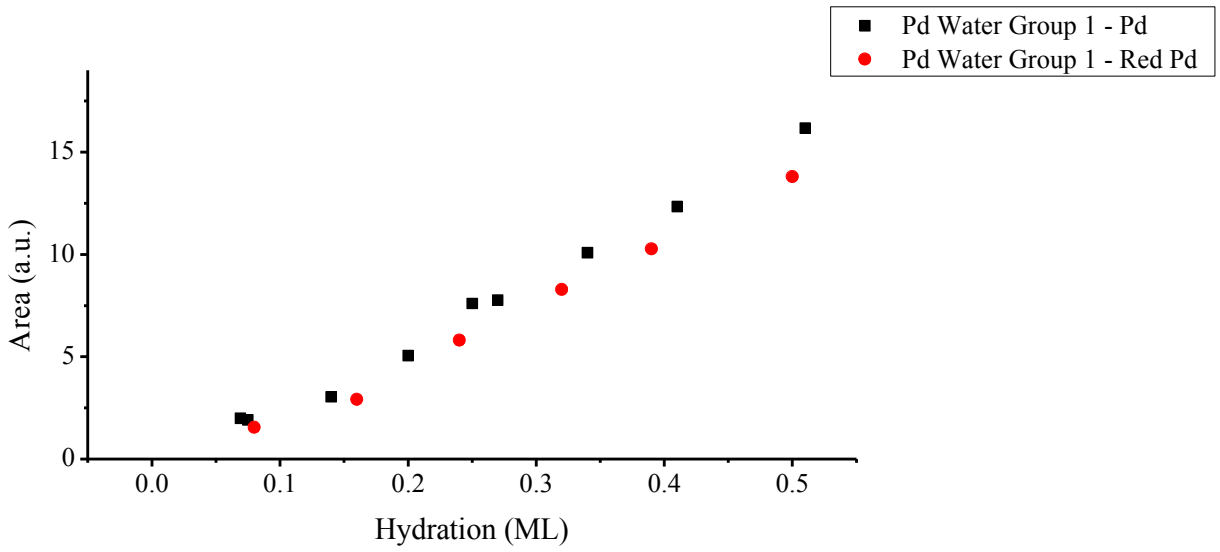

Figure 52: Comparison of the area of the Pd Water Group 1 peak between the two Pd loaded samples.

Qualitatively, the results for the water areas in the Pd loaded samples suggest that the presence of the metal is strongly influencing the water. Specifically, the water molecules are not as abundant in the same environments as in the pristine sample. They are most likely appearing in the NMR spectrum in Pd Water Groups 1 and 2. Comparisons of the areas of these two peaks between the Pd-MCM-41 and reduced Pd-MCM-41 samples are shown in Figures 51A and 52. Pd Water Group 1 is the largest peak in both Pd loaded samples and increases linearly with hydration. Therefore it is identified as a water group that is influenced by Pd to have a different chemical shift than the existing water groups. The area of this group is slightly smaller in the reduced sample. Pd Water Group 2 is very small, though of roughly constant area. Its size and behavior do not immediately identify it as a water group, but this will be discussed in depth in the next section.

Finally, Figures 53 – 56 show comparisons of the widths of the peaks in the Pd loaded samples to those in the pristine case. Overall, the widths in Pd-MCM-41 are found to be essentially the same as those in reduced Pd-MCM-41. This suggests that the behavior of the various proton groups, and the

environments they are found in, in these two samples are essentially identical, which is to be expected based on their synthesis details. There are few significant differences between the Pd loaded samples and the pristine sample. The graphs of the widths of the surface silanol groups are very similar between the three samples. The trends are identical in all cases. The unhydrated SOH peak (Figure 53A) is slightly (~ 0.1 – 0.2 ppm) wider in the Pd loaded samples compared to the pristine. The points in the width graph of the hydrated SOH (Figure 54B) all appear to be scattered along a similar curve, with no more than 0.5 ppm separating points from different samples. The widths of the HBOH group (Figure 53B) are identical at low hydration levels for all samples, but the constant value reached above SOH saturation is wider in the Pd loaded samples by about 0.3 – 0.5 ppm. The widths obtained for the surface silanols are indicating that the surfaces of the two materials are very similar. The marginally wider HBOH peak might suggest that the HBOH groups in the palladized samples are not hydrated the same way as in the pristine sample. Perhaps a different arrangement or orientation of silanol groups prevent water molecules from binding to the HBOH groups in a uniform way. Another possibility is that the difference between the area of the HBOH water peak, seen in Figure 51B, is connected to this wider area. Perhaps the reduced area is due to a limitation in hydration capacity. Less water to bind to the HBOH groups would leave some always unhydrated, effectively arresting the narrowing of the HBOH peak.

The similarities continue for the widths of the water peaks. The widths of the SOH water proton peaks (Figure 54A) are again essentially the same, with the palladized samples becoming slightly (~ 0.1 – 0.2 ppm) wider above SOH saturation. The most significant difference appears in the width of the HBOH water peak (Figure 55A). Though the width in the pristine sample remains essentially constant around 1.7 ppm, in the Pd loaded samples it begins at around 1.5 ppm and drops to around 1.0 ppm at the highest hydration level. This latter discrepancy could point to fewer water

binding configurations for the HBOH water. This seems to conflict with the HBOH peak being wider above SOH saturation in the Pd loaded samples, but only if there is enough water to saturate all of the HBOH groups. As was mentioned previously, the area of the HBOH water peak is low for the palladized samples. So perhaps there is not enough water available for complete HBOH hydration, leading to the broader saturation width of the HBOH peak, but the HBOH water that is present is in a single binding configuration, explaining the narrower HBOH water peak.

The findings here conclude that the application of the extended Walia model to fitting the NMR spectra of the Pd loaded MCM-41 samples has been successful. The agreement between the results of the palladized samples and those from the pristine case, most notably the chemical shifts of the corresponding peaks seen in all three samples, are strong indications that any remaining, significant discrepancies are caused by the presence of the Pd clusters. These differences will have to be explained by, and so provide the foundation of, any model that explains the behavior of water on Pd-MCM-41.

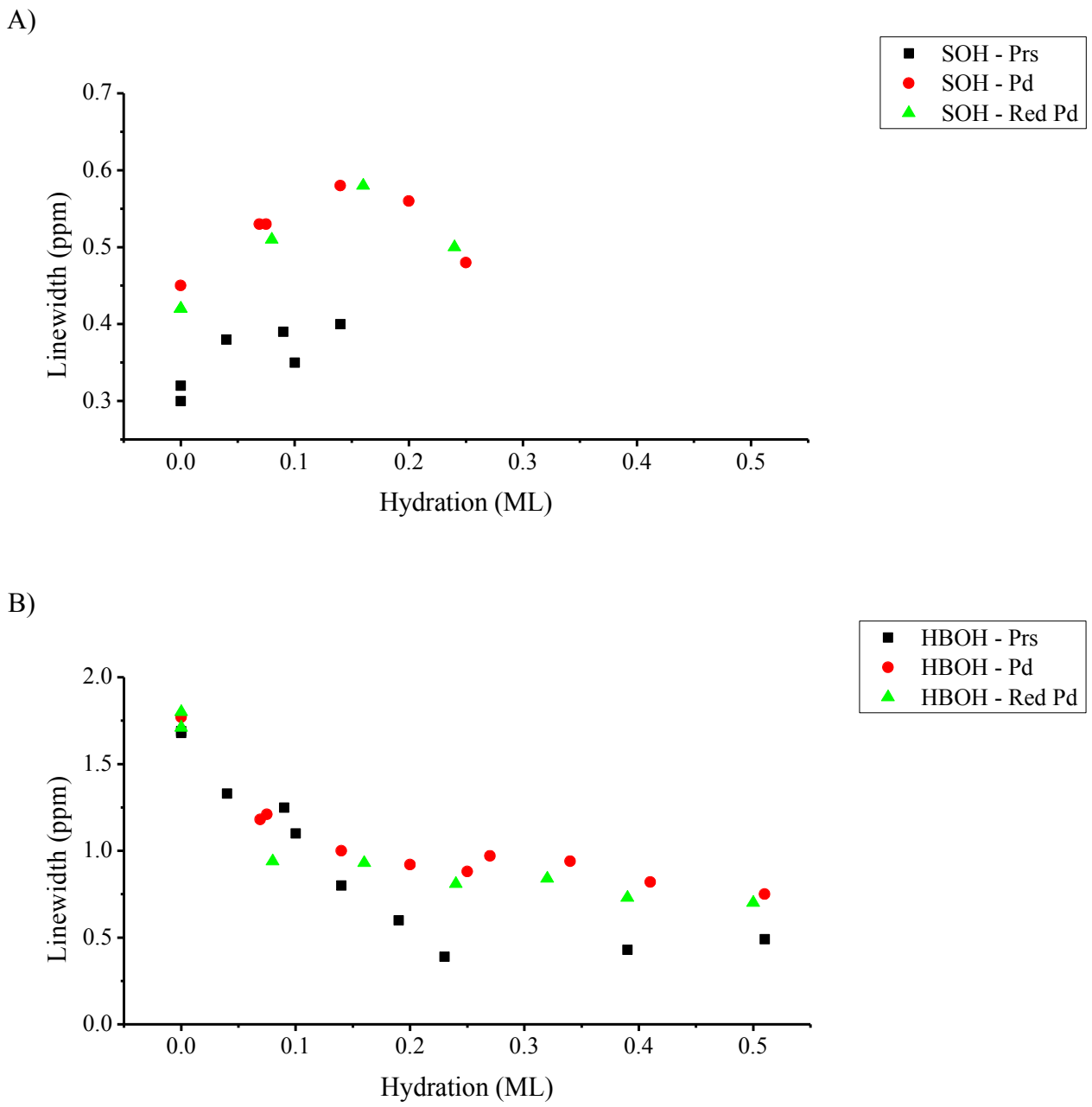

Figure 53: Comparison of the width of the HBOH peak (A) and SOH peak (B) between the three samples.

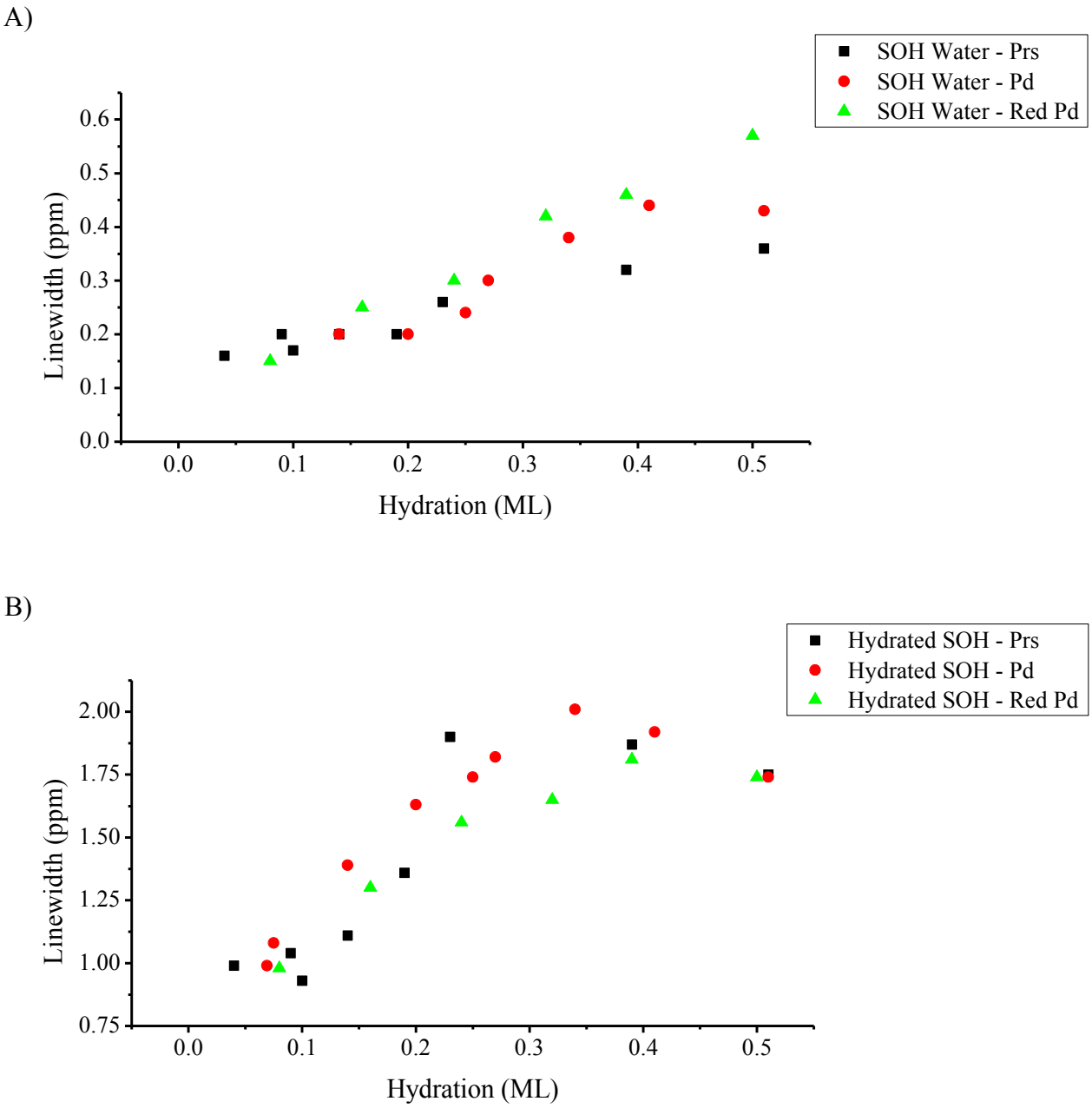

Figure 54: Comparison of the width of the SOH water peak (A) and hydrated SOH peak (B) between the three samples.

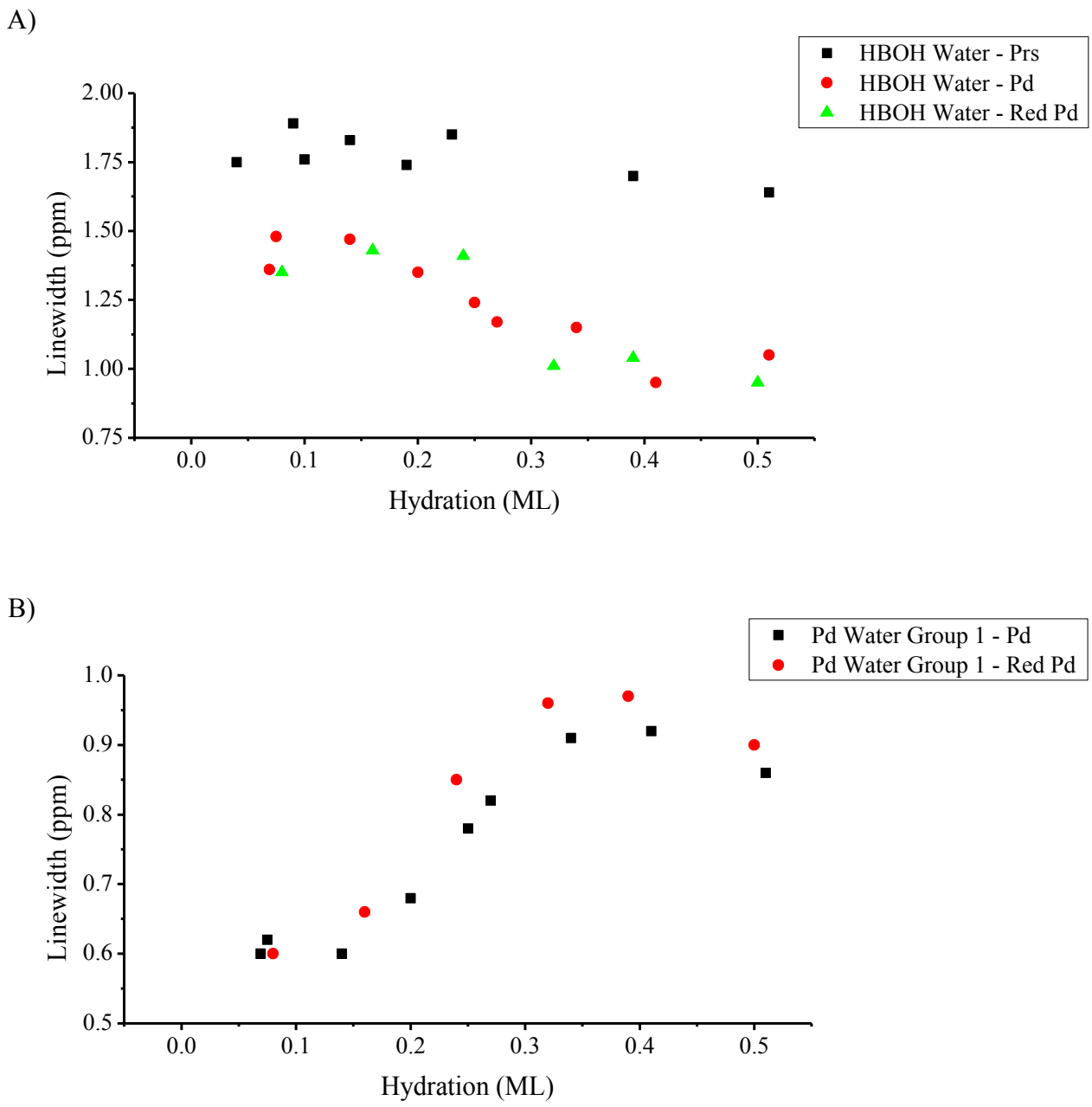

Figure 55: Comparison of the width of the HBOH water peak (A) and Pd Water Group 1 peak (B) between the three samples.

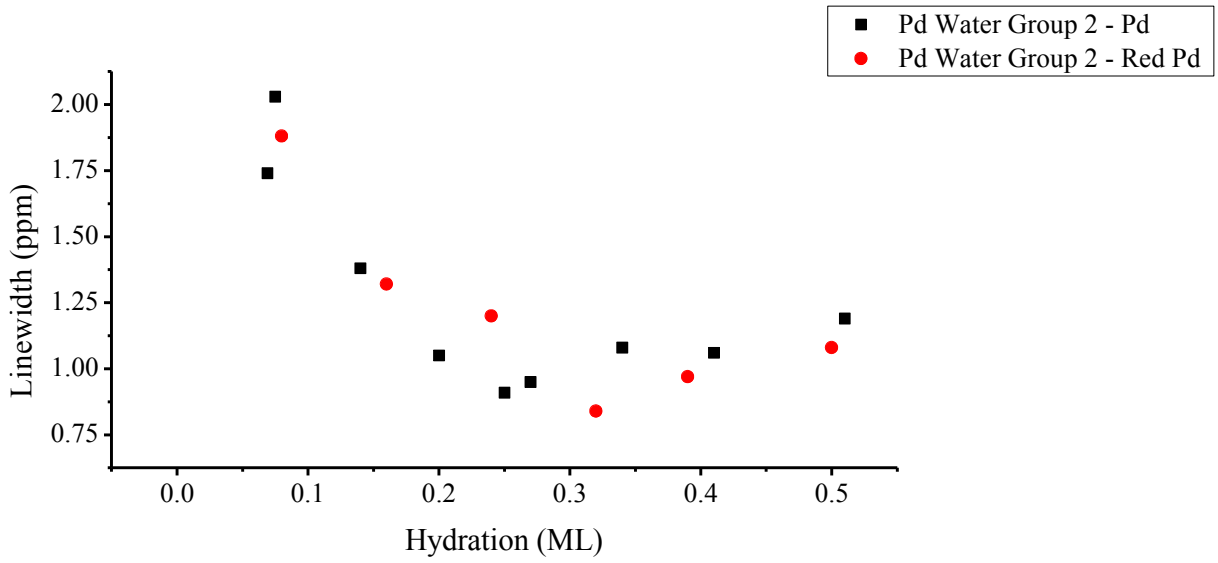

Figure 56: Comparison of the width of the Pd Water Group 2 peak between the three samples.

7.4. Behavior of Water on Pd-MCM-41

Based on the results and discussion up to this point, there a number of unique features in the behavior of water in palladium-loaded MCM-41, which are summarized here. The most obvious is the presence of two additional peaks, one accounting for the majority of the hydrated sample's spectral area, Pd Water Group 1, and another much smaller one, Pd Water Group 2. These peaks exist downfield of similar water peaks in the pristine MCM-41 sample.

In addition to these extra peaks, some of the peaks that are also observable in pristine MCM-41 have modified behavior. The unhydrated SOH group peak decreases in area slower with increasing hydration with the Pd present, likely a result of those silanol groups being hydrated slower with increasing hydration. There are much fewer water molecules hydrating the SOH groups, as compared to the pristine sample, though this is less true for the reduced Pd-MCM-41 sample. The HBOH water peak is also smaller in area, as well as narrower, though the HBOH group itself exhibits a wider peak. A subtle but important difference is the change in the ratio of areas for the water groups. This implies the SOH water and HBOH water are being affected differently.

These effects are predicted to be due to a layer of PdO on the clusters, not the Pd itself, since the oxide cleaned sample lacks these various features. Furthermore, more water returns to the SOH water peak in the reduced Pd-MCM-41 sample.

A difficulty in defining an appropriate model is the lack of details about the Pd clusters. While it is certain that Pd has entered the sample as nano-scale clusters, and that some of those clusters are 8 – 30 nm in diameter, there is no information about Pd clusters smaller than that. Therefore, reasonable approximations will have to be made.

In searching for potential theories to explain the observations unique to Pd-MCM-41, there are two simple, conspicuous possibilities that can be quickly excluded, thereby guiding the discussion towards superior models. The simplest idea to eliminate is any kind of a one-to-one type interaction between water and Pd; there are simply not enough metal atoms for it. In 38 mg of 2 % loaded Pd-MCM-41, there are 4.3×10^{18} Pd atoms, but there are 10^{19} water molecules at lowest, nonzero hydration level and nearly 10 times that at the highest. Furthermore, only a fraction of those Pd are accessible to the water, since some of the atoms will be in the interior of the metal clusters. So between 2 and 25 water molecules are being influenced by each Pd in the system. These numbers are likely 5 to 10 times higher, due to metal being present as clusters and not an atomically thin sheet.

The second theory to be quickly eliminated is that any of the groups are caused or influenced by residual NH_4 groups on the pore surface. If they were present in any significant number, they would appear in the sample's dry spectrum, as they did in the spectrum of dry NH_4-MCM-41 shown in Figure 30.

Two plausible explanations remain, which will be discussed in the remainder of this section. The first centers around water preferentially grouping around Pd clusters, and the second hinges on water experiencing a very large chemical shift as a result of its proximity to the metal.

7.4.1. Model A – Water Clustering

The first model for water behavior on Pd-MCM-41 identifies Pd Water Group 1 as an accumulation of water around the Pd particles that is exchanging with SOH water. This clustered water will be referred to as Pd-related multilayer water, or just Pd multilayer water for short, to distinguish it from the pore filling water seen in the pristine MCM-41 sample. This theory for the identity of Pd Water Group 1 readily explains its large area and the fact that its shift is between that of bulk or clustered water and SOH water.

In pristine MCM-41, water prefers to hydrate the pore surface with a single layer of water molecules before a second layer forms, which quickly leads to pore filling water. In order for multilayer water to develop in the vicinity of the Pd clusters, one to two layers must first form on the Pd cluster itself. If the metal cluster is small enough to be inside the pore, then these one or two layers might be enough to initiate capillary condensation, leading to pore filling water in the vicinity of the cluster. It is these capillary forces that keep the water localized to the Pd clusters, rather than diffusing away to drier areas of the pore surface, though the surface around the clusters is also hydrated to a greater extent. Pd Water Group 1 appears as soon as water is present in the sample, at hydration levels well below those where pore filling water occurs in pristine MCM-41. Therefore, the Pd clusters must contain preferential binding sites for water in order to initiate the development of this Pd multilayer water at low hydration levels.

A recent publication by Kan et. al. [108] presents work on the adsorption of water on thin films of PdO(101). As mentioned previously (see Figure 36) it has been concluded that it is the PdO that cause the spectral differences between pristine and Pd-MCM-41, not bare Pd itself. Figure 57 is a phase diagram from the work of Lundgren et. al. [109] for the oxide layer formed on Pd (100) based on temperature and partial pressure of O. According to Lundgren, the synthesis conditions that the current

Pd-MCM-41 sample undergoes following Pd introduction (calcination at 593 K for three hours under ambient laboratory atmosphere) will leave the Pd metal with a (√5x√5)R27° surface oxide layer [109], which is one layer of PdO(101) on Pd(100) [110, 111]. Three hours is more than sufficient for the layer to properly form, since Lundgren saw fully formed oxides within 300 s. While the experiments of Kan and Lundgren were performed on metallic films, they provide a reasonable approximation of what is occurring in Pd clusters. Therefore, the work of Kan on PdO(101) thin films is closely related to the current Pd-MCM-41 samples and their results can be used to aid in interpreting the current results.

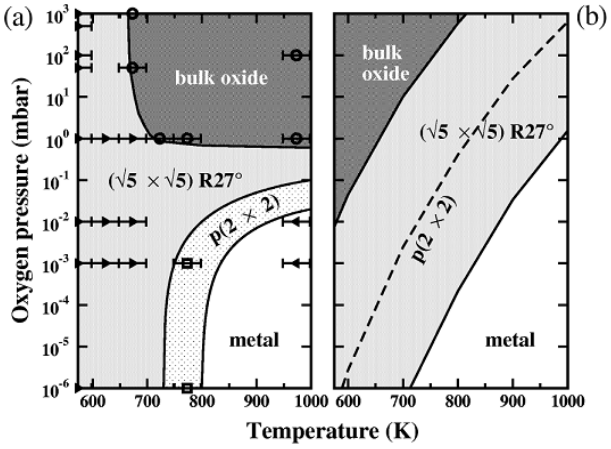

Figure 57: Temperature-pressure diagram for the phases found on a Pd surface under different conditions. (a) As observed by Lundgren. (b) As calculated from first principles. Taken from reference [109].

The primary result of Kan was observing how much stronger water is bound to PdO as compared to bare Pd. Using both density function theory calculations and temperature programmed desorption experiments, Kan found that when the metal oxide layer is sufficiently hydrated, the most stable binding configuration is the formation of two OH–H_2O complexes from four adsorbed H_2O molecules. The water molecules in these complexes are strongly bound to the surface. The adsorption energy (E_{ads}) for each water molecule was found to be between 90 – 100 kJ/mol depending on the hydration level. In addition to this strongly bound, chemisorbed layer of water, another adsorption

state accepts physisorbed water with an E_{ads} of 54 kJ/mol. The next adsorption state on PdO would be a multilayer of adsorbed water. For comparison, the E_{ads} of water on silica surfaces is 33 – 72 kJ/mol, depending on the site [112]. The binding energy of a water molecule that is bound to other water molecules in a water polymer complex [113 – 116] has been measured to be 25 – 67 kJ/mol, depending on the number of water molecules in the complex. The comparable E_{ads} for water on a silica surface and water in clusters suggest that it is possible that the water would remain in the vicinity of the Pd multilayer water and not preferentially diffuse away to drier regions of pore surface, as previously suggested. As an aside, the low E_{ads} of water on Pd (29 kJ/mol [117]), compared to that on PdO found by Kan, supports the previous conclusion that it is PdO, and not bare Pd, that is the cause for the observed spectral differences between water on pristine MCM-41 and Pd-MCM-41.

The high E_{ads} of water on the PdO surface of the metal clusters suggests that it contains the preferential binding sites for water that are required for Model A of water behavior on Pd-MCM-41. This preferential binding of water leads to the Pd multilayer water identified as part of Pd Water Group 1. That the area of the unhydrated SOH group decreases slower with increasing hydration in the Pd loaded samples as compared to the pristine case supports the idea that water is preferentially being taken up into a different site, effectively "starving" the silica surface of water. Therefore, the strongly bound first, and possibly second, layer of water molecules on the PdO surface of the metal clusters are determined to comprise Pd Water Group 2. The strong chemisorption and physisorption of the water molecules in the first water layer would be established by the first water molecules present in the system, which explains why Pd Water Group 2 appears at its maximum area at the first non-zero hydration. The slight drop in area with increasing hydration may be due to exchange with the higher water layers on the Pd clusters that comprise part of Pd Water Group 1.

The high chemical shift of Pd Water Group 2 is due to the highly hydrated nature of its

constituent complexes, and the strong hydrogen bonding that is related to the high E_{ads}. A higher local hydration surrounding the OH–H_2O complexes means that all of their H atoms are experiencing hydrogen bonds, shifting them to higher chemical shifts. This is similar to the high shifts seen for HBOH water and hydrated SOH groups. As for the contribution from strong hydrogen bonding, it is known that the stronger the hydrogen bond experienced by a hydrogen atom, the greater the chemical shift [21]. A shift downfield is related to a decrease in electronic shielding, which would occur if the proton is drawn further away from its O atom. This is again similar to the HBOH water, which has the highest chemical shift in the pristine sample, and the strongest hydrogen bonds.

The issue with this peak identification is one of populations. There are between 7.6 – 9.7 x 10^{18} H atoms, or 4.8 x 10^{18} water molecules, in the Pd Water Group 2 peak. But there are only 4.3 x 10^{18} Pd atoms in the entire sample, and some of these won't be accessible at the surface of the cluster. The available fraction will depend on the cluster size. Due to the incompleteness of direct information on the size and distribution of the Pd particles present in the sample, estimates must be made. In Appendix B, arguments are presented to justify an approximation of 10 – 25% of the Pd atoms being available at the surface of the Pd clusters. This means that each of these surface Pd atoms must have a OH–H_2O complex bound to it along with two to four water molecules strongly associated with it to account for the area of the Pd Water Group 2 peak. The work of Kan justifies up to one water molecule being strongly bound to the OH–H_2O complex. It could be that some of the higher layer waters are also bound strongly enough to be shifted as high as Pd Water Group 2 requires. Alternatively, the area could be larger due to rapid exchange with these higher layer water molecules.

The drop in area of the SOH water and HBOH water peaks could be explained by the aforementioned water scavenging effect of the PdO layer on the metal clusters, but it does not explain the different ratio between them. The Walia model predicts two SOH water for every one HBOH

water, but in these results, the HBOH water area is higher. This suggests that some of the SOH water must be undergoing fast exchange with the PdO water.

Fast exchange between SOH water and Pd multilayer water would cause the peaks of both groups to be shifted to a population-weighted average chemical shift of the two species, as described by equation (55). The SOH water that is still visible in the spectrum at its expected, unshifted position must therefore not be undergoing exchange. This could be caused by the distribution of Pd clusters. The clusters may simply be too distant from each other for all the SOH water to reach them in the NMR timescale (ie. over the course of NMR signal recording, ~ 1 μs). The drop in the area of the HBOH water peak is assumed to be due to less water being available on the surface – the water scavenging idea mentioned above – rather than due to exchange. The results of Trebosc [29] support this assumption, where it was found that strongly bound water at a chemical shift of 6.1 ppm in a MCM-41 sample hydrated to 0.2 ML exchanged slowly with the remaining water.

If the size and shift of the groups involved in the exchange are determined, then the shift of the Pd Water Group 1 peak should be reproducible using equation (55), while providing a way to check some the assumptions made along the way.

Since the HBOH water is assumed to not participate in exchange, it provides a means of estimating how much water is actually involved with the silica surface. In order for the area plot of the SOH water peak to be in the expected proportion to that of the HBOH water, it would have to be roughly 5 to 10 times larger. A more precise number can be obtained by looking at group populations at SOH saturation. After calibrating the peak areas to a proton count, it is found that there are 3.3 x 10^{19} SOH groups in the dry sample. The lowest hydration that does not have an observed SOH peak is 0.27 ML. At this hydration, there are 3.9 x 10^{18} water molecules in the SOH water peak. In order for the area of the unhydrated SOH peak to drop to zero there must be at least as many water molecules in

the SOH water peak as there are SOH groups. Therefore, there must be $3.3 \times 10^{19} / 3.9 \times 10^{18} = 8.5$ times as many water molecules present in the sample as is being reported by the SOH water peak. The extra SOH water is appearing in Pd Water Group 1.

This factor of 8.5 allows the intrinsic populations involved in the exchange to be calculated. The number of SOH water molecules that are undergoing exchange is 7.5 times the number seen in the SOH water peak (the missing 1.0 is the area seen in the SOH water peak itself, since this is by definition not involved in exchange). Subtracting this from the number of water molecules seen in Pd Water Group 1 leaves the number of water molecules that are in the Pd multilayer water groups surrounding the Pd clusters. This information is summarized in Table 7.

Hydration Level (ML)	**Water Molecules in SOH Water Peak (x 10^{18}), $n_{SOH\ water}$**	**Water Molecules in Pd Water Group 1 (x 10^{18}), $n_{Pd\ Water\ Group\ 1}$**	**SOH Water Molecules Exchanging with Pd Multilayer Water (x 10^{18}), [a] $n_{SOH\ water}^{exchange} = 7.5\, n_{SOH\ water}$**	**Pd Multilayer Water Molecules (x 10^{18}), [a] $n_{multilayer} = n_{Pd\ Water\ Group\ 1} - n_{SOH\ water}^{exchange}$**
0.069	0	10.8	0 (0)	10.8 (1.0)
0.075	0	10.4	0 (0)	10.4 (1.0)
0.14	1.2	16.5	8.8 (0.53)	7.7 (0.47)
0.2	2.1	27.4	15.5 (0.57)	11.9 (0.43)
0.25	2.8	41.2	21.1 (0.51)	20.2 (0.49)
0.27	3.9	42.1	29.4 (0.70)	12.7 (0.30)
0.34	4.1	54.7	31.0 (0.57)	23.7 (0.43)
0.41	5.5	66.9	41.1 (0.61)	25.8 (0.39)
0.51	6.7	87.7	49.9 (0.57)	37.8 (0.43)

Table 7: Calculation of the number of water molecules in the two groups that constitute Pd Water Group 1: Pd multilayer water and the SOH water exchanging with the multilayer water. [a]The relative contribution of each constituent water group to the total number of water molecules in Pd Water Group 1 is shown in parentheses.

With the populations having been calculated, only the chemical shifts of the two groups remain to be determined. The Pd multilayer water will be treated like bulk or clustered water. The 4.6 ppm

observed for pore filling water in the pristine MCM-41 sample is not appropriate in this case, since this value is likely the result of fast exchange between water in the middle of the pore and water hydrogen bonded to surface silanol groups. The chemical shift of bulk or cluster water has been reported to be between 4.7 and 5.5 ppm [29, 30, 118], so an average value of 5.1 ppm is chosen to represent the chemical shift of the Pd multilayer water. The chemical shift of the SOH water is hydration dependent, but the Pd clusters have changed the distribution of water on the pore surface, altering the effective hydration near them. So the chemical shift of the SOH water peak in the Pd-MCM-41 results might not give the required value. Therefore, another treatment is needed.

The effective chemical shift of the SOH water that is exchanging with the Pd multilayer water can be approximated by comparing the amount of water in that group per surface silanol to the same in the pristine MCM-41 sample. To do so, a linear fit is obtained of a graph of the chemical shift of SOH water in pristine MCM-41 as a function of SOH water molecules per surface OH. This graph and associated fit are shown in Figure 58. The equation for this line can then be used, along with the number of exchanging SOH water in the Pd-MCM-41 sample from Table 7, to determine the effective chemical shift of this water group. The results of this are shown in the 2nd column of Table 8. The rest of Table 8 shows the results of applying equation (55) to obtain the exchange averaged chemical shift, which should be the same as that of Pd Water Group 1. Figure 59 shows plots of the calculated (column 6 of Table 8) and measured (column 7) chemical shifts of Pd Water Group 1 as a function of hydration. Figure 60 shows the difference between these calculation and measurement (column 8).

Hydration Level (ML)	Chemical Shift of Exchanging SOH water (ppm)	Chemical Shift of Pd Multilayer Water (ppm)	Population of Exchanging SOH water	Population of Pd Multilayer Water	Calculated Chemical Shift of Pd Water Group 1 (ppm)	Measured Chemical Shift of Pd Water Group 1 (ppm)	Difference Between Calculated and Measured (ppm)
0.14	2.84	5.10	0.46	0.54	4.05	3.51	0.54
0.20	2.95	5.10	0.49	0.51	4.05	3.62	0.42
0.25	3.05	5.10	0.44	0.56	4.19	3.72	0.48
0.27	3.20	5.10	0.60	0.40	3.95	3.82	0.13
0.34	3.22	5.10	0.49	0.51	4.18	4.03	0.15
0.41	3.40	5.10	0.53	0.47	4.20	4.24	-0.05
0.51	3.56	5.10	0.49	0.51	4.34	4.33	0.01

Table 8: Calculation of the chemical shift of Pd Water Group 1 using equation (55). Note: Lower hydration levels were left out of the calculation. The spectra from these experiments did not contain SOH water peaks, so the calculation of the weighted average would just give the Pd multilayer water shift.

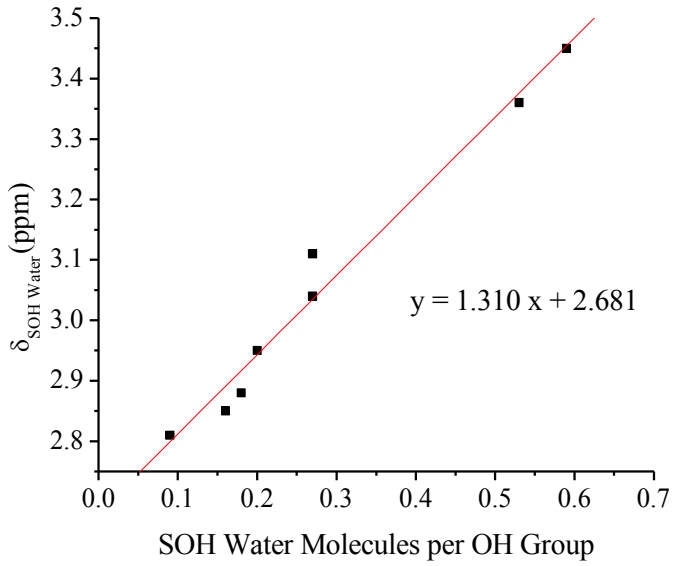

Figure 58: Determination of the relationship between the chemical shift of SOH water and the number of SOH water per OH group.

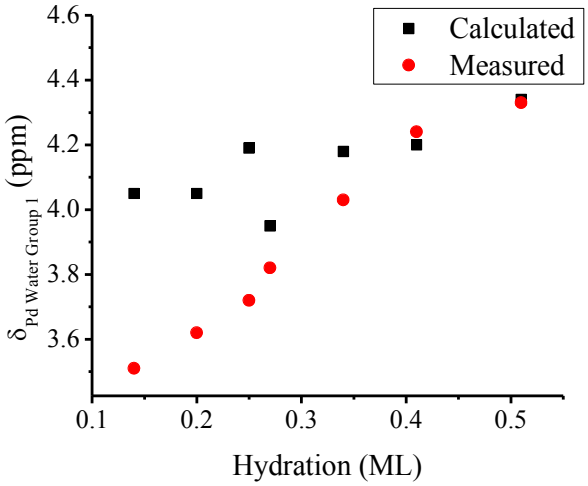

Figure 59: Comparison of the calculated and measured chemical shifts for Pd Water Group 1.

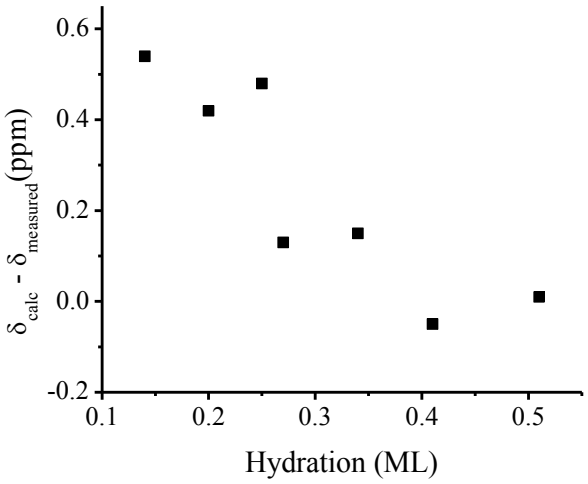

Figure 60: Difference between the calculated and measured chemical shifts for Pd Water Group 1.

Overall, the calculated chemical shifts for Pd Water Group 1 are reasonably close to the measured values. Figures 59 and 60 show that the calculated chemical shifts get closer to the measured values with increasing hydration. The fact that the discrepancy is larger at low hydration values could be due to a poorly defined area curve for the SOH water, which this analysis hinges upon. The area of this group is low, and also difficult to fit in the NMR spectrum, leading to an area plot that is linear, while the same group has a slightly logarithmic character for the pristine MCM-41 sample. Furthermore, the lower hydration levels clearly have additional distortion since the measured SOH water area is zero until 0.14 ML. There is still SOH water exchanging with the Pd multilayer water below 0.14 ML, so this is definitely impacting the calculated shifts in the lower hydration levels. The fact that the calculated chemical shift matches well with the measured shift at higher hydration levels, despite the crudeness of the approach, is very encouraging as to the validity of the model.

In light of the successful definition of Pd Water Groups 1 and 2, the effect of reducing Pd-MCM-41 can be explained. The drop in area of Pd Water Group 1, and the roughly equal gain in area of SOH water, is caused by less SOH water exchanging with Pd multilayer water. This must be due to a fairly small drop in the amount of PdO present on the Pd clusters, since Pd Water Group 2, the water

bound to the PdO groups themselves, does not see a significant decrease in area. Fewer PdO groups means fewer sites causing pore condensation of water, which causes less Pd multilayer water, leaving more SOH water groups not experiencing exchange.

In order for the above exchange analysis for Pd Water Group 1 to be valid, the system has to be in the fast exchange regime. The NMR lines of two equally populated groups begin to merge at an exchange rate of roughly [119],

$$k = \frac{\pi}{\sqrt{2}} \Delta v = 2.22 \Delta v \tag{67}$$

where Δv is the frequency separation of the two peaks. At the largest peak separation,

$$\Delta v = (5.0\ ppm - 2.8\ ppm)(500\ Hz/ppm) = 1100\ Hz \tag{68}$$

So initial merging would occur at an exchange rate of approximately 2400 s^{-1}, and a single peak would show up at exchange rates likely above 5000 s^{-1}. This exchange rate is not out of the question for the situation described. In porous silica systems, the exchange rate between pore-filling water and water bound to surface sites is widely accepted as fast [32 – 35], with one publication stating the rate to be in the range of $10^3 – 10^4$ s^{-1} [32].

Model A for the behavior of water on Pd-MCM-41 is summarized in Figure 61. Any water that is incident on a Pd cluster, which is coated in a PdO layer, will readily chemisorb into a first layer, forming the OH–H_2O complexes described by Kan, as well as physisorb into a second, strongly bound layer. These water groups are identified as Pd Water Group 2. These strongly bound water layers lead to further layers of water becoming associated with the Pd cluster, as well as the silica surface surrounding the cluster being hydrated more than regions lacking Pd clusters. In regions where the Pd clusters are sufficiently small to enter the pore, this wetting of the cluster and silica will be aided by the same capillary condensation that leads to pore filling water at higher hydration levels in pristine MCM-

41. The Pd multilayer water and nearby SOH water, whose population sizes are roughly equal, exchange rapidly enough to collapse their NMR lines into a single line at a weighted average chemical shift, which is identified as Pd Water Group 1.

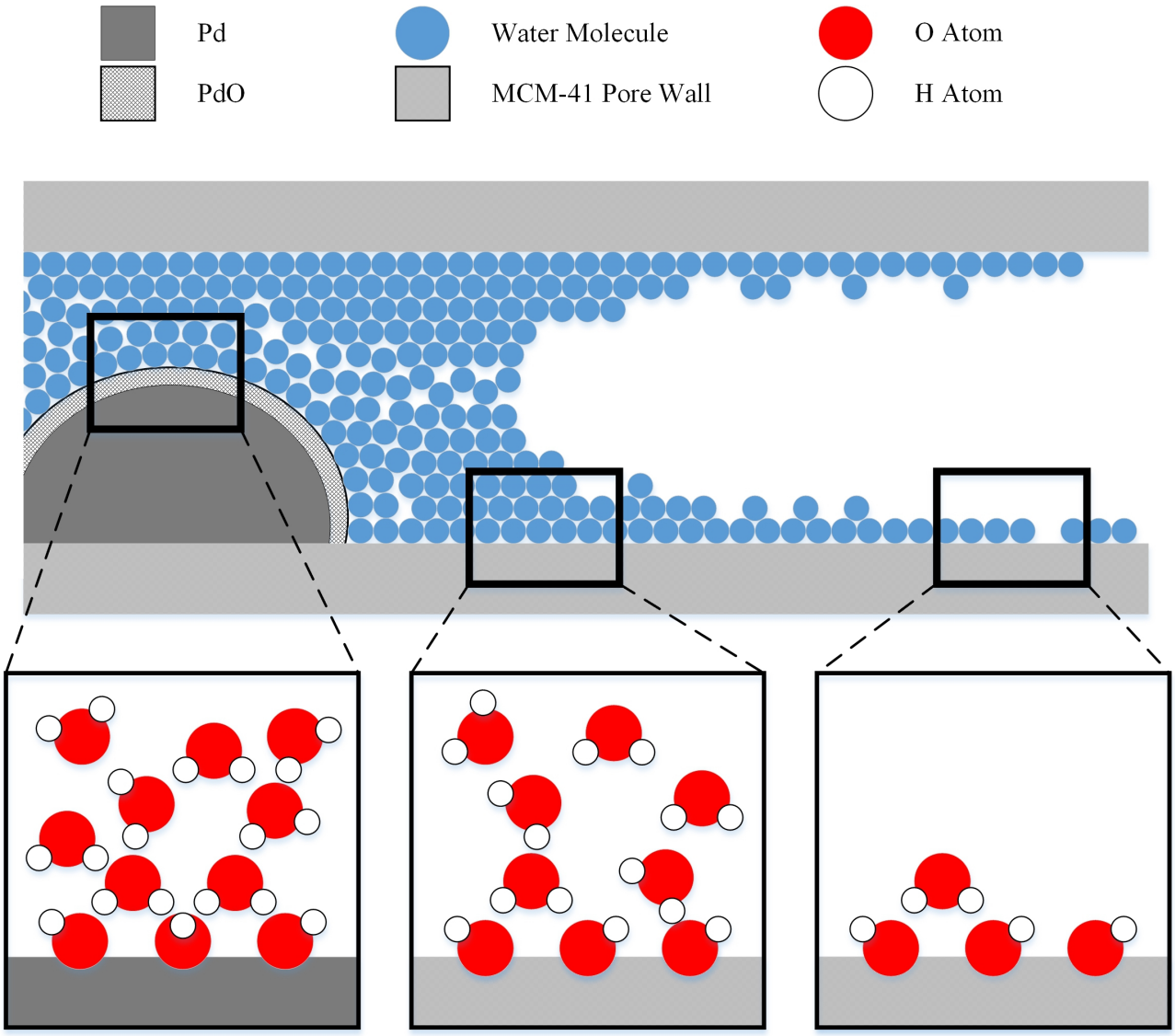

Figure 61: Schematic of Model A for the behavior of water in Pd-MCM-41. The three panes at the bottom show details of each region of interest. The leftmost pane shows the details of water arrangements at the Pd/PdO surface, which include the OH–H_2O complexes described by Kan. The middle pane shows the multilayer SOH water found on the silica surface near the Pd clusters. The rightmost pane shows a standard, submonolayer hydration of the silica surface.

7.4.2. Model B – Large, Palladium-Induced Shift

One of the implied requirements in the previous model is that the Pd clusters do not greatly

affect the chemical shift of the nearby water molecules. There are a number of mechanisms that exist, however, that could result in rather large chemical shifts for any protons in the vicinity of the Pd metal clusters. These possible mechanisms must be addressed, and discounted, which is the purpose of this section.

The way a water group with a large shift would be incorporated into an alternate model for the behavior of water on Pd-MCM-41 would be solely through exchange. Each of the two Pd Water Groups are about 1 ppm downfield from a water group. Therefore, a possible scenario involves Pd Water Group 1 and Pd Water Group 2 being identified as the results of highly shifted water rapidly exchanging with SOH water and HBOH water, respectively. This is the essence of Model B for the behavior of water on Pd-MCM-41.

The highly shifted water group required by Model B will be referred to as Pd shifted water for the sake of clarity. This Pd shifted water would have to be located as close as possible to the Pd clusters in order to maximize the metal's effect on it. For this reason, the same configuration of water bound to the Pd clusters applies as was outlined in the previous section. The first layer of water will therefore involve the $OH–H_2O$ complexes described by Kan.

Based on the areas involved, the Pd shifted water must be exchanging with the silanol water groups to different degrees. That is, the area of Pd Water Group 1 peak is very large and the remaining SOH water is very small, so nearly all of the SOH water is exchanging with Pd shifted water. The area of Pd Water Group 2 peak on the other hand is smaller than that of the HBOH water peak, so only a small portion of the total HBOH water is undergoing exchange with the Pd shifted water. This requires the Pd shifted water to be exchanging with the two water groups to different degrees. Also, the exchange system has to be uncoupled, meaning the Pd shifted water that is exchanging with SOH water cannot simultaneously be exchanging rapidly with HBOH water, otherwise only a single peak

would be observed, rather than two. This could be explained by the SOH groups and HBOH groups occupying separate regions of the pore surface. Indeed HBOH groups must occur in long chains, one silanol group hydrogen bonding to another, and that group to another, and so on, in order for the silanol population distribution in dry MCM-41 to be explained [21]. This physical separation of the two types of silanol groups would also explain the previously reported result of the two types of silanol water exchanging only slowly with each other [29]; if the two types of silanol groups reside in separate regions that are distant from each other, then the water molecules that are associated with them will require long timescales in order to exchange magnetization.

If this picture of the MCM-41 pore surface is accepted, then it offers a few possible explanations as to how the Pd shifted water may exchange differently with the two groups. One idea is that the Pd clusters are distributed on the surface in such a way that they occur more frequently in SOH populated regions (perhaps due to the pore surface in these areas simply having more room) compared to those occupied by HBOH groups.

Another explanation that would lead to Pd clusters being found mainly in SOH occupied regions requires the NH_4 groups that are introduced in the preliminary material synthesis steps to truly seed the Pd cluster formation. Then, if the NH_4 molecules exchange with SOH groups more readily than the HBOH groups, since the latter are all involved in two hydrogen bounds, then Pd clusters would mainly be seeded in the SOH dense portions of the pore surface.

An alternative to the idea of Pd being distributed differently in separate regions of the pore surface is that the water groups themselves could have different mobilities. On average, according to the Walia model, the HBOH water are involved in more hydrogen bonds than the SOH water, so it is reasonable to assume that the SOH water would be more mobile, undergoing more jumps between surface hydration sites.

These various theories can explain the Pd shifted water exchanging separately, and to different degrees, with the two water groups. So this observation does not condemn Model B at the outset, though it does impose some as yet unconfirmed constraints on the nature of MCM-41.

In order for the SOH water and HBOH water peaks to be shifted in the right direction, the peak for the Pd shifted water must have a large shift, downfield from the positions of the silanol water peaks. The hyperfine interaction between a nuclear spin and that of an unpaired electron is the source of the very large chemical shifts [45, 120, 121], since the magnetic moment of the electron is roughly 10^5 times larger than that of a nucleus. The resulting chemical shift adjustment is given different names based on the system it is observed in. In systems involving the conduction electrons of metals, it is referred to as the Knight shift [45], while in those containing paramagnetic atoms or complexes, it is called a paramagnetic shift [122]. Regardless of the origin, the electron-nucleus coupling of the hyperfine interaction can be broken down into two parts: the contact shift and the pseudocontact shift.

The pseudocontact shift is a through-space, dipolar interaction between the magnetic moment of a nucleus and that of an unpaired electron. Its Hamiltonian has essentially the same form as the internuclear dipolar Hamiltonian [120] (see equation (34)), which has several consequences. First, while the long range of this interaction would affect many water molecules in the current system, its magnitude decreases with the cube of nucleus-electron distance. It is impossible to get a 10 ppm shift, even with optimal parameter choices [120]. The pseudocontact shift is regularly used in the refinement of complex molecular structures like proteins [123]; the NMR spectrum from a molecule with an added paramagnetic ion can be compared to a diamagnetic equivalent and the size of the shift provides information about the distance of each residue to the location of that ion. A typical shift for the closest hydrogen atoms to the paramagnetic center, which would experience the largest shifts, is about 4 ppm [123]. So the maximum shifts caused by this mechanism are quite limited. The second consequence

of the interaction's dipolar nature is that the MAS that the current sample undergoes will diminish the pseudocontact shift's already limited magnitude. In systems where both the contact and pseudocontact shifts are known to coexist, the latter is routinely ignored [124].

The contact shift that would exist in the present sample would be a Knight shift, since it involves a large collection of metal atoms, whose unpaired electrons would be conduction electrons, rather than those residing in a paramagnetic ion bound to a molecule. Normally the Knight shift is used to explain the large change in metal-NMR frequency (eg. ^{195}Pt NMR) between bulk metal and diamagnetic compounds of the same metal [45]. It can also be used to explain the shift of atoms or molecules adsorbed on, or otherwise bound to, the surface of a metal. For example, it is the cause for one of the largest ^{13}C NMR shifts recorded, which is CO being shifted 310 ppm when bound to a Pd surface [121]. In ^{1}H NMR, it causes the shift of H adsorbed on and absorbed in Pd metal. This latter example however, is the matter of much debate. The hydride that results from the absorption often bears two NMR lines, whose identity is the source of great discourse. The most thorough explanation was put forth by Rades [125], who detailed the contribution to the Knight shift from its various sources. The contributions from the electrons are divided into that from the s and d conduction electrons in the metal. These contributions depend on the density of states at the Fermi level. For a metal with nearly complete d band, such as is the case for Pd, the density of d states will be high. This leads to a primarily negative contribution to the Knight shift, leading to an upfield shift, which has been measured previously [126, 127]. Therefore, the Knight shift cannot be the cause of the downfield shift of the Pd shifted water. Furthermore, the H is not bound to the Pd cluster in the OH–H_2O complex, rather the O is. So the effect would have to be transmitted through chemical bonds. While this has been shown to occur [128], the effect diminishes for H atoms that are a further number of bond lengths away from the metal. Based on these various points, the Knight shift will likely not be

responsible for the large, downfield shift of the Pd shifted water.

Despite the above discussion raising serious doubts that a large, downfield shift could be explained for water bound to a Pd metal cluster, it is still instructive to determine what chemical shift the Pd shifted water requires in order to obtain the observed shifts of Pd Water Groups 1 and 2. For this argument, Pd Water Group 1 will be selected, though what follows is equally applicable to Pd Water Group 2.

Rearranging equation (55) for the necessary chemical shift, and relabeling the subscripts, gives,

$$\delta_{Pd\ Shifted\ Water} = \frac{\delta_{Pd\ Water\ Group\ 1} - \delta_{SOH\ Water}\, p_{SOH\ Water}}{p_{Pd\ Shifted\ Water}} \tag{69}$$

Here, the populations, p_i, are relative not to the entire system, but only the two water groups involved in the exchange. The total population will therefore be given by the number of water molecules calculated from the area of Pd Water Group 1 NMR peak. The population of the Pd shifted water will be determined from the known number of Pd atoms in the sample, the approximate fraction of those atoms at the surface of the Pd clusters and the number of water molecules associated with each surface Pd as predicted by the Kan model. The latter two of these are discussed in the previous section, where it is made clear that each has a range of possible values.

Regardless of what the interaction may be, there is a limited range of the number of water molecules that could be significantly shifted by the Pd metal. The range of reasonable values are 0.5 (corresponding to just the OH of the OH–H_2O complex being shifted by the Pd) to 2.5 (an additional two water molecules being involved). As discussed previously, the fraction of Pd atoms at the cluster surface is assumed to be between 10 and 25 %.

The SOH water population is determined by taking difference between the total water in Pd Water Group 1 and the calculated population of the Pd shifted water. The observed chemical shift of

the SOH water, at the appropriate hydration level, will be used for $\delta_{SOH\ Water}$.

Figure 62 shows four plots of $\delta_{Pd\ Shifted\ Water}$ as a function of hydration, one for each permutation of the maximum and minimum value being used for the two approximated variables: Pd surface fraction, f, and number of water molecules shifted by the Pd, n_W. It shows that the chemical shift of the Pd shifted water has to increase with increasing hydration in order to reproduce the chemical shift of Pd Water Group 1, in some cases quite significantly.

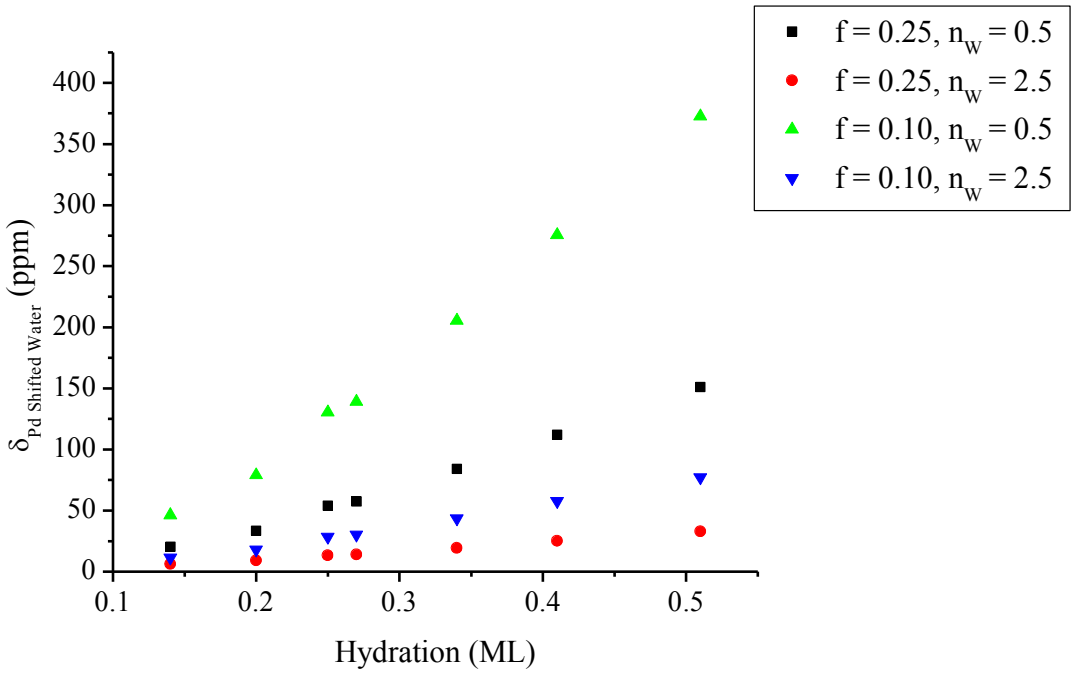

Figure 62: Calculated chemical shift of the Pd shifted water group required to cause the shift of Pd Water Group 1, as a function of hydration. Each data set is distinguished by the fraction of Pd atoms at the surface of clusters (f) and the number of water molecules being shifted by each of these surface Pd (n_W).

The first issue with these results is that the chemical shift of the Pd shifted water has no reason to change with hydration. It is the first water site to be hydrated, since it has the highest adsorption energy, so its population reaches its maximum before the first hydration level measured. While there may be chemical or physical exchange occurring with this site, this will not affect what the chemical

shift is for the water molecules that occupy the site. Secondly, some of the chemical shifts that this model requires in order to reproduce the shift of Pd Water Group 2, as high as 370 ppm, are well outside anything reported for a ^{1}H NMR chemical shift. Finally, phenomenal exchange rates would be required to coalescence two peaks separated by 13 – 370 ppm, which translates to 6.5 – 185 kHz in a 500 MHz ^{1}H NMR experiment; at least $3 \times 10^{4} - 9 \times 10^{5}$ s^{-1}. Again, these are well outside any reported exchange rates found in the literature for similar systems.

Based on the discussion in this section, a model relying on a water group that has been shifted far downfield by the Pd metal clusters cannot explain the characteristics of Pd Water Group 1 and 2. While the model presented in the previous section, Model A, cannot be conclusively labeled as the complete description of the behavior of water in Pd-MCM-41, the failure of the model just discussed does bolster its claim.

8. Conclusions and Recommendations for Future Work

The physical structure of pristine and Pd loaded MCM-41, as well as the behavior of water adsorbed on their pore surfaces, have been investigated. The structure of the pristine sample was determined to be in keeping with well formed MCM-41. Both the XRD and N_2 adsorption results suggest that the Pd-MCM-41 material has been degraded somewhat in the synthesis process, though it still maintains a high specific surface area and enough long range order in its pore structure to cause multiple x-ray reflections. A reduction treatment in H_2 gas did not seem to affect the structure of Pd-MCM-41.

^{1}H MAS NMR spectra of water on pristine MCM-41 were successfully fit using the existing Walia model. It was shown that this model, though initially developed for commercially synthesized MCM-41 at hydration levels up to 0.2 ML, can be applied to samples synthesized in the laboratory and hydrated up to 0.51 ML, so long as appropriate considerations were made. The first of these was the appearance of an additional peak at around 0.5 ML, which was attributed to pore-filling water that has condensed in the pores of the material, similar to that described by Grunberg [30]. The second is the introduction of water-water interactions, once the hydration level had exceeded ~ 0.2 ML. With these considerations, and after reconciling a few discrepancies, the current results for pristine MCM-41 were determined to match those of Walia. Therefore, the current fittings of the pristine MCM-41 ^{1}H MAS NMR spectra were used to aid and assess the fitting of the NMR spectra for the Pd loaded samples.

Fitting of the spectra for the Pd-MCM-41 and reduced Pd-MCM-41 samples required the addition of two peaks to the Walia model to account for the differences between their spectra and those of the pristine sample. These two peaks were labeled Pd Water Group 1 and Pd Water Group 2, since they were clearly caused by the Pd clusters; specifically, the oxide layer that coats them. With these peaks added, the spectra could be fit successfully. This was determined by observing that the chemical

shifts, as well as many of the trends in area and peak width, that were found in the palladized samples were identical or similar to those in the pristine sample.

Besides the presence of Pd Water Group 1 and 2, the other peaks also showed that they were affected by the presence of the Pd clusters. The differences between the Pd loaded and pristine samples formed the basis for the models presented as explanations of the behavior of water on Pd-MCM-41.

Two models were proposed, designated Model A and Model B, to explain these observations. Model A involves water first dissociatively and preferentially adsorbing onto the Pd clusters. This leads to water condensing around the clusters in a manner similar to the pore-filling water of pristine MCM-41 above 0.5 ML. This multilayer water group that is associated with the Pd clusters is undergoing fast exchange with the SOH water nearby. Pd Water Group 1 is the result of this exchange and Pd Water Group 2 is the first few layers of water that are strongly associated with the Pd clusters.

Model B requires the Pd clusters to cause the water nearest to it to have a very large, downfield chemical shift. This water group (Pd shifted water) is then in fast exchange with SOH water and HBOH water, leading to the Pd Water Group 1 and Pd Water Group 2 peaks, respectively.

Both of these models are evaluated by trying to reproduce the chemical shift of Pd Water Group 1. Model A does so reasonably well; the simulated shift becomes closer to the measured value with increasing hydration level. For Model B to accomplish the same result, the chemical shift of the Pd shifted water would have to increase as a function of hydration, which is not possible given the details of the model. In some cases, depending on the parameters of the model, the shift would have to be outside of what is justifiable for the system. The other consequence of these enormous shifts is that it puts an equally large, and equally unrealistic, demand on the exchange rates required for the two peaks to coalesce into one. All of these points conspire against such a model, so Model B is ruled out as a

possibility, and the influence of the Pd metal on the shift of the adsorbed water is determined to be negligible. Therefore, based on the results presented here and the interpretation thereof, Model A seems to be the most likely explanation of the observations, and is deemed to be the best description for the behavior of water on Pd-MCM-41.

In order to improve the credibility of Model A, there are several experiments that could be performed in the future. First, more detailed information on the Pd clusters in the sample should be obtained. This would be best achieved with SEM and TEM measurements of a higher resolution than those presented here. These experiments would be able to show if the metal has made it into the pores and what the size of these particles are, allowing a conclusive estimate of the number of Pd atoms at the surface of the clusters available for interactions with water.

An NMR exchange study would provide the most useful information in vetting the proposed model of water in Pd-MCM-41. Both Model A and Model B require some form of exchange between various groups. Determining what groups in the ^{1}H MAS NMR spectrum of hydrated Pd-MCM-41 are products of exchange, what the constituent groups are and what exchange rates are involved, would substantially support or disprove either model. Another experiment that would be useful is a measurement of the chemical shift of water on oxidized Pd particles, since this is another key feature to both models. The results of these experiments would go a long way in refining the understanding of water on Pd-MCM-41.

Once enough confidence exists in a model for the behavior of water in Pd-MCM-41, investigation of spillover in this system can begin. The main experiment would be recreating spillover conditions in the Pd-MCM-41 system, through a high temperature H_2 exposure, and measuring the resulting sample with ^{1}H MAS NMR. A thorough analysis of the results of this experiment would be a considerable contribution to the literature on spillover. Extending this idea, the same measurement on

a carbonaceous system, such as Pd loaded, activated charcoal, would be even more substantial, as no ^{1}H MAS NMR results exist for such a sample.

References

[1] Khoobiar S. Particle to particle migration of hydrogen atoms on platinum-alumina catalysts from particle to neighboring particles. *J. Phys. Chem.*, 1964; **68**: 411-412

[2] Boudart M, Vannice MA, Benson JE. Adlineation, portholes and spillover. *Z. Phys. Chem.*, 1969; **64**: 171-177

[3] Sermon PA, Bond GC. Hydrogen Spillover. *Catal. Rev.: Sci. Eng.*, 1974; **8**: 211-239

[4] Conner WC, Falconer JL. Spillover in Heterogeneous Catalysis. *Chem. Rev.*, 1995; **95**: 759-788

[5] Rozanov VV, Krylov OV. Hydrogen Spillover in Heterogeneous Catalysis. *Russ. Chem. Rev.*, 1997; **66**: 107-119

[6] Prins R. Hydrogen Spillover - Facts and Fiction. *Chem. Rev.*, 2012; **112**: 2714-2738

[7] Tsao C, Liu Y, Chuang H, Tseng H, Chen T, Chen C, Yu M, Li Q, Lueking A, Chen S. Hydrogen Spillover Effect of Pt-Doped Activated Carbon Studied by Inelastic Neutron Scattering. *J. Phys. Chem. Lett.*, 2011; **2**: 2322-2325

[8] Psofogiannakis GM, Froudakis GE. Fundamental studies and perceptions on the spillover mechanism for hydrogen storage. *Chem. Comm.*, 2011; **47**: 7933-7943

[9] Root TW, Duncan TM. Characterization of hydrogen on silica-supported rhodium with 1H NMR spectroscopy. *Chem. Phys. Lett.*, 1987; **137**: 57-62

[10] Wu X, Gerstein BC, King TS. Characterization of silica-supported ruthenium catalysts by hydrogen chemisorption and nuclear magnetic resonance of adsorbed hydrogen. *J. Catal.*, 1989; **118**: 238-254

[11] Gajardo P, Apple TM, Dybowski C. Observation of surface states of hydrogen on a Rh/TiO2

catalyst by NMR spectroscopy. *Chem. Phys. Lett.*, 1980; **74**: 306-308

[12] Apple TM, Gajardo P, Dybowski C. NMR, ESR, and TPD Study of H2 Adsorption on Rh/TiO2 Catalyst. *J. Catal.*, 1981; **68**: 103-108

[13] Bhatia S, Engelke F, Pruski M, Gerstein BC, King TS. Interaction of Hydrogen with Supported Ru Catalysts: High Pressure in Situ NMR Studies. *J. Catal.*, 1994; **147**: 455-464

[14] Sheng T, Gay ID. Proton magnetic resonance of hydrogen adsorbed on supported platinum catalysts. *J. Catal.*, 1981; **71**: 119-126

[15] Van Meerbeek A, Jelli A, Fripiat JJ. Reduction of the Surface of Silica Gel by Hydrogen Spillover. *J. Catal.*, 1977; **46**: 320-325

[16] Lenz DH, Conner WC. Hydrogen Spillover on Silica. *J. Catal.*, 1988; **112**: 116-125

[17] Chao Z, Wu T, Ye J, Chen G, Wan H. 1H MAS NMR Characterization of Hydrogen Over Silica-Supported Rhodium Catalyst. *Sci. Chi.*, 2001; **44**: 103-112

[18] Wang L, Yang RT. New sorbents for hydrogen storage by hydrogen spillover – a review. *Ener. Env. Sci.*, 2008; **1**: 268-279

[19] Beck JS, Vartuli JC, Roth WJ, Leonowicz ME, Kresge CT, Schmitt KD, Chu CTW, Olson DH, Sheppard EW, McCullen SB, Higgins JB, Schlenker JL. A New Family of Mesoporous Molecular Sieves Prepared with Liquid Crystal Templates. *J. Am. Chem. Soc.*, 1992; **114**: 10834-10843

[20] Kresge CT, Leonowicz ME, Roth WJ, Vartuli JC, Beck JS. Ordered mesoporous molecular sieves synthesized by a liquid-crystal template mechanism. *Nature*, 1992; **359**: 710-712

[21] Walia J, Crone J, Liang J, Niknam M, Lemaire C, Thompson RT, Peemoeller H. Temperature and hydration dependence of proton MAS NMR spectra in MCM-41: Model based on motion induced chemical shift averaging. *SSNMR*, 2013; **49-50**: 26-32

[22] Marin-Astorga N, Pecchi G, Fierro JLG, Reyes P. Alkynes hydrogenation over Pd-supported catalysts. *Catal. Lett.*, 2003; **91**: 115-121

[23] Li H, Chen J, Wan Y, Chai W, Zhang F, Lu Y. Aqueous medium Ullmann reaction over a novel Pd/Ph–Al-MCM-41 as a new route of clean organic synthesis. *Green Chem.*, 2007; **9**: 273-280

[24] Gannouni A, Albela B, Said Zina M, Bonneviot L. Metal dispersion, accessibility and catalytic activity in methane oxidation of mesoporous templated aluminosilica supported palladium. *Appl. Catal. A: Gen.*, 2013; **464-465**: 116-127

[25] Kanda Y, Seino A, Kobayashi T, Uemichi Y, Sugioka M. Catalytic Performance of Noble Metals Supported on Mesoporous Silica MCM-41 for Catalytic Performance of Noble Metals Supported on Mesoporous Silica MCM-41 for Hydrodesulfurization of Benzothiophene. *J. Jap. Petr. Inst.*, 2009; **52**: 42-50

[26] Mastalir A, Rac B, Kiraly Z, Molnar A. In situ generation of Pd nanoparticles in MCM-41 and catalytic applications in liquid-phase alkyne hydrogenations. *J. Mol. Catal. A: Chem.*, 2007; **264**: 170-178

[27] Niknam M, Liang J, Walia J, Peemoeller H. Chemical exchange and spectral coalescence in low-hydration MCM-41 studied by proton NMR. *Mic. Meso. Mat.*, 2012; **162**: 136-142

[28] Hassan H, Reardon E, Peemoeller H. Correlation between deuterium NMR spectral components and MCM-41 pore surface hydration sites. *Mic. Meso. Mat.*, 2009; **122**: 121-127

[29] Trebosc J, Wiench JW, Huh S, Lin VSY, Pruski M. Solid-State NMR Study of MCM-41-type Mesoporous Silica Nanoparticles. *J. Am. Chem. Soc.*, 2005; **127**: 3057-3068

[30] Grunberg B, Emmler T, Gedat E, Shenderovich I, Findenegg GH, Limbach H, Buntkowsky G. Hydrogen Bonding of Water Confined in Mesoporous Silica MCM-41 and SBA-15 Studied by 1H

Solid-State NMR. *Chem. Eur. J.*, 2004; **10**: 5689-5696

[31] Vyalikh A, Emmler T, Grunberg B, Xu Y, Shenderovich I, Findenegg GH, Limbach H, Buntkowsky G. Hydrogen Bonding of Water Confined in Controlled-Pore Glass 10-75 Studied by 1H-Solid State NMR. *Z. Phys. Chem.*, 2007; **221**: 155-168

[32] Stapf S, Kimmich R, Seitter RO. Proton and Deuteron Field-Cycling NMR Relaxometry of Liquids in Porous Glasses: Evidence for Levy-Walk Statistics. *Phys. Rev. Lett.*, 1995; **75**: 2855-2858

[33] Korb JP, Malier L, Cros F, Xu S, Jonas J. Surface dynamics of liquids in nanopores. *Phys. Rev. Lett.*, 1996; **77**: 2312-2315

[34] D'Orazio F, Bhattacharja S, Halperin WP, Eguchi K. Molecular diffusion and nuclear-magnetic-resonance relaxation of water in unsaturated porous silica glass. *Phys. Rev. B*, 1990; **42**: 9810-9818

[35] Holly R, Peemoeller H, Choi C, Pintar MM. Proton rotating frame spin-lattice relaxation study of slow motion of pore water. *J. Chem. Phys.*, 1998; **108**: 4183-4188

[36] Schreiber A, Ketelsen I, Findenegg GH. Melting and freezing of water in ordered mesoporous silica materials. *Phys. Chem. Chem. Phys.*, 2001; **3**: 1185-1195

[37] Vallet-Regi M, Ramila A, del Real RP, Perez-Pariente J. A New Property of MCM-41: Drug Delivery System. *Chem. Mater.*, 2001; **13**: 308-311

[38] Khodakov AY, Zholobenko VL, Bechara R, Durand D. Impact of aqueous impregnation on the long-range ordering and mesoporous structure of cobalt containing MCM-41 and SBA-15 materials. *Mic. Meso. Mat.*, 2005; **79**: 29-39

[39] Mokhonoana MP, Coville NJ. Highly loaded Fe-MCM-41 materials: Synthesis and reducibility studies. *Materials*, 2009; **2**: 2337-2359

[40] Prasanth KP, Raj MC, Bajaj HC, Kim TH, Jasra RV. Hydrogen sorption in transition metal

modified mesoporous materials. *Int. J. Hyd. Ener.*, 2010; **35**: 2351-2360

[41] Junges U, Disser S, Schmid G, Schuth F. Ordered mesoporous materials as catalyst supports. *Meso. Mol. Siev.*, 1998; **117**: 391-398

[42] Benito P, Gregori M, Andreoli S, Fornasari, Millefanti S, Ospitali F, Albonetti. Role of the preparation method on properties of Pd/Cu-MCM-41 hydrodechlorinating catalysts. *Catal. Today*, 2014; **235**: 134-143

[43] Koh, C.A., R. Nooney and S. Tahir. Characterization and catalytic properties of MCM41 and Pd/MCM-41 materials. *Catal. Lett.*, 1997; **47**: 199-203

[44] Demel J, Cejka J, Stepnicka P. The use of palladium nanoparticles supported on MCM-41 mesoporous molecular sieves in Heck reaction: A comparison of basic and neutral supports. *J. Mol. Catal. A: Chem.*, 2007; **274**: 127-132

[45] Slichter CP. Principles of Magnetic Resonance, 3rd ed., Springer-Verlag. 1989

[46] Abragam A. The Principles of Nuclear Magnetism, 1st ed., Oxford Unversity Press. 1961

[47] Lamb WE. Internal Diamagnetic Fields. *Phys. Rev.*, 1941; **60**: 817-819

[48] Ramsey NF. Chemical shift in nuclear magnetic resonance and in diamagnetic susceptibility. *Phys. Rev.*, 1952; **86**: 243-246

[49] Ramsey NF. Magnetic shielding of nuclei in molecules. *Phys. Rev.*, 1950; **78**: 699-703

[50] Casabianca LB, de Dios AC. Ab initio calculations of NMR chemical shifts. *J. Chem. Phys.*, 2008; **128**: 052201(1-10)

[51] Markley JL, Bax A, Arata Y, Hilbers CW, Kaptein R, Sykes BD, Wright PE, Wuthrich K. Recommendations for the presentation of NMR structures of proteins and nucleic acids. *J. Mol. Bio.*,

1998; **280**: 933-952

[52] Fukushima E, Roeder SBW. Experimental Pulse NMR: A Nuts and Bolts Approach, 1st ed., Addison Wesley Publishing. 1981

[53] Bloembergen N, Purcell EM, and Pound R. Relaxation effects in nuclear magnetic resonance absorption. *Phys. Rev.*, 1948; **73**: 679-712

[54] Ernst RR, Bodenhausen G, Wokaun A. Principles of Nuclear Magneric Resonance in One and Two Dimensions, 1st ed., Clarendon Press. 1987

[55] Benson JE, Kohn HW, Boudart M. On the reduction of tungsten trioxide accelerated by platinum and water. *J. Catal.*, 1966; **5**: 307-313

[56] Dalla Betta RA, Boudart M. Hydroxyl exchange on H–CaY and Pt/H–CaY zeolites with deuterium. *J. Chem. Soc. Fara. Trans. 1*, 1976; **72**: 1723-1732

[57] Carley AF, Edwards HA, Mile B, Roberts MW, Rowlands CC, Jackson SD, Hancock FE. An EPR study of a palladium catalyst using a PBN (N-benzylidene-tert-butylamine N-oxide) spin trap: direct demonstration of hydrogen spillover. *J. Chem. Soc. Chem. Comm.*, 1994; : 1407-1408

[58] Levy RB, Boudart M. The kinetics and mechanism of spillover. *J. Catal.*, 1974; **32**: 304-314

[59] Boudart M. On the nature of spilt-over hydrogen. *J. Mol. Catal. A: Chem.*, 1999; **138**: 319-321

[60] Young GJ. Interaction of Water Vapor with Silica Surfaces. *J. Coll. Sci.*, 1958; **13**: 67-85

[61] Lange KR. The Characterization of Molecular Water on Silica Surfaces. *J. Coll. Sci.*, 1965; **20**: 231-240

[62] Shen JL, Lee YC, Lui YL, Cheng PW, Cheng CF. Blue–green photoluminescence in MCM-41 mesoporous nanotubes. *J. Phys. Cond. Matt.*, 2003; **15**: L297-L304

[63] Bronnimann CE, Zeigler RC, Maciel GE. Proton NMR Study of Dehydration of the Silica Gel Surface. *J. Am. Chem. Soc.*, 1988; **110**: 2023-2026

[64] Payne CC. Applications of colloidal silica: past, present and future, Chapter 54 in Colloidal Silica: Fundamentals and Applications. Edited by Bergna HE, Roberts WO. 2006

[65] Zimmerman JR, Brittin WE. Nuclear Magnetic Resonance Studies in Multiple Phase Systems: Lifetime of a Water Molecule in an Adsorbing Phase on Silica Gel. *J. Phys. Chem.*, 1957; **61**: 1328-1333

[66] Rouquerol J, Avnir D, Fairbridge CW, Everett DH, Haynes JH, Pernicone N, Ramsay JDF, Sing KSW, Unger KK. Recommendations for the Characterization of Porous Solids. *Pure & Appl. Chem.*, 1994; **66**: 1739-1758

[67] Zhao XS, Lu GQ, Whittaker AK, Millar GJ, Zhu HY. Comprehensive study of surface chemistry of MCM-41 using 29Si CP MAS NMR, FTIR, pyridine-TPD, and TGA. *J. Phys. Chem. B*, 1997; **101**: 6525-6531

[68] Glinka CJ, Nicol JM, Stucky GD, Ramli E, Margolese D, Huo Q, Higgins JB, Leonowicz ME. Small angle neutron scattering study of the structure and formation of MCM-41 mesoporous molecular sieves. *J. Por. Mat.*, 1996; **3**: 93-98

[69] Chen C, Burkett SL, Li H, Davis ME. Studies on mesoporous materials II. Synthesis mechanism of MCM-41. *Mic. Mat.*, 1993; **2**: 27-34

[70] Chen C, Li H, Davis ME. Studies on mesoporous materials: I. Synthesis and characterization of MCM-41. *Mic. Mat.*, 19933; **2**: 17-26

[71] Marler B, Oberhagemann U, Vortmann S, Gies H. Influence of the sorbate type on the XRD peak intensities of loaded MCM-41. *Mic. Mat.*, 1996; **6**: 375-383

[72] Klug HP, Alexander LE. X-ray Diffraction Procedures for Polycrystalline and Amorphous Materials, 2nd ed., John Wiley and Sons. 1974

[73] Mansour F, Dimeo RM, Peemoeller H. High-resolution inelastic neutron scattering from water in mesoporous silica. *Phys. Rev. E*, 2002; **66**: 041307(1-7)

[74] Kruk M, Jaroniec M, Sayari A. A unified interpretation of high-temperature pore size expansion processes in MCM-41 mesoporous silicas. *J. Phys. Chem. B*, 1999; **103**: 4590-4598

[75] Gregg SJ, Sing KSW. Adsorption, Surface Area and Porosity, 2 ed., Academic Press. 1982

[76] Kenny MB, Sing KSW. Adsorptive properties of porous silicas, Chapter 44 in Colloidal Silica: Fundamentals and Applications. Edited by Bergna HE, Roberts WO. 2006

[77] Brunauer S, Emmett PH, Teller E. Adsorption of gases in multimolecular layers. *J. Am. Chem. Soc.*, 1938; **60**: 309-319

[78] Bergna HE. Colloid chemistry of silica: An overview, Chapter 3 in Colloidal Silica: Fundamentals and Applications. Edited by Bergna HE, Roberts WO. 2006

[79] Chuang I, Maciel GE. A detailed model of local structure and silanol hydrogen bonding on silica gel surfaces. *J. Phys. Chem. B*, 1997; **101**: 3052-3064

[80] Park S, Lee S. A study on hydrogen-storage behaviors of nickel-loaded mesoporous MCM-41. *J. Coll. Int. Sci.*, 2010; **346**: 194-198

[81] Wojcieszak J, Monteverdi S, Mercy M, Nowak I, Ziolek M, Bettahar MM. Nickel containing MCM-41 and AlMCM-41 mesoporous molecular sieves: Characteristics and activity in the hydrogenation of benzene. *Appl. Catal. A: Gen.*, 2004; **268**: 241-253

[82] Wise EM. Palladium: Recovery, Properties, and Uses, 1st ed., Academic Press. 1968

[83] Chang W, Chae G, Jang SR, Shin J, BJ Ahn. An efficient microwave-assisted Suzuki reaction using Pd/MCM-41 and Pd/SBA-15 as catalysts in solvent-free condition. *J. Ind. Eng. Chem.*, 2012; **18**: 581-585

[84] Petersson LG, Dannetun HM, Lundstrom I. Water production on palladium in hydrogen-oxygen atmospheres. *Surf. Sci.*, 1985; **163**: 273-284

[85] Johansson M, Ekedahl LG. The water formation rate on platinum and palladium as a function of the surface hydrogen pressure from three-dimensional hydrogen pressure distributions. *Appl. Surf. Sci.*, 2001; **180**: 27-35

[86] Johansson M, Ekedahl LG. Hydrogen adsorbed on palladium during water formation studied with palladium membranes. *Appl. Surf. Sci.*, 2001; **173**: 122-133

[87] Guthrie, C. Behaviour of Mesoporous Silica MCM-41 Supported Catalysts in Degradation Reactions. PhD Thesis, University of Waterloo. 2012

[88] Cheng CF, Park DH, Klinowski J. Optimal parameters for the synthesis of the mesoporous molecular sieve [Si]-MCM-41. *J. Chem. Soc. F. Trans.*, 1997; **93**: 193-197

[89] Liang, J. Proton NMR Study of Water Molecule Dynamics in MCM-41. MSc Thesis, Univeristy of Waterloo. 2006

[90] Hassan, J. NMR Study of Exchange and Hydration Site Identification in MCM-41. PhD Thesis, University of Waterloo. 2006

[91] Kruk M, Jaroniec M, Sayari A. Adsorption study of surface and structural properties of MCM-41 materials of different pore sizes. *J. Phys. Chem. B*, 1997; **101**: 583-589

[92] Panpranot J, Pattamakomsan K, Goodwin JG, Praserthdam P. A comparative study of Pd/SiO2 and Pd/MCM-41 catalysts in liquid-phase hydrogenation. *Catal. Comm.*, 2004; **5**: 583-590

[93] Pasqua L, Testa F, Aiello R, Di Renzo F, Fajula F. Influence of pH and nature of the anion on the synthesis of pure and iron-containing mesoporous silica. *Mic. Meso. Mat.*, 2001; **44-45**: 111-117

[94] Kloetstra KR, van Laren M, van Bekkum H. Binary caesium-lanthanum oxide supported on MCM-41: A new stable heterogenous basic catalyst. *J. Chem. Soc. Fara. Trans*, 1997; **93**: 1211-1220

[95] Batsanov, SS. Van der Waals Radii of Elements. *Inorg. Mat.*, 2001; **37**: 871-885

[96] Franks F. Water: A Matrix of Life, 2nd ed., The Royal Society of Chemistry. 2000

[97] Tan ML, Fischer JT, Chandra A, Brooks BR, Ichiye T. A temperature of maximum density in soft sticky dipole water. *Chem. Phys. Lett.*, 2003; **376**: 646-652

[98] Wang LP, Head-Gordon T, Ponder JW, Ren P, Chodera JD, Eastman PK, Martinez TJ, Pande VS. Systematic Improvement of a Classical Molecular Model of Water. *J. Phys. Chem. B*, 2013; **117**: 9956-9972

[99] Email correspondence with Dr. Colin Guthrie. March 31, 2013

[100] Zhao XS, Audley F, Lu GQ. Irreversible Change of Pore Structure of MCM-41 upon Hydration at Room Temperature. *J. Phys. Chem. B*, 1998; **102**: 4143-4146

[101] Ribeiro Carrott MML, Estevao Candeias AJ, Carrott PJM, Unger KK. Evaluation of the stability of pure silica MCM-41 toward water vapor. *Langmuir*, 1999; **15**: 8895-8901

[102] Guthrie CP, Reardon EJ. Metastability of MCM-41 and Al-MCM-41. *J. Phys. Chem. A*, 2008; **112**: 3386-3390

[103] Landau MV, Varkey SP, Herskowitz M, Regev O, Pevzner S, Sen T, Luz Z. Wetting stability of Si-MCM-41 mesoporous material in neutral, acidic and basic aqueous solutions. *Mic. Meso. Mat.*, 1999; **33**: 149-163

[104] Chantler T. Theoretical Form Factor, Attenuation and Scattering Tabulation for Z=1-92 from E=1-10 eV to E=0.4-1.0 MeV. *J. Phys. Chem. Ref. Data*, 1995; **24**: 71-643

[105] Jacobs WPJH, de Haan JW, van de Ven JM, van Santen RA. Interaction of ammonia with Broensted acid sites in different cages of zeolite Y as studied by 1H MAS NMR. *J. Phys. Chem.*, 1993; **97**: 10394-10402

[106] Hunger M. Multinuclear solid-state NMR studies of acidic and non-acidic hydroxyl protons in zeolites. *SSNMR*, 1996; **6**: 1-29

[107] Hunger M, Schenk U, Breuninger M, Glaser R, Weitkamp J. Characterization of the acid sites in MCM-41-type materials by spectroscopic and catalytic techniques. *Mic. Meso. Mat.*, 1999; **27**: 261-271

[108] Kan HH, Colmyer RJ, Asthagiri A, Weaver JF. Adsorption of Water on a PdO(101) Thin Film: Evidence of an Adsorbed HO-H2O Complex. *J. Phys. Chem. C*, 2009; **113**: 1495-1506

[109] Lundgren E, Gustafson J, Mikkelsen A, Andersen JN. Kinetic Hindrance During the Initial Oxidation of Pd(100) at Ambient Pressures. *Phys. Rev. Lett.*, 2004; **72**: 1-4

[110] Kostelnik P, Seriani N, Kresse G, Mikkelsen A, Lundgren E, Blum V, Sikola T, Varga P, Schmid M. The Pd(100)-(√5 x √5)R27°-O Surface Oxide: A LEED, DFT and STM Study. *Surf. Sci.*, 2007; **601**: 1574-1581

[111] Todorova M, Lundgren E, Blum V, Mikkelsen A, Gray S, Gustafson J, Borg M, Rogal J, Reuter K, Andersen JN, Scheffler M. The Pd(100)-(√5 x √5)R27°-O Surface Oxide Revisited. *Surf. Sci.*, 2003; **541**: 101-112

[112] Yang J, Meng S, Xu L, Wang EG. Water adsorption on hydroxylated silica surfaces studied using the density functional theory. *Phys. Rev. B*, 2005; **71**: 03541(1-12)

[113] Shi Z, Ford JV, Wei S, Castleman AW. Water clusters: Contributions of binding energy and entropy to stability. *J. Chem. Phys.*, 1993; **99**: 8009-8015

[114] del Bene J, Pople JA. Intermolecular energies of small water polymers. *Chem. Phys. Lett.*, 1969; **4**: 426-428

[115] del Bene J, Pople JA. Theory of Molecular Interactions. I. Molecular Orbital Studies of Water Polymers Using a Minimal Slater-Type Basis. *J. Chem. Phys.*, 1970; **52**: 4858-4866

[116] Magnera TF, David DE, Michl J. The first twenty-eight gas-phase proton hydration energies. *Chem. Phys. Lett.*, 1991; **182**: 363-370

[117] Karlberg GS. Adsorption trends for water, hydroxyl, oxygen, and hydrogen on transition-metal and platinum-skin surfaces. *Phys. Rev. B*, 2006; **74**: 153414(1-4)

[118] Cogley DR, Falk M, Butler JN, Grunwald E. Solvation and self-association of water in propylene carbonate. *J. Phys. Chem.*, 1972; **76**: 855-864

[119] Shanan-Atidi H, Bar-Eli KH. A convenient method for obtaining free energies of activation by the coalescence temperature of an unequal doublet. *J. Phys. Chem.*, 1970; **74**: 961-963

[120] Kurland RJ and McGarvey BR. Isotropic NMR Shifts in Transition Metal Complexes: The Calculation of the Fermi Contact and Pseudocontact Terms. *J. Mag. Res.*, 1970; **2**: 286-301

[121] Slichter CP. Probing Phenomena at Metal Surfaces by NMR. *Ann. Rev. Phys. Chem.*, 1986; **37**: 25-51

[122] Levitt MH. Spin Dynamics: Basics of Nuclear Magnetic Resonance, 2nd ed., John Wiley and Sons. 2008

[123] Li J, Pilla KB, Li Q, Zhang Z, Su X, Huber T, and Yang J. Magic Angle Spinning NMR Structure Determination of Proteins from Pseudocontact Shifts. *J. Am. Chem. Soc.*, 2013; **135**: 8294-8303

[124] Zhang Y, Sun H, and Oldfield E. Solid-State NMR Fermi Contact and Dipolar Shifts in Organometallic Complexes and Metalloporphyrins. *J. Am. Chem. Soc.*, 2005; **127**: 3652-3653

[125] Rades T, Polisset-Thfoin M, Fraissard J. Study of supported Pt-Pd catalysts by hydrogen chemisorption and proton NMR of sorbed species. Evidence for an alloying effect. *Top. Catal.*, 2000; **11/12**: 283-287

[126] Bonardet JL, Fraissard J, de Menorval LC. Palladium and proton knight shift in palladium hydride. *Proc. 6th Int. Conf. Catal.*. 1977

[127] Brill P, Voitlander J. Palladium and proton knight shift in palladium hydride. *Ber. Buns. Phys. Chem.*, 1973; **77**: 1097-1103

[128] Kohlmann O, Steinmetz WE, Mao X, Wuelfing WP, Templeton AC, Murray RW, Johnson CS. NMR Diffusion, Relaxation, and Spectroscopic Studies of Water Soluble, Monolayer-Protected Gold Nanoclusters. *J. Phys. Chem. B*, 2001; **105**: 8801-8809

[129] Damyanova S, Pawelec B, Arishtirova K, Fierro JLG, Sener C, Dogu T. MCM-41 supported PdNi catalysts for dry reforming of methane. *Appl. Catal. B: Env.*, 2009; **92**: 250-261

[130] Gregori M, Benito P, Fornasari G, Migani M, Millefanti S, Ospitali F, Albonetti S. Preparation of Pd/Cu MCM-41 catalysts for hydrodechlorination: Influence of the synthesis procedure. *Mic. Meso. Mat.*, 2014; **190**: 1-9

Appendix A – Full Set ^{1}H MAS NMR Spectra

This appendix contains the full set of ^{1}H MAS NMR spectra used in this study. Each graph shows the measured spectrum in black and the calculated model in red. The hydration level and sample type is also indicated on each graph. The same vertical and horizontal scale is used in every case for the sake of easy comparison.

Pristine MCM-41
Dry

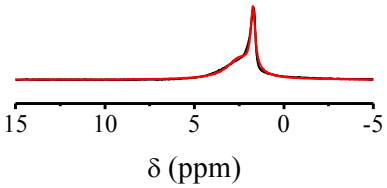

Pristine MCM-41
0.044 ML

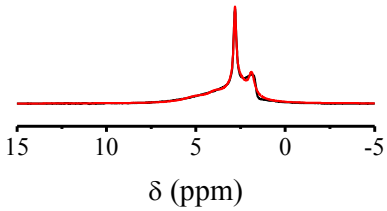

Pristine MCM-41
0.086 ML

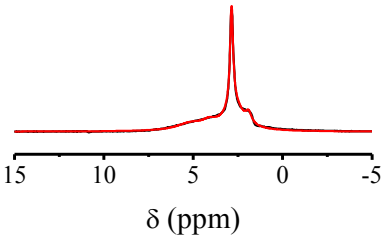

Pristine MCM-41
0.10 ML

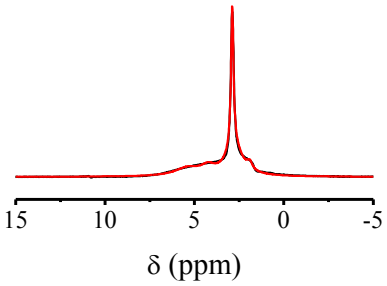

Pristine MCM-41
0.14 ML

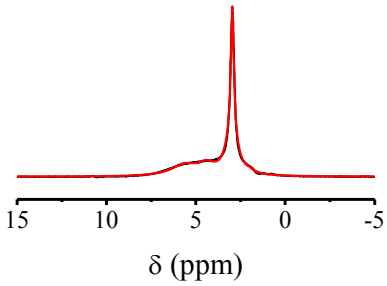

Pristine MCM-41
0.19 ML

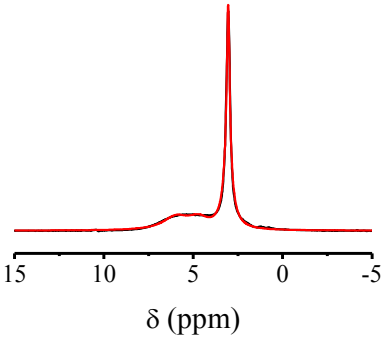

Pristine MCM-41
0.23 ML

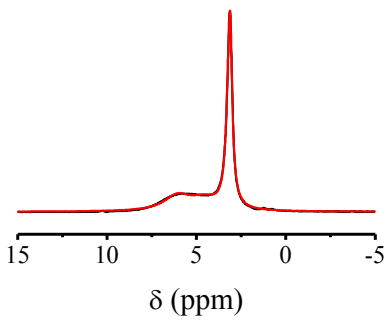

Pristine MCM-41
0.39 ML

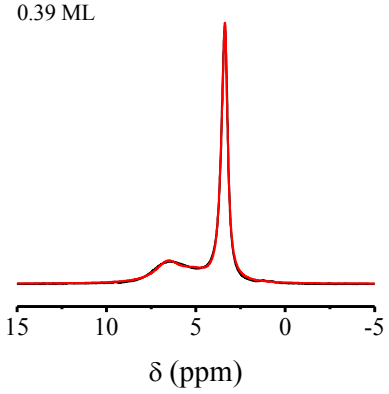

Pristine MCM-41
0.51 ML

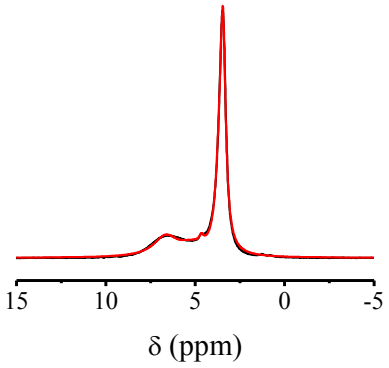

Pd-MCM-41
Dry

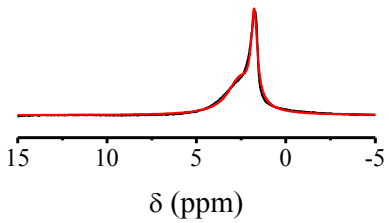

Pd-MCM-41
0.069 ML

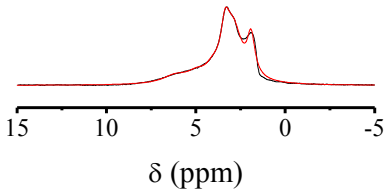

Pd-MCM-41
0.075 ML

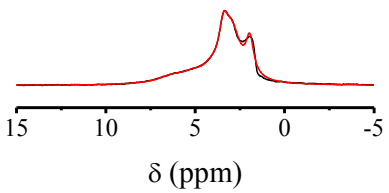

Pd-MCM-41
0.14 ML

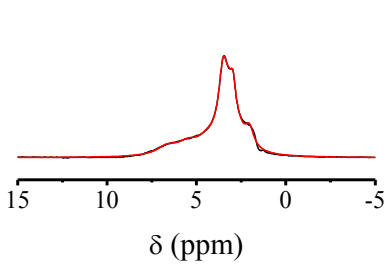

Pd-MCM-41
0.20 ML

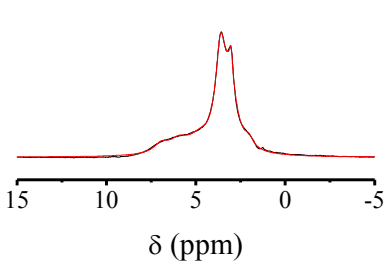

Pd-MCM-41
0.25 ML

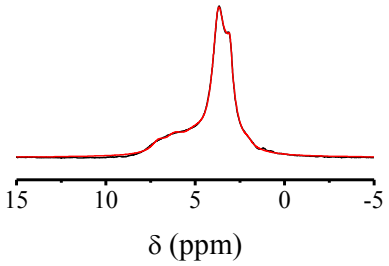

Pd-MCM-41
0.27 ML

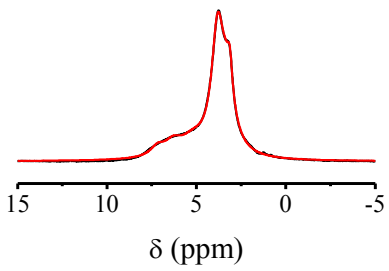

Pd-MCM-41
0.34 ML

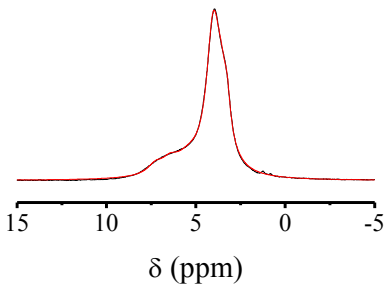

Pd-MCM-41
0.41 ML

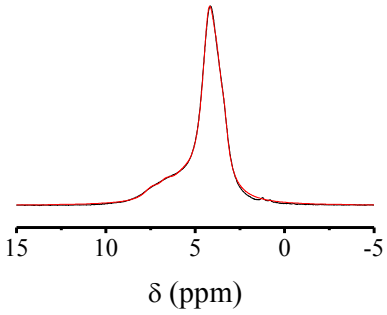

Pd-MCM-41
0.51 ML

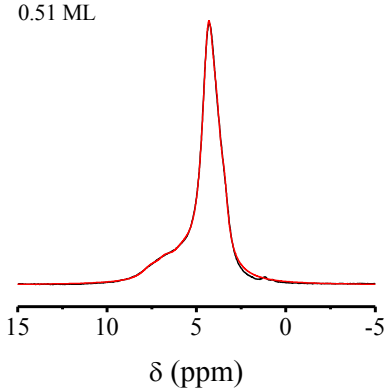

Reduced Pd-MCM-41
Dry

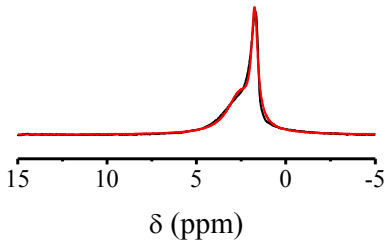

Reduced Pd-MCM-41
0.076 ML

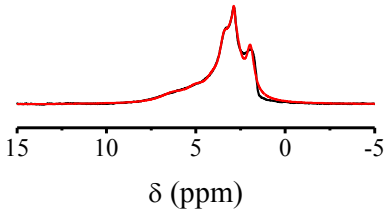

Reduced Pd-MCM-41
0.16 ML

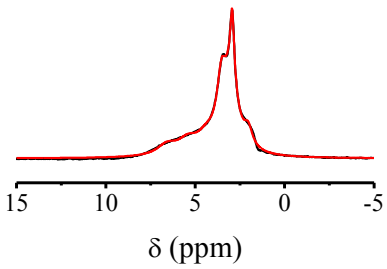

Reduced Pd-MCM-41
0.24 ML

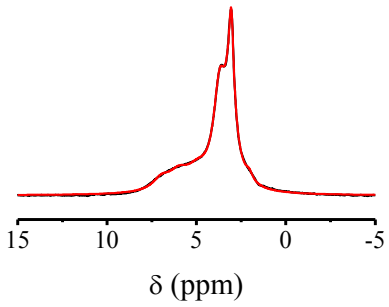

Reduced Pd-MCM-41
0.32 ML

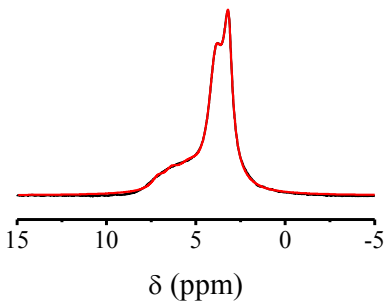

Reduced Pd-MCM-41
0.39 ML

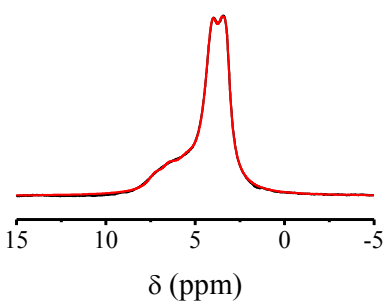

Reduced Pd-MCM-41
0.50 ML

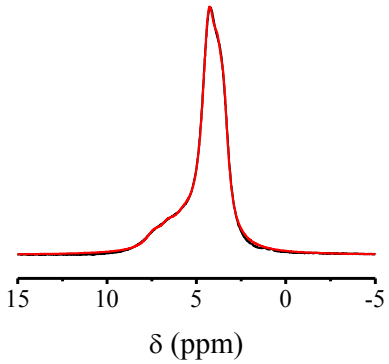

Appendix B – Pd Cluster Size Modeling

The data available on the Pd-MCM-41 material used in the present study is insufficient to conclusively determine the exact distribution of sizes of the Pd clusters the material contains. This information would permit a calculation of the fraction of Pd atoms that are at the surface of these clusters, *f*. These are the Pd atoms in the sample that are capable of interacting with water. This appendix will produce an estimate of *f* by first calculating the number of Pd atoms that are at the surface of a metal cluster based on that cluster's size, and then use this result to determine *f* for a number of cluster size distributions generated from results in existing publications. This results in a range of *f* values that are an approximate representation of *f* in the Pd-MCM-41 sample.

It will be assumed that the Pd clusters are perfect spheres, filled with Pd atoms that are hard spheres. The volumes of both the cluster and a single Pd atom are, respectively,

$$V_{cluster} = \frac{4}{3}\pi r_{cluster}^3 \tag{70a}$$

$$V_{Pd} = \frac{4}{3}\pi r_{Pd}^3 \tag{70b}$$

The unit cell of bulk Pd metal has a face-centred cubic (fcc) crystal packing arrangement [82]. If the clusters are assumed to have the same crystal structure, then the number of Pd atoms in a single Pd cluster is,

$$\begin{aligned} n_{Pd} &= \left(\frac{V_{cluster}}{V_{Pd}}\right) e_{fcc} \\ &= \left(\frac{r_{cluster}}{r_{Pd}}\right)^3 e_{fcc} \end{aligned} \tag{71}$$

where the fcc packing efficiency is, $e_{fcc} = \frac{\pi}{3\sqrt{2}} \approx 0.74$

But only the atoms on the outside of the sphere will interact with water in the pore of Pd-MCM-41.

The number of surface Pd atoms can be approximated in a similar way as the number of atoms in the cluster.

The surface area of a cluster is,

$$S_{cluster} = 4\pi r_{cluster}^2 \tag{72}$$

The number of Pd atoms exposed on the surface of the cluster can be approximated as the surface area of the cluster divided by the cross-sectional area of a single Pd atom, multiplied by a packing efficiency factor,

$$\begin{aligned} n_{Pd}^{surface} &= \left(\frac{S_{cluster}}{A_{Pd}} \right) e_{circle} \\ &= \left(\frac{4\pi r_{cluster}^2}{\pi r_{Pd}^2} \right) e_{circle} \end{aligned} \tag{73}$$

Where the packing efficiency is that of a circle, of radius r, inside of a square, of side length $2r$,

$$\begin{aligned} e_{circle} &= \frac{A_{circle}}{A_{square}} \\ &= \frac{\pi}{4} \end{aligned} \tag{74}$$

So $n_{Pd}^{surface}$ becomes,

$$\begin{aligned} n_{Pd}^{surface} &= \left(\frac{4\pi r_{cluster}^2}{\pi r_{Pd}^2} \right) e_{circle} \\ &= \pi \left(\frac{r_{cluster}}{r_{Pd}} \right)^2 \end{aligned} \tag{75}$$

This approximation is very rough, but improves as ($r_{cluster}$ / r_{Pd}), or equivalently n_{Pd}, increases. With r_{Pd} ≈ 1.4 Å [82], the ratio of the number of Pd atoms on the surface of a cluster to the total number of Pd atoms in a cluster is,

$$\frac{n_{Pd}^{surface}}{n_{Pd}} = \frac{\pi\left(\frac{r_{cluster}}{r_{Pd}}\right)^2}{\left(\frac{r_{cluster}}{r_{Pd}}\right)^3 \frac{\pi}{3\sqrt{2}}} = 3\sqrt{2}\left(\frac{r_{Pd}}{r_{cluster}}\right) = \frac{5.9\,\text{Å}}{r_{cluster}} = \frac{12\,\text{Å}}{d_{cluster}} \tag{76}$$

where $d_{cluster}$ is the diameter of the cluster. In practice, this fraction will have a value of 1 for $d_{cluster}$ less than 12 Å, since there cannot be more surface Pd atoms than there are total Pd atoms. Below this value of $d_{cluster}$, all the Pd atoms are accessible at the surface. Now for a given distribution of cluster sizes, f can be calculated by performing a numerical integration of,

$$f = \int_{x=0.3\,nm} p(x)\frac{n_{Pd}^{surface}}{n_{Pd}}(x)\,dx,\; x \equiv d_{cluster} \tag{77}$$

where $p(d_{cluster})$ is the population of clusters with a particular diameter, given by the cluster size distribution, and the fraction $n_{Pd}^{surface}/n_{Pd}$ is given in equation (76). The integration is started at $d_{cluster}$ = 3 Å, the diameter of a Pd atom, since the cluster cannot be smaller than this.

The cluster size distribution is assumed to have the form of a normal distribution. This is the best choice as a first order approximation, and experimentally determined size distributions for metal particles in MCM-41 that exist in the literature match this approximation well [26, 129, 130]. Five size distributions are generated based on these existing distributions and the available information for the current sample. These simulated distributions are shown in Figure 63.

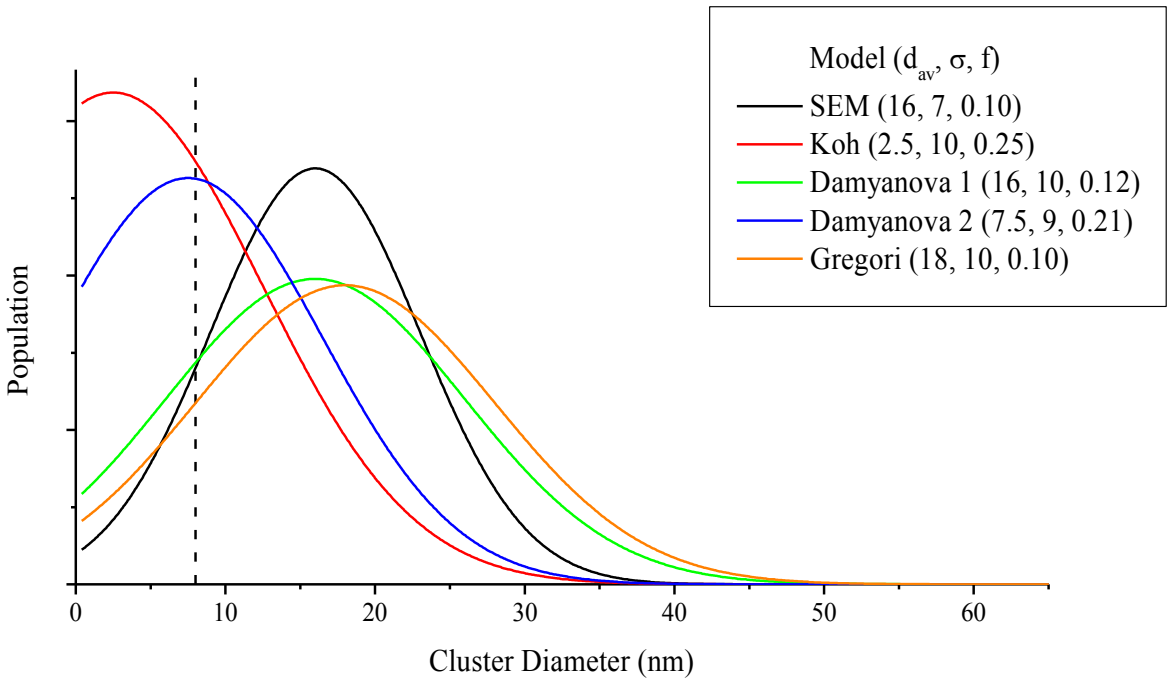

Figure 63: Cluster size distributions for the current observations (SEM) and those in existing publications (Koh, Damyanova and Gregori). The numbers in parentheses are the average particle diameter, d_{av} (in nm), the standard deviation, σ (in nm) and the fraction of the total Pd atoms that are accessible at the surface of the clusters, f, for each distribution. The vertical, dashed line indicates the threshold for what is visible in the SEM image available for the current Pd-MCM-41 sample (8 nm). Any clusters in the distributions that are smaller than this diameter would not be visible in this image (Figure 26).

The two parameters for a normal distribution are the position of its center (which in this case will be the average particle size, d_{av}) and the standard deviation, σ. In generating the distributions shown in Figure 63, these two parameters are chosen to best fit the situation each plot is trying to model. The main requirement set by the SEM results in Figure 26 is that the upper size limit is around 30 nm. For the distribution generated to best match these results (labeled "SEM" in Figure 63), it is also assumed that the majority of the Pd clusters are visible. Therefore, the d_{av} and σ chosen for this case keep most of the particles between 8 and 30 nm in diameter. The remaining size distributions have their d_{av} and σ chosen to best reproduce the results seen in the existing publications by Koh [43],

Damyanova [129] (note that there are two distributions reported in this paper) and Gregori [130]. The values of d_{av}, σ and f are shown in the legend of Figure 63 for each distribution.

The five distributions in Figure 63 are assumed to be a reasonable representation of what might exist in the current system. Therefore, the range of f that will be used in the discussion of the current Pd-MCM-41 sample will be taken to be 0.10 – 0.25 (ie. it is estimated that 10 – 25 % of the Pd atoms present in the sample exist at the surface of Pd clusters).